

AD-769 919

CORRELATION OF PROPERTIES AND MICROSTRUCTURE IN  
WELDED TITANIUM ALLOYS

NORTHROP CORP.

PREPARED FOR  
AIR FORCE MATERIALS LABORATORY

SEPTEMBER 1973

Distributed By:

**NTIS**

National Technical Information Service  
U. S. DEPARTMENT OF COMMERCE

UNCLASSIFIED

Security Classification

AD-769919

## DOCUMENT CONTROL DATA - R &amp; D

(Security classification of title, body of abstract and indexing annotation must be entered when the overall report is classified)

1. ORIGINATING ACTIVITY (Corporate author) Northrop Corporation Aircraft Division 3901 W. Broadway, Hawthorne, California 90250		2. REPORT SECURITY CLASSIFICATION UNCLASSIFIED	
		3b. GROUP N/A	
3. REPORT TITLE  CORRELATION OF PROPERTIES AND MICROSTRUCTURE IN WELDED TITANIUM ALLOYS			
4. DESCRIPTIVE NOTES (Type of report and inclusive dates) Final Report - 15 June 1972 to 15 June 1973			
5. AUTHOR(S) (First name, middle initial, last name)  K. C. Wu			
6. REPORT DATE September 1973	7a. TOTAL NO. OF PAGES 111 128	7b. NO. OF REFS 10	
8a. CONTRACT OR GRANT NO. F33615-72-C-2015	8b. ORIGINATOR'S REPORT NUMBER(S) NOR 73-110		
8c. PROJECT NO. 7351			
8d. Task No. 735102	8e. OTHER REPORT NO(S) (Any other numbers that may be assigned this report) AFML-TR-73-202		
10. DISTRIBUTION STATEMENT  APPROVED FOR PUBLIC RELEASE; DISTRIBUTION UNLIMITED			
11. SUPPLEMENTARY NOTES		12. SPONSORING MILITARY ACTIVITY Air Force Materials Laboratory AFML/LLM Wright-Patterson AFB, Ohio 45433	
13. ABSTRACT The purpose of this program was to conduct a systematic investigation to correlate the metallurgical reactions during welding to the mechanical properties and microstructures in a Ti-6Al-6V-2Sn weldment. Welding heat-input, material thickness, thermal conductivity, and tooling configuration all affect cooling rates in a weldment, and the critical area in titanium-alloy weldments usually is the region where peak temperatures lie between 2500F and the liquidus temperature. Therefore, a set of continuous cooling transformation diagrams, along with related information on microstructure and mechanical properties was prepared to cover all important conditions resulting from the welding processes. Mechanical properties and microstructures resulting from various welding processes and parameters were studied, and the optimum welding parameters and heat-treatments were determined. The effect of long-term thermal exposure was also evaluated.  To study the fusion-zone microstructure resulting from various welding processes (cooling rates) and its mechanical properties, four welding processes, manual gas tungsten-arc welding (GTAW), plasma arc welding (PAW), automatic gas tungsten-arc welding (GTAW), and electron beam welding (EBW), were used. In addition, the automatic GTAW process with dual filler-metal was used to determine the influence of fusion-zone composition on microstructure and mechanical properties.  Thermal cycles in the heat-affected zone (HAZ) near the fusion line were measured for the four welding processes and the cooling rates from 2500F were interpolated or extrapolated. Thus, a correlation between welding processes, cooling rates, and the			

DD FORM 1473  
1 NOV 65

Reproduced by  
NATIONAL TECHNICAL  
INFORMATION SERVICE  
U S Department of Commerce  
Springfield VA 22151

UNCLASSIFIED  
Security Classification

128

UNCLASSIFIED

Security Classification

14	KEY WORDS	LINK A		LINK B		LINK C	
		ROLE	WT	ROLE	WT	ROLE	WT
	Ti-6Al-6V-2Sn Continuous Cooling Transformation Welding Microstructure Mechanical Properties						

ia

UNCLASSIFIED

Security Classification

13. Abstract (Continued)

continuous-cooling transformation diagram (CCT) was established and the relationships between the characteristics of welding processes and CCT diagrams could be identified.

The transformation products in the simulated heat-affected zones and fusion zones were identified. It was found that decreases in tensile ductility and fracture toughness were attributable to increased amounts of alpha-prime ( $\alpha'$ ) and decreased  $\alpha$ -platelet thicknesses transformed from beta ( $\beta$ ) upon cooling. The  $\alpha'$  influenced fracture toughness more than stress-corrosion resistance. For instance, an increase of  $\alpha'$  content from 10% (manual GTA-welded fusion zone) to 78% (electron-beam welded fusion zone) decreased fracture toughness from 50 ksi $\sqrt{\text{in}}$  to 34 ksi $\sqrt{\text{in}}$ , but only decreased stress-corrosion resistance from 42 ksi $\sqrt{\text{in}}$  to 31 ksi $\sqrt{\text{in}}$ . The fatigue strength of the welds was primarily dependent upon the yield strength of the weld. By adding Ti-75A filler-metal, the tensile yield strength decreased from 158 ksi to 146 ksi, and the fatigue strength at  $5 \times 10^6$  cycles decreased from 50 ksi to 40 ksi. Although the addition of Ti-75A decreased the tensile yield and fatigue strengths, fracture toughness and stress-corrosion resistance were increased.

Postweld heat-treatment of the automatic GTA welds at 1400F for 4 hours produced a modest reduction in tensile yield strength from 158 ksi to 147 ksi, but increased elongation from 3.5% to 11.8% and fracture toughness from 44 ksi $\sqrt{\text{in}}$  to 57 ksi $\sqrt{\text{in}}$ . However, the stress-corrosion resistance remained about the same (36 ksi $\sqrt{\text{in}}$ ) despite the heat-treatment. Thermal exposure of the postweld heat-treated GTA welds at 500F for 1000 hours produced minor reductions in mechanical properties and a significant reduction in stress-corrosion resistance. These effects were believed to be caused by fine precipitates.

The results obtained from this investigation indicate that: (1) a high heat-input process or the use of preheat to decrease cooling rates will produce a ductile, tough, stress-corrosion resistant weld with a small reduction in tensile yield and fatigue strength; (2) if a low heat-input process is necessary, then postweld heat-treatment at 1400F-1600F for 4 hours will produce a weld with a tensile yield strength of 147 ksi and a minimum fracture toughness of 57 ksi $\sqrt{\text{in}}$ ; or (3) the addition of Ti-75A filler-metal to the molten pool will provide a weld with a tensile yield strength of 146 ksi with a fracture toughness of 68 ksi $\sqrt{\text{in}}$ .

it

NOTICE

When Government drawings, specifications, or other data are used for any purpose other than in connection with a definitely related Government procurement operation, the United States Government thereby incurs no responsibility nor any obligation whatsoever; and the fact that the Government may have formulated, furnished, or in any way supplied the said drawings, specifications, or other data, is not to be regarded by implication or otherwise as in any manner licensing the holder or any other person or corporation, or conveying any rights or permission to manufacture, use, or sell any patented invention that may in any way be related thereto.

ADMISSION for

WHITE SECTION ☒

COPY SECTION ☐

UNANNOUNCED NOTIFICATION

BY DISTRIBUTION/ADVISABILITY CODES

Date ATLANTA HQ of Special

A

Copies of this report should not be returned unless return is required by security considerations, contractual obligations, or notice on a specific document.

ic

**CORRELATION OF PROPERTIES AND MICROSTRUCTURE  
IN WELDED TITANIUM ALLOYS**

K. C. Wu

Approved for public release; distribution unlimited.

id

## FOREWORD

This report was prepared by the Northrop Corporation, Aircraft Division, Hawthorne, California under USAF Contract No. F33615-72-C-2015. The contract work was initiated under Project No. 7351, "Metallic Materials," Task No. 735102, "Welding and Brazing of Metals Components for Military Aerospace Structures and Jet Engine," and was administered under the direction of the Metals and Ceramics Division, Air Force Materials Laboratory, Air Force Systems Command, Wright-Patterson Air Force Base, Ohio, with Captain R. P. Simpson (AFML/LLM), as Project Engineer.

This report covers work conducted during the period of 15 June 1972 through 15 June 1973. The report was submitted by the author in July 1973.

Northrop Corporation, Aircraft Division, was the contractor with K. C. Wu as the Principal Investigator directing all activities. This report has been assigned Northrop Report Number NOR 73-110 for internal control purposes.

This report has been reviewed and is approved.



ROGER J. AUSTIN, Major, USAF  
Acting Chief, Metals and Processing Branch  
Metals and Ceramics Division  
Air Force Materials Laboratory

## ABSTRACT

The purpose of this program was to conduct a systematic investigation to correlate the metallurgical reactions during welding to the mechanical properties and microstructures in a Ti-6Al-6V-2Sn weldment. Welding heat input, material thickness, thermal conductivity, and tooling configuration all affect cooling rates in a weldment, and the critical area in titanium-alloy weldments usually is the region where peak temperatures lie between 2500F and the liquidus temperature. Therefore, a set of continuous cooling transformation diagrams, along with related information on microstructure and mechanical properties was prepared to cover all important conditions resulting from the welding processes. Mechanical properties and microstructures resulting from various welding processes and parameters were studied, and the optimum welding parameters and heat treatments were determined. The effect of long-term thermal exposure was also evaluated.

To study the fusion-zone microstructure resulting from various welding processes (cooling rates) and its mechanical properties, four welding processes, manual gas tungsten-arc welding (GTAW), plasma arc welding (PAW), automatic gas tungsten-arc welding (GTAW), and electron beam welding (EBW), were used. In addition, the automatic GTAW process with dual filler-metal was used to determine the influence of fusion-zone composition on microstructure and mechanical properties.

Thermal cycles in the heat-affected zone (HAZ) near the fusion line were measured for the four welding processes and the cooling rates from 2500F were interpolated or extrapolated. Thus, a correlation between welding processes, cooling rates, and the continuous-cooling transformation diagram (CCT) was established and the relationships between the characteristics of welding processes and CCT diagrams could be identified.



The transformation products in the simulated heat-affected zones and fusion zones were identified. It was found that decreases in tensile ductility and fracture toughness were attributable to increased amounts of alpha-prime ( $\alpha'$ ) and decreased  $\alpha$ -platelet thicknesses transformed from beta ( $\beta$ ) upon cooling. The  $\alpha'$  influenced fracture toughness more than stress-corrosion resistance. For instance, an increase of  $\alpha'$  content from 10% (manual GTA-welded fusion zone) to 78% (electron-beam welded fusion zone) decreased fracture toughness from 50 ksi $\sqrt{\text{in}}$  to 34 ksi $\sqrt{\text{in}}$ , but only decreased stress-corrosion resistance from 42 ksi $\sqrt{\text{in}}$  to 31 ksi $\sqrt{\text{in}}$ . The fatigue strength of the welds was primarily dependent upon the yield strength of the weld. By adding Ti-75A filler-metal, the tensile yield strength decreased from 158 ksi to 146 ksi, and the fatigue strength at  $5 \times 10^6$  cycles decreased from 50 ksi to 40 ksi. Although the addition of Ti-75A decreased the tensile yield and fatigue strengths, fracture toughness and stress-corrosion resistance were increased.

Postweld heat-treatment of the automatic GTA welds at 1400F for 4 hours produced a modest reduction in tensile yield strength from 158 ksi to 147 ksi, but increased elongation from 3.5% to 11.8% and fracture toughness from 44 ksi $\sqrt{\text{in}}$  to 57 ksi $\sqrt{\text{in}}$ . However, the stress-corrosion resistance remained about the same (36 ksi $\sqrt{\text{in}}$ ) despite the heat-treatment. Thermal exposure of the postweld heat-treated GTA welds at 500F for 1000 hours produced minor reductions in mechanical properties and a significant reduction in stress-corrosion resistance. These effects were believed to be caused by fine precipitates.

The results obtained from this investigation indicate that: (1) a high heat-input process or the use of preheat to decrease cooling rates will produce a ductile, tough, stress-corrosion resistant weld with a small reduction in tensile yield and fatigue strength; (2) if a low heat-input process is necessary, then postweld heat-treatment at 1400F-1600F for 4 hours will produce a weld with a tensile yield strength of 147 ksi and a minimum fracture toughness of 57 ksi $\sqrt{\text{in}}$ ; or (3) the addition of Ti-75A filler-metal to the molten pool will provide a weld with a tensile yield strength of 146 ksi with a fracture toughness of 68 ksi $\sqrt{\text{in}}$ .

## TABLE OF CONTENTS

	<u>Page</u>
I INTRODUCTION . . . . .	1
II MATERIALS AND TEST SPECIMEN DESIGNS . . . . .	3
III PROCEDURES AND EQUIPMENT . . . . .	5
CONSTRUCTION OF CONTINUOUS COOLING TRANSFORMATION DIAGRAM AND SIMULATION OF HEAT-AFFECTED ZONE SPECIMENS . . . . .	5
WELDING . . . . .	5
Thermal Cycle Recording . . . . .	7
Postweld Heat-Treatment . . . . .	8
Thermal Exposure . . . . .	8
MICROSTRUCTURAL STUDIES . . . . .	8
MECHANICAL TESTING . . . . .	10
Hardness Measurements . . . . .	10
Tensile Tests . . . . .	10
Fatigue Tests . . . . .	10
Fracture-Toughness and Stress-Corrosion Tests . . . . .	11
IV RESULTS AND DISCUSSIONS . . . . .	13
HEAT-AFFECTED ZONE STUDIES . . . . .	13
Continuous Cooling Transformation . . . . .	13
Effect of Cooling Rate on Microstructure and Mechanical Properties . . . . .	14
Effect of Heat-Treatment and Thermal Exposure on Syn- thetic HAZ Microstructure and Mechanical Properties . . . . .	18
FUSION ZONE STUDIES . . . . .	19
Correlation Between Heat-Input and Cooling Rate . . . . .	19
Solidification Pattern in the Fusion Zones . . . . .	20
MICROSTRUCTURE AND MECHANICAL PROPERTIES OF THE FUSION ZONES . . . . .	21
Effect of Composition Alteration on Fusion-Zone Micro- structure and Mechanical Properties. . . . .	27
Effect of Postweld Heat-Treatment on Fusion-Zone Micro- structure and Mechanical Properties . . . . .	29
Effect of Thermal Exposure on Fusion Zone Microstructure and Mechanical Properties . . . . .	31
V CONCLUSIONS . . . . .	33
VI RECOMMENDATIONS . . . . .	34
VII APPLICATION OF PROGRAM RESULTS TO PRACTICE . . . . .	35
AS-WELDED EFFECTS . . . . .	35
POSTWELD HEAT-TREATMENT EFFECTS . . . . .	37

CONTENTS (Continued)

	<u>Page</u>
EFFECTS OF CHEMICAL ALTERATION OF THE FUSION ZONE . . . . .	37
THERMAL EXPOSURE EFFECTS . . . . .	37
WELDING PROCESS SELECTION . . . . .	38
VIII REFERENCES . . . . .	40

# LIST OF TABLES

<u>TABLE</u>		<u>PAGE</u>
I	CHEMICAL COMPOSITION AND MECHANICAL PROPERTIES OF Ti-6Al-6V-2Sn PLATE (HEAT NO. 295818) AND FILLER-METAL (HEAT NO. 303492-3912) . . . . .	3
II	TENSILE, FRACTURE TOUGHNESS, AND STRESS-CORROSION DATA FOR Ti-6Al-6V-2Sn PLATE IN MA AND STA CONDITIONS . . . . .	3
III	WELDING SCHEDULES FOR MANUAL GTA, PLASMA ARC, AUTOMATIC GTA, AND ELECTRON BEAM WELDING . . . . .	7
IV	SUMMARY OF PHASE CONTENTS IN THE SYNTHETIC HEAT-AFFECTED ZONE IN VARIOUS HEAT TREATMENT CONDITIONS . . . . .	14
V	HARDNESS MEASUREMENTS IN THE SYNTHETIC HEAT-AFFECTED ZONE . . .	15
VI	SUMMARY OF $K_{Ic}$ AND $K_{Isc}$ OF THE SYNTHETIC HEAT-AFFECTED ZONE IN VARIOUS HEAT TREATED CONDITIONS . . . . .	15
VII	HEAT INPUT AND COOLING RATE FOR FOUR WELDING PROCESSES . . . . .	19
VIII	SUMMARY OF PHASE CONTENTS IN THE FUSION ZONES . . . . .	23
IX	TENSILE PROPERTIES OF WELDED Ti-6Al-6V-2Sn PLATE, AS-WELDED . . . . .	24
X	SUMMARY OF $K_{Ic}$ AND $K_{Isc}$ OF THE FUSION ZONES . . . . .	26
XI	TENSILE PROPERTIES OF Ti-6Al-6V-2Sn FUSION ZONE USING VARIOUS AMOUNTS OF Ti-75 FILLER-METAL, AS-WELDED (LONGITUDINAL TENSION ONLY, AVERAGE OF THREE). . . . .	28
XII	TENSILE PROPERTIES OF THE FUSION ZONE, AUTOMATIC GTAW POSTWELD HEAT TREATED AT 1400F - 4 HRS . . . . .	30
XIII	TENSILE PROPERTIES OF THE FUSION ZONE, AUTOMATIC GTAW, POSTWELD HEAT TREATED AT 1400F - 4 HRS PLUS 500F - 1000 HRS . .	32
XIV	SUMMARY OF THE CORRELATION OF MICROSTRUCTURE AND MECHANICAL PROPERTIES IN WELDMENT PRODUCED BY FOUR WELDING PROCESSES . . .	36

## LIST OF ILLUSTRATIONS

<u>FIGURE</u>		<u>PAGE</u>
1	S-N CURVES FOR Ti-6Al-6V-2Sn BASE METAL . . . . .	41
2	BASE METAL MICROSTRUCTURE, AS-RECEIVED (MILL ANNEALED) . . . .	42
3	BASE METAL MICROSTRUCTURE, SOLUTION-TREATED 1650F - 1HR, WATER QUENCH . . . . .	43 43
4	BASE METAL MICROSTRUCTURE, SOLUTION TREATED 1650F - 1 HR, WATER QUENCH, AND AGED 1050F - 4 HRS . . . . .	44
5	CONFIGURATION OF MECHANICAL TEST SPECIMENS . . . . .	45
6	THE GLEEBLE . . . . .	46
7	JOINT CONFIGURATION FOR AUTOMATIC AND MANUAL GTA WELDING . .	47
8	MANUAL GTA WELDING SET-UP IN AN ATMOSPHERE CHAMBER . . . . .	48
9	AUTOMATIC GTA WELDING EQUIPMENT MODIFIED FOR DUAL FILLER-METAL PROCESS . . . . .	48
10	MANUAL GTA WELDED PLATE . . . . .	49
11	PLASMA ARC WELDED PLATE . . . . .	49
12	AUTOMATIC GTA WELDED PLATE . . . . .	50
13	ELECTRON BEAM WELDED PLATE . . . . .	50
14	WELDING PLATE SET-UP FOR RECORDING THERMAL CYCLES IN THE HEAT-AFFECTED ZONE . . . . .	51
15	X-RAY DIFFRACTION INTENSITY RECORDING FOR ALPHA PHASE IN A HEAT-AFFECTED ZONE SPECIMEN COOLED FROM 2500F AT A COOLING RATE OF 366F/SEC . . . . .	52
16	REVERSE BENDING FATIGUE TEST IN PROGRESS . . . . .	53
17	STRESS-CORROSION TEST SET-UP . . . . .	54
18	CONTINUOUS COOLING TRANSFORMATION DIAGRAM FOR Ti-6Al-6V-2Sn .	55
19	MICROSTRUCTURE OF SYNTHETIC HEAT-AFFECTED ZONE COOLED AT 366F/SECOND . . . . .	56
20	MICROSTRUCTURE OF SYNTHETIC HEAT-AFFECTED ZONE COOLED AT 110F/SECOND . . . . .	56

# ILLUSTRATIONS (Continued)

<u>FIGURE</u>		<u>PAGE</u>
21	MICROSTRUCTURE OF SYNTHETIC HEAT-AFFECTED ZONE COOLED AT 25F/SECOND . . . . .	57
22	EFFECT OF COOLING RATE ON PHASE CONTENTS IN THE SYNTHETIC HEAT-AFFECTED ZONE COOLED FROM 2500F IN AS-CYCLED, HEAT TREATED, AND THERMALLY EXPOSED CONDITIONS . . . . .	58
23	EFFECT OF COOLING RATE ON PHASE CONTENTS IN THE SYNTHETIC HEAT-AFFECTED ZONE BEFORE AND AFTER HEAT-TREATMENT AT 1600F - 2 HRS . . . . .	59
24	EFFECT OF COOLING RATE AND POST-CYCLE HEAT TREATMENT ON FRACTURE TOUGHNESS IN THE SYNTHETIC HEAT-AFFECTED ZONE . . .	60
25	EFFECT OF COOLING RATE AND POST-CYCLE HEAT-TREATMENT ON STRESS-CORROSION RESISTANCE IN THE SYNTHETIC HEAT-AFFECTED ZONE . . . . .	61
26	EFFECT OF PHASE CONTENTS ON FRACTURE TOUGHNESS OF THE SYNTHETIC HEAT-AFFECTED ZONE, ALL CONDITIONS . . . . .	62
27	EFFECT OF PHASE CONTENTS ON STRESS-CORROSION RESISTANCE OF THE HEAT-AFFECTED ZONE, ALL CONDITIONS . . . . .	63
28	EFFECT OF COOLING RATE ON STRESS-CORROSION SUSCEPTIBILITY RATIO OF THE SYNTHETIC HEAT-AFFECTED ZONE, ALL CONDITIONS . . . .	64
29	EFFECT OF PHASE CONTENTS ON STRESS-CORROSION SUSCEPTIBILITY RATIO OF THE SYNTHETIC HEAT-AFFECTED ZONE, ALL CONDITIONS . .	65
30	FRACTURE SURFACE OF A SYNTHETIC HEAT-AFFECTED ZONE SPECIMEN COOLED AT 366F/SEC AND FRACTURE-TOUGHNESS TESTED . . . . .	66
31	FRACTURE SURFACE OF A SYNTHETIC HEAT-AFFECTED ZONE SPECIMEN COOLED AT 25F/SEC, HEAT TREATED AT 1600F FOR 2 HRS AND FRACTURE-TOUGHNESS TESTED . . . . .	67
32	FRACTURE SURFACE OF A SYNTHETIC HEAT-AFFECTED ZONE SPECIMEN COOLED AT 25F/SEC AND STRESS-CORROSION TESTED . . . . .	68
33	FRACTURE SURFACE OF A SYNTHETIC HEAT-AFFECTED ZONE SPECIMEN COOLED AT 25F/SEC, HEAT TREATED AT 1600F FOR 2 HRS AND STRESS-CORROSION TESTED . . . . .	69
34	SYNTHETIC HEAT-AFFECTED ZONE, 366F/SEC, 1400F - 4 HRS . . . .	70
35	SYNTHETIC HEAT-AFFECTED ZONE, 110F/SEC, 1400F - 4 HRS . . . .	70

# ILLUSTRATIONS (Continued)

<u>FIGURE</u>		<u>PAGE</u>
36	SYNTHETIC HEAT-AFFECTED ZONE, 25F/SEC, 1400F - 4 HRS . . . . .	71
37	SYNTHETIC HEAT-AFFECTED ZONE, 366F/SEC, 1600F - 2 HRS . . . . .	71
38	SYNTHETIC HEAT-AFFECTED ZONE, 110F/SEC, 1600F - 2 HRS . . . . .	72
39	SYNTHETIC HEAT-AFFECTED ZONE, 25F/SEC, 1600F - 2 HRS . . . . .	72
40	SYNTHETIC HEAT-AFFECTED ZONE, 366F/SEC, 1400F - 4 HRS PLUS 500F - 1000 HRS . . . . .	73
41	SYNTHETIC HEAT-AFFECTED ZONE, 110F/SEC, 1400F - 4 HRS PLUS 500F - 1000 HRS . . . . .	73
42	SYNTHETIC HEAT-AFFECTED ZONE, 25F/SEC, 1400F - 4 HRS PLUS 500F - 1000 HRS . . . . .	74
43	SOLIDIFICATION PATTERN OF A WELD BEAD, MANUAL GTAW PROCESS . .	75
44	MACROSTRUCTURE AND HARDNESS MEASUREMENTS IN A MANUAL GTA WELD USING Ti-6Al-6V-2Sn FILLER METAL . . . . .	76
45	MICROSTRUCTURE IN THREE DIRECTIONS OF THE Ti-6Al-6V-2Sn FUSION ZONE USING MATCHING FILLER METAL, MANUAL GTAW PROCESS, AS-WELDED . . . . .	77
46	SOLIDIFICATION PATTERN OF A WELD BEAD, PLASMA ARC WELDING PROCESS . . . . .	78
47	MACROSTRUCTURE AND HARDNESS MEASUREMENTS IN A PLASMA ARC WELD WITHOUT FILLER METAL . . . . .	79
48	MICROSTRUCTURE IN THREE DIRECTIONS OF THE Ti-6Al-6V-2Sn FUSION ZONE WITHOUT FILLER METAL, PLASMA ARC WELDING PROCESS, AS-WELDED . . . . .	80
49	SOLIDIFICATION PATTERN OF A WELD BEAD, AUTOMATIC GTAW PROCESS . . . . .	81
50	MACROSTRUCTURE AND HARDNESS MEASUREMENTS IN AN AUTOMATIC GTA WELD USING Ti-6Al-6V-2Sn FILLER METAL . . . . .	82
51	MICROSTRUCTURE IN THREE DIRECTIONS OF THE Ti-6Al-6V-2Sn FUSION ZONE MATCHING FILLER METAL, AUTOMATIC GTAW PROCESS, AS-WELDED . . . . .	83
52	SOLIDIFICATION PATTERN OF A WELD BEAD, ELECTRON BEAM WELDING PROCESS . . . . .	84

# ILLUSTRATIONS (Continued)

<u>FIGURE</u>		<u>PAGE</u>
53	MACROSTRUCTURE AND HARDNESS MEASUREMENTS IN AN ELECTRON BEAM WELD WITHOUT FILLER METAL . . . . .	85
54	MICROSTRUCTURE IN THREE DIRECTIONS OF THE Ti-6Al-6V-2Sn FUSION ZONE WITHOUT FILLER METAL, ELECTRON BEAM WELDING PROCESS, AS-WELDED . . . . .	86
55	FUSION ZONE MICROSTRUCTURE, MANUAL GTAW, AS-WELDED . . . . .	87
56	FUSION ZONE MICROSTRUCTURE, PLASMA ARC WELDING, AS-WELDED . . . . .	87
57	FUSION ZONE MICROSTRUCTURE, AUTOMATIC GTAW, AS-WELDED . . . . .	88
58	FUSION ZONE MICROSTRUCTURE, ELECTRON BEAM WELDING, AS-WELDED . . . . .	38
59	EFFECT OF COOLING RATE ON PHASE CONTENTS IN FUSION ZONES, AS-WELDED . . . . .	89
60	TENSILE YIELD-ELONGATION RELATIONSHIP FOR THE FUSION ZONES PRODUCED BY VARIOUS WELDING PROCESSES AND HEAT TREATMENTS . . . . .	90
61	TENSILE YIELD-FRACTURE TOUGHNESS RELATIONSHIP FOR THE FUSION ZONES PRODUCED BY VARIOUS WELDING PROCESSES AND HEAT TREATMENTS . . . . .	91
62	S-N DATA FOR Ti-6Al-6V-2Sn WELDS . . . . .	92
63	FRACTURE SURFACE OF THE FATIGUE TESTED SPECIMENS . . . . .	93
64	EFFECT OF COOLING RATE ON FRACTURE TOUGHNESS AND STRESS-CORROSION RESISTANCE OF FUSION ZONES . . . . .	94
65	EFFECT OF PHASE CONTENTS ON FRACTURE TOUGHNESS OF FUSION ZONES, ALL CONDITIONS . . . . .	95
66	EFFECT OF PHASE CONTENTS ON STRESS-CORROSION RESISTANCE OF FUSION ZONES, ALL CONDITIONS . . . . .	96
67	FRACTURE SURFACE OF A MANUAL GTA WELDED FUSION ZONE, FRACTURE-TOUGHNESS TESTED . . . . .	97
68	FRACTURE SURFACE OF AN ELECTRON BEAM WELDED FUSION ZONE, FRACTURE TOUGHNESS TESTED . . . . .	98
69	FRACTURE SURFACE OF A MANUAL GTA WELDED FUSION ZONE, STRESS-CORROSION TESTED . . . . .	99



# ILLUSTRATIONS (Continued)

<u>FIGURE</u>		<u>PAGE</u>
70	FRACTURE SURFACE OF AN ELECTRON BEAM WELDED FUSION ZONE, STRESS-CORROSION TESTED . . . . .	100
71	MACROSTRUCTURE AND HARDNESS MEASUREMENTS IN AN AUTOMATIC GTA WELD USING 50% Ti-662 and 50% Ti-75A FILLER METAL . . . .	101
72	MACROSTRUCTURE AND HARDNESS MEASUREMENTS IN AN AUTOMATIC GTA WELD USING 100% Ti-75A FILLER METAL . . . . .	102
73	FUSION ZONE MICROSTRUCTURE, AUTOMATIC GTAW, 50% Ti-662 and 50% Ti-75A FILLER METAL . . . . .	103
74	FUSION ZONE MICROSTRUCTURE, AUTOMATIC GTAW, 100% Ti-75A FILLER METAL . . . . .	103
75	ELECTRON MICROPROBE TRACE FOR DUAL FILLER-METAL WELDED FUSION ZONES . . . . .	104
76	S-N DATA FOR Ti-6Al-6V-2Sn WELDS USING DUAL FILLER-METAL . . .	105
77	EFFECT OF FILLER METAL ON FRACTURE TOUGHNESS AND STRESS-CORROSION RESISTANCE (AUTOMATIC GTAW) . . . . .	106
78	MACROSTRUCTURE AND HARDNESS MEASUREMENTS IN AN AUTOMATIC GTA WELD USING Ti-662 FILLER METAL, HEAT TREATED AT 1400F - 4 HRS . . . . .	107
79	FUSION ZONE MICROSTRUCTURE, AUTOMATIC GTAW, Ti-662 FILLER METAL, 1400F - 4 HRS . . . . .	108
80	S-N DATA FOR Ti-6Al-6V-2Sn WELDS, AUTOMATIC GTA WELDED . . .	109
81	MACROSTRUCTURE AND HARDNESS MEASUREMENTS IN AN AUTOMATIC GTA WELD, 1400F - 4 HRS PLUS 500F - 1000 HRS . . . . .	110
82	FUSION ZONE MICROSTRUCTURE, AUTOMATIC GTAW, 1400F - 4 HRS PLUS 500F - 1000 HRS . . . . .	111

# I

## INTRODUCTION

Because of their superior mechanical properties, titanium alloys are being applied in increasing quantities to high-performance aircraft. Although welding is an important technique for the fabrication of titanium structures and welding studies of titanium alloys were started more than a decade ago, a systematic welding program has not been conducted. Welding metallurgy has rarely been used as a basis for improving the performance of weldments in service, and mechanical properties of titanium weldments have seldom been correlated with titanium microstructures.

It was found in previous studies<sup>(1,2)</sup> that alpha-beta titanium alloys are cooling-rate sensitive. High cooling rates produce more  $\alpha'$ , which lowers toughness and reduces weldability. Slow cooling rates promote the growth of  $\alpha$  plates that enrich the  $\beta$  phase with  $\beta$  stabilizers. The enriched  $\beta$  phase has a lower  $M_s$  temperature and hence, a lower tendency to transform to  $\alpha'$ , preferring to remain at room temperature as retained  $\beta$ . Large, tough  $\alpha$  plates divert crack propagation paths and possibly reduce crack propagation by blunting the crack tip. On the other hand, thin martensitic  $\alpha'$  plates will provide a poorer medium for energy absorption and limit resistance to crack propagation.

Welding processes characteristically deliver various amounts of heat energy in terms of heat-input in Joules per inch. Welding processes of low heat-input such as electron beam welding cause high cooling rates that result in low-toughness welds. Welding processes of high heat-input such as manual gas tungsten-arc welding produce low cooling rates which result in tougher weldments. Other mechanical properties are influenced by cooling rates as well.

The construction of a continuous cooling transformation diagram from a critical peak temperature provides a convenient method for correlating welding processes, heat input, cooling rate, microstructure, and mechanical properties. Once the effect of cooling rate (welding process) is determined, postweld heat-treatments for improving mechanical properties can be explored, if needed, in a systematic manner.

The major difference between the fusion and heat-affected zones in a weldment is the grain structure and alloy partitioning caused by the additional melting and solidification processes. The solidification pattern is influenced by the temperature gradient and solidification rate which are characteristic of each welding process.

By recording the cooling rates in various welding processes and relating the range of cooling rates for each welding process to the continuous cooling transformation diagram, one may predict the mechanical properties of titanium alloys produced by any welding process.

If and when this work covers all commercially available, technically-significant titanium alloys, a welding metallurgy handbook can be prepared. From this handbook, welding engineers can easily choose an appropriate welding process and postweld heat-treatment to fulfill specific service requirements.

## II

### MATERIALS AND TEST SPECIMEN DESIGNS

Four plates of 0.350-inch by 36-inch by 72-inch Ti-6Al-6V-2Sn were obtained from RMI, Inc., and ten pounds of 0.040-inch diameter Ti-6Al-6V-2Sn filler-metal was procured from Alloy Industries, Inc., Both were in the mill annealed (1350F - 15 min., AC) condition. The chemical compositions are listed in Table I.

TABLE I  
CHEMICAL COMPOSITION OF Ti-6Al-6V-2Sn PLATE (HEAT NO. 295818)  
AND FILLER-METAL (HEAT NO. 303492-3912)

	CHEMICAL COMPOSITION, %									
	C	N	Fe	Al	V	Sn	Cu	O	H	Ti
PLATE	.02	.011	.67	5.5	5.6	2.0	.63	.155	47(PPM)	Bal.
FILLER METAL	.01	.010	.82	5.6	5.6	2.3	.75	.162	22(PPM)	Bal.

The base metal in the mill annealed condition and solution-treated and aged (STA) condition (1650F - 1 hr., WQ and 1050F - 4 hrs., AC) was characterized by tension, fracture toughness, and stress-corrosion tests (Table II), and fatigue tests. The configuration of the tensile test specimens followed the Federal Standard, Method 211, Type F-2.

TABLE II  
TENSILE\*, FRACTURE TOUGHNESS, AND STRESS CORROSION DATA FOR  
Ti-6Al-6V-2Sn PLATE IN MA AND STA CONDITIONS

	YIELD STRENGTH .2% KSI	ULT. STRENGTH KSI	ELONGATION % (2 in.)	K <sub>IC</sub> KSI $\sqrt{\text{IN}}$	K <sub>ISCC</sub> KSI $\sqrt{\text{IN}}$
MA	152.7	161.2	13.0	44	35
STA	186.3	195.9	5.0	24	21

\* Longitudinal Direction

Fatigue data for the base metal in the MA and STA conditions are shown in Figure 1. The high-cycle fatigue strength was equal in both conditions, about 60 ksi, although the MA condition provided better low-cycle fatigue strength.

Microstructures of the base metal in the MA, ST, and STA conditions are shown in Figures 2 through 4. X-ray diffraction measurements indicated that the base metal contained 93%  $\alpha$  and 7%  $\beta$  in the MA condition and 94%  $\alpha$  and 6%  $\beta$  in the STA condition.

Mechanical tests conducted in this program were tension in the longitudinal (to the fusion zone) and transverse (to the fusion zone) orientations, fracture toughness, stress-corrosion, and longitudinal reverse-bending fatigue. For heat-affected zone specimens, only fracture-toughness and stress-corrosion tests were conducted. The dimensions of test specimens is shown in Figure 5.

### III PROCEDURES AND EQUIPMENT

#### CONSTRUCTION OF CONTINUOUS COOLING TRANSFORMATION DIAGRAM AND SIMULATION OF HEAT-AFFECTED ZONE SPECIMENS

Blanks for mechanical tests and microstructural analyses were 0.80-inch wide and 4.0 inches long by 0.35-inch thick; they were heated to 2500F in the Gleeble (Figure 6), held at this temperature for four seconds, and then cooled to room temperature at six different cooling rates: 366F/sec, 280F/sec, 160F/sec, 110F/sec, 64F/sec, and 25F/sec. A high-speed dilatometer and Pt/Pt-10Rh thermocouple (0.010-inch diameter wire) were attached to each specimen for recording specimen dilation and thermal cycle on an oscillograph. The transformation temperature was determined at the deflection point on the dilation trace. After thermal cycling, the blanks for fracture-toughness and stress-corrosion tests were machined on all four sides to yield specimens 0.75-inch wide by 4.0 inches long by 0.25-inch thick. Thus, the oxidized layer produced by thermal cycling was removed completely.

Specimens in each cooling-rate group were divided into four subgroups of three each. Each subgroup was tested in a different condition: (1) as-cycled, (2) cycled plus 1400F for 4 hours, (3) cycled plus 1600F for 2 hours, and (4) cycled plus 1400F for 4 hours plus 500F for 1000 hours.

#### WELDING

Four welding processes, manual GTA, plasma arc, automatic GTA, and electron beam welding, were used. Plates were sheared into blanks on a power shear, and the shear lips were machined off during preparation of weld joints or test specimens. The double-vee joint configuration used for manual and automatic GTA welding is shown in Figure 7. For electron beam and plasma arc welding, square butt joints having a 16  $\mu$  finish and 63  $\mu$  finish, respectively, were used.

Before welding, printed letters on the plates were removed by rubbing with cleanser and plastic abrasive pads. Then, the plates were degreased in acetone and chemically cleaned in a 30%  $\text{HNO}_3$ -3% HF water solution, rinsed in de-ionized water, and wiped dry.

Manual GTA welding was conducted in an atmosphere chamber using the welding set-up shown in Figure 8. The chamber was thoroughly purged with argon. For practical purposes, a root pass was made to melt the lands together so that full penetration could be obtained in subsequent passes. Then, welding was performed on both sides, one after another, using matching filler metal. Because of the maneuvering, welding current and arc voltage were not recorded. The travel speed was about 2 inches/minute.

Plasma arc welding was conducted on an Airline Welding Positioner using a 400-ampere AC-DC power supply. The plasma arc torch was a Model PWM4A, and the control console was a Model WC100, manufactured by Thermal Dynamics Corporation. Welding current was recorded on an Esterline Angus recorder. Arc voltage was measured between terminals at the control panel and the ground.

The automatic GTA welding was conducted on the same positioner upon which an arc voltage feed-back controlled torch was installed. Welding power was supplied by a 400-ampere AC-DC power supply. The welding current and arc voltage were recorded on Esterline Angus recorders. The back-up bar was made of stainless steel. Single-pass welding was attempted to obtain a weld with a single thermal cycle. Although numerous joint geometries and welding schedules were used, a satisfactory weld could not be obtained. Therefore, the double-V weld joint was selected for its simplicity of machining and the balancing of residual stress to minimize distortion.

Automatic GTA dual filler-metal welding was performed using the same welding positioner and equipment and welded from both sides. Direct current, straight polarity was used. For 100% Ti-75A filler-metal welding, the wire-feed speed was the same as that for the matching filler-metal, 42 IPM. To achieve the 50% Ti-75A and 50% Ti-662 ratio in the deposit, these two filler-metals were fed at 21 IPM each. The dual filler-metal welding equipment is shown in Figure 9.

Electron beam welding was performed at Electron Beam Welding, Inc., Los Angeles under Northrop supervision. The welding machine was a Hamilton Standard unit. Visual inspection and X-ray radiography indicated that all welds had 100% penetration, no under-cutting or cracks, and freedom from porosity.

Welded plates are shown in Figures 10 through 13 before machining into test specimens.

The welding schedules for the manual GTA, plasma arc, automatic GTA, and electron beam welding are shown in Table III.

Welds were inspected using X-ray radiography which showed no indication of defects. Then, the welded plates were sheared into blanks and machined into various types of test specimens. A layer of approximately 0.050-inch of metal on both sides was removed by machining to reach the specified thickness of 0.250-inch. These inspection and machining procedures were applied to all the weldments.

TABLE III  
WELDING SCHEDULES FOR AUTOMATIC GTA, MANUAL GTA,  
PLASMA ARC, AND ELECTRON BEAM WELDING

PROCESS	TRAVEL IN/MIN	ARC VOLTAGE V	WELDING CURRENT A	TORCH CU.FT./HR.	SHIELD GAS CU.FT./HR.	TRAILING GAS CU.FT./HR.	BACK-UP GAS CU.FT./HR.	WIRE FEED IN/MIN
Manual GTA	2 Approx.	8-11	*Vary	-	-	-	-	Manu.
Plasma Arc	6	30	* 180	30	4	60	20	None
Electron Beam	40	130x10 <sup>3</sup>	35x10 <sup>-3</sup>	-	-	-	-	None
Auto. GTA	6	9-10	*260-270	20	-	50	15	42

\*DC Straight Polarity

#### Thermal Cycle Recording

To determine the cooling rate from 2500F for each welding process employed in this program, the thermal cycle near the fusion line was recorded. Six 0.010-inch in diameter Pt/Pt-10Ph thermocouples were percussion welded in the vicinity of the predicted fusion line. The set-up of the welding plate for thermal-cycle recording is shown in Figure 14. The same welding parameters for preparation of test specimens were used for thermal cycling. Thermal cycles were recorded on a multi-channel Honeywell Visicorder, Model 406C. The cooling rate at 2500F was obtained either by interpolating or extrapolating from a cooling rate versus peak-temperature plot.



### Postweld Heat-Treatment

Either simulated heat-affected zone blanks or weldments were machined to their final dimensions before heat-treatment. Two heat-treatments, 1400F for 4 hours and 1600F for 2 hours, followed by air cooling, were selected for heat-affected zone specimens. Since a 1200F heat-treatment<sup>(3)</sup> did not improve HAZ toughness, heat-treatment temperatures higher than this were required. A treatment of 1400F for 4 hours is simple and can be conducted in air without serious oxidation. In this program, all heat-treatments were conducted in a vacuum furnace operating at approximately  $10^{-5}$  torr.

If a weldment can be heat treated at higher temperatures in air or an inert atmosphere, then a treatment of 1600F for 2 hours may be practical. The 1600F heat-treatment improves toughness and ductility tremendously from the as-welded condition, but it is not quite as effective as the triplex treatment used by Simpson and Wu<sup>(4)</sup>. The 1600F treatment was selected for this program, however, because of its simplicity.

For fusion zone specimens, only one heat-treatment, 1400F for 4 hours, was used. This treatment produced a microstructure possessing the lower limit of toughness obtained from the postweld heat-treatments used in this program.

### Thermal Exposure

To determine the thermal stability of these weldments, both simulated heat-affected zone and fusion-zone specimens were exposed in air at 500F for 1000 hours. After exposure, specimens were subjected to tensile, fatigue, fracture-toughness, and stress-corrosion tests.

### MICROSTRUCTURAL STUDIES

Microstructural studies conducted in this program included optical photomacrography, optical photomicrography, electron microprobe, X-ray diffraction, and scanning electron microscopy (SEM).

Photomacrographs were taken between 5X and 20X using a Baush and Lomb camera for fracture toughness and stress-corrosion fracture surfaces. Specimens for microstructural studies were polished through 4-0 paper, nylon wheel with Linde A  $0.3\mu$  aluminum oxide slurry mixed with ammonia fluoride solution, and polished on microcloth with a Linde A slurry in water. Kroll's etch was used for micro-etching. For macrostructure studies, electrolytic etching (Disa-Electropol 3A solution) was employed. Etching current was 1-2 amperes at an etching voltage of 25V. Etching time was 5 seconds at each stop for a total of 20 seconds. A Leitz MM5 metallograph was used for all photomicrographs.

Electron microprobe analysis was performed on the Perkin-Elmer XMA-5 microprobe to measure the chemical gradients in welds produced with dual filler metal. The sample was usually moved in increments of  $500\mu$  to determine its chemical profile. Ti, Al, Sn, and V were measured quantitatively by two methods: (1) comparison of base metal chemistry to HAZ or fusion zone chemistry intensities or (2) comparison with pure elemental standards and use of correction-factor calculations.

X-ray diffraction techniques were applied to study phase transformation. A Norelco X-ray diffractometer and filtered Cu  $K\alpha$  radiation were used for all examinations. The one-degree slit and the receiver slit were used with a proportional counter tube. A 50-KV potential and a 20-MA current on the tube was used.

Because of the very low intensity of  $\alpha'$  and  $\alpha$  peaks from the  $(21\bar{1}1)$  plane, a slow-scanning, point-to-point counting method was used to obtain a recording trace, as shown in Figure 15. The diffraction plane for  $\beta$  phase was  $(110)$  at the  $2\theta$  angle of approximately 40 degrees. The calculations of weight percentages of  $\alpha$ ,  $\alpha'$ , and  $\beta$  were made by measuring the area under  $\alpha$ ,  $\alpha'$ , and  $\beta$  (not shown) peaks. The area under each peak was divided by the theoretical structure factor to obtain relative weights from which weight percentages were calculated. This approach assumed that only  $\alpha$ ,  $\alpha'$ , and  $\beta$  were present in the microstructures.

Scanning electron fractography was performed on the JEOLCO JSM-2 microscope. Specimens were sectioned to 1/2-inch in height. The angle of incidence was 80 degrees. Representative fractographs were taken at 700X and 2100X.

## MECHANICAL TESTING

### Hardness Measurements

Rockwell C-scale was used for hardness measurements to meet industrial practices. When the microstructure varied in a small region, Knoop microhardness measurements were used and Knoop hardness numbers were converted to Rockwell C numbers. Five measurements were made on each specimen to obtain an average hardness value.

### Tensile Tests

A grid was printed on the reduced section of each tensile specimen to register the local elongation in the weld. However, no significant variation in local elongation or lateral contraction was observed. Tests were conducted on a standard tensile test machine at a cross-head speed of 0.05 in/min. A stress-strain curve was recorded for each specimen from which the yield strength and Young's modulus were determined. Elongation was measured within a 2-inch gage length. Three specimens were tested for each condition.

### Fatigue Tests

Composite weldments were subjected to four-point reverse-bending fatigue tests on a Baldwin SF-1-U fatigue machine (1800 cpm). The fatigue test equipment with a specimen in test is shown in Figure 16. The four-point reverse bending applies the same tensile and compressive stresses to the face and the root of the weld as well as to all three zones. The least fatigue-resistant zone fails first, and the fatigue crack propagates through the remaining areas.

The maximum stress is obtained from the equation:  $F = \frac{AW}{2S}$

F is maximum stress, in psi

W is load setting on the machine, in lbs.

S is sectional modulus =  $\frac{bd^2}{6}$ ; b is width, d is thickness, both in inches

A is span between inside loading posts, in inches

The fatigue strength was defined as the stress at which two specimens did not fail at or greater than 5 million cycles or at which one specimen did fail but one out of two specimens did not fail at or greater than 5 million cycles at 5,000 psi above this stress.

#### Fracture-Toughness and Stress-Corrosion Tests

The development of plane-strain fracture mechanics provides a recognized method for determining the toughness of parent materials. This same approach may be used on weldments, provided that due consideration is given to the varying microstructures existing from the fusion zone through the heat-affected zone. The use of fatigue-cracked fracture-mechanics specimens for toughness tests is also a convenience because the same types of specimens are needed to conduct stress-corrosion tests in salt water.

The precracked single-edge-notch specimen shown in Figure 5 was used to determine the stress-corrosion behavior and fracture toughness of the base metal, simulated heat-affected zone, and fusion zone. This specimen configuration closely resembles design recommendations by Srawley and Brown<sup>(5)</sup> and Payne<sup>(6)</sup> for plane-strain fracture toughness tests. The synthetic HAZ specimens were thermally cycled before notching in order to maintain a constant cross-section for uniform resistance heating in the Gleeble. Precracking was conducted on a Baldwin SF-1-U fatigue machine at a frequency of 1800 cpm. Crack propagation rate was controlled so that the minimum time for the crack to reach a length of 0.20-inch (from the edge of the specimen) was 10-15 minutes. Then, the load was reduced to meet the ASTM specification:  $K_I(\text{max})/E \geq 0.002\sqrt{a}$  to extend the crack to a total length of 0.250-inch. Precracked specimens were stored in a dessicator before testing. Tests were conducted on an Instron machine, and the procedure met ASTM E-399-72 specifications.  $K_{Ic}$  was calculated using the equation:  $K_{Ic} = \frac{P}{BW^{3/2}} F\left(\frac{A}{W}\right)$

where:

$$F\left(\frac{A}{W}\right) = 1.99\left(\frac{A}{W}\right)^{3/2} - .41\left(\frac{A}{W}\right)^{3/2} + 18.70\left(\frac{A}{W}\right)^{5/2} - 38.48\left(\frac{A}{W}\right)^{7/2} + 5.385\left(\frac{A}{W}\right)^{9/2}$$

$K_{Ic}$  is plane-strain fracture toughness in  $\text{psi}\sqrt{\text{in}}$

P is load, in lbs.

B is thickness, 0.250-inch

W is width, 0.750-inch

A is crack length, in inches

When  $\frac{P_{max}}{P_Q} > 1.1$  or  $B < 2.5 \frac{K_{Ic}^2}{\sigma_{ys}}$ ,  $K_{Ic}$  was not valid and  $K_Q$  was substituted for  $K_{Ic}$ .

Stress-corrosion specimens were precracked on the same machine and with the same basic procedure as the fracture-toughness test specimens, with one exception. The notch was submerged in 3.5 percent salt water in a plastic box attached to the specimens during precracking and until the completion of stress-corrosion test, as shown in Figures 17A and 17B. The specimen was loaded using a dead-weight lever-arm loading frame. Weight equivalent to  $1.0 \text{ ksi}\sqrt{\text{in}}$  was added every three hours, minimum, until crack growth initiated and/or the specimen failed. The threshold stress-intensity factor for stress-corrosion,  $K_{Isc}$ , was calculated using the same equation:  $K = \frac{P}{BW^{3/2}} F\left(\frac{A}{W}\right)$

Here, P is the load at failure and A is the crack length before adding the final increment of load.

At least three tests were conducted for each condition.

## IV RESULTS AND DISCUSSION

### HEAT-AFFECTED ZONE STUDIES

#### Continuous Cooling Transformation

Figure 18 shows the continuous cooling transformation diagram (CCT) determined for Ti-662 from 2500F, based upon six cooling rates. Mechanical properties and microstructure studies were conducted for specimens cooled at 336F, 110F, and 25F/sec.

The  $\beta \rightarrow \alpha$  transformation temperature decreased with increasing cooling rate (1500F at 25F/sec and 1230F at 366F/sec). It was expected that the nucleation and growth process would be suppressed by increasing cooling rate. For the same reason, the  $\alpha$ -platelets were narrower and shorter at higher cooling rates, as shown in the microstructures of Figures 19 through 21. The CCT diagrams further shows that the martensitic transformation temperature ( $M_s$ ) has not been affected by cooling rate, as found in Ti-Mo alloys by Duwez<sup>(7)</sup>, because the transformation of  $\beta \rightarrow \alpha'$  is a shear process. This  $M_s$  temperature is approximately 1040F.

On cooling,  $\beta$  phase became unstable at the  $\alpha/\beta$  transformation temperature and  $\alpha$  phase precipitated by rejecting  $\beta$ -stabilizers. As the  $\alpha$  phase grew, the  $\beta$  phase became enriched in  $\beta$ -stabilizers. At the  $M_s$  temperature, lean  $\beta$  phase transformed to  $\alpha'$  by shear, and enriched  $\beta$  phase, which has a lower  $M_s$  temperature, remained as retained  $\beta$ .

At slow cooling rates, the time for nucleation and growth of  $\alpha$  phase is longer and the size of  $\alpha$ -platelets is larger. On the other hand, less  $\beta$  phase is lean enough in  $\beta$ -stabilizer to transform into  $\alpha'$ . When the cooling rate is high, there is less time for nucleation and growth of  $\alpha$  phase and the size of  $\alpha$ -platelets is small. Since less  $\alpha$  phase transforms from  $\beta$ , the  $\beta$  phase is more diluted in  $\beta$ -stabilizers. Thus, more  $\alpha'$  is transformed below the  $M_s$  temperature.

### Effect of Cooling Rate on Microstructure and Mechanical Properties

Figures 22 and 23 indicate the effect of cooling rate on phase contents in the synthetic HAZ. In the as-cycled condition, the phases present were 60%  $\alpha$ , 30%  $\alpha'$ , and 10%  $\beta$  in a specimen cooled from 2500F at 366F/sec. The  $\alpha$  phase increased to 68% and  $\alpha'$  phase decreased to 27% at 110F/sec. At 25F/sec, the  $\alpha$  phase increased to 81% and  $\alpha'$  phase decreased to 10%. However, cooling rate was less influential on the  $\beta$  content, which remained between 5% and 10%. Table IV summarizes phase contents in the synthetic HAZ in various heat treatment conditions.

Microstructure has a definite influence on the mechanical properties. Hardness measurements were the least sensitive measure of microstructural changes. Yet, they show the general trend of higher hardnesses at cooling rates and increased hardness as a result of the 500F thermal exposure for 1000 hours, as shown in Table V.

TABLE IV  
SUMMARY OF PHASE CONTENTS IN THE SYNTHETIC  
HEAT-AFFECTED ZONE IN VARIOUS HEAT TREATMENT CONDITIONS

COOLING RATE (F/SEC)	HEAT TREATMENT	$\alpha$	$\alpha'$	$\beta$ (%)
366	As-Cycled	60	30	10
366	Cycled plus 1400F - 4 hrs.	74	16	10
366	Cycled plus 1600F - 2 hrs.	74	15	11
366	Cycled plus 1400F - 4 hrs. & 500F - 1000 hrs.	75	13	12
110	As-Cycled	68	27	5
110	Cycled plus 1400F - 4 hrs.	76	27	7
110	Cycled plus 1600F - 2 hrs.	77	17	7
110	Cycled plus 1400F - 4 hrs. & 500F - 1000 hrs.	80	10	10
25	As-Cycled	81	10	9
25	Cycled plus 1400F - 4 hrs.	85	4	11
25	Cycled plus 1600F - 2 hrs.	86	3	11
25	Cycled plus 1400F - 4 hrs. & 500F - 1000 hrs.	86	2	12

**TABLE V**  
**HARDNESS MEASUREMENT IN**  
**THE SYNTHETIC HEAT-AFFECTED ZONE**

CONDITIONS	HARDNESS, ROCKWELL C					
	366F/SEC	260F/SEC	170F/SEC	110F/SEC	64F/SEC	25F/SEC
As-Cycled	45	42	39	41	39	36
Cycled plus 1400F - 4 hrs.	37	--	--	36	--	34
Cycled plus 1600F - 2 hrs.	33	--	--	35	--	34
Cycled, 1400F - 4 hrs. plus 500F - 1000 hrs.	38	--	--	39	--	38

Table VI summarizes the fracture toughness ( $K_{Ic}$ ) and threshold stress-intensity factor for stress corrosion ( $K_{Isc}$ ) of the synthetic HAZ in various conditions. From this Table, curves were plotted to show the relationship between heat treatments,  $K_{Ic}$ , and  $K_{Isc}$ .

**TABLE VI**  
**SUMMARY OF  $K_{Ic}$  AND  $K_{Isc}$  OF THE SYNTHETIC**  
**HEAT-AFFECTED ZONE IN VARIOUS HEAT TREATMENT CONDITIONS**

COOLING RATE**	HEAT TREATMENT	$K_{Ic}$	$K_{Isc}$	$K_{Isc}/K_{Ic}$
366	As-Cycled	34	32	0.94
366	Cycled plus 1400F - 4 hrs.	46	37	0.80
366	Cycled plus 1600F - 2 hrs.	61*	37	0.61
366	Cycled plus 1400F - 4 hrs. & 500F - 1000 hrs.	48	26	0.54
110	As-Cycled	46	40	0.87
110	Cycled plus 1400F - 4 hrs.	51	28	0.55
110	Cycled plus 1600F - 2 hrs.	64*	40	0.62
110	Cycled plus 1400F - 4 hrs. & 500F - 1000 hrs.	53	27	0.51
25	As-Cycled	60	38	0.63
25	Cycled plus 1400F - 4 hrs.	63*	38	0.60
25	Cycled plus 1600F - 2 hrs.	66*	41	0.62
25	Cycled plus 1400F - 4 hrs. & 500F - 1000 hrs.	60	27	0.45

\*  $K_Q$

\*\* Cooled from 2500F



Figures 24 and 25 show the effect of cooling rate on fracture toughness and stress-corrosion resistance in four conditions. Considering the as-cycled condition only, Figure 24 indicates that the cooling rate had a large influence on the fracture toughness. Increasing the cooling rate from 25F/sec to 366F/sec decreased  $K_{IC}$  from 60  $\text{ksi}\sqrt{\text{in}}$  to 34  $\text{ksi}\sqrt{\text{in}}$ . The stress-corrosion resistance, Figure 25, only decreased from 38  $\text{ksi}\sqrt{\text{in}}$  to 32  $\text{ksi}\sqrt{\text{in}}$  due to the same change in cooling rates.

From the CCT diagram, one could predict that the transformation products resulting from various cooling rates affect the mechanical properties. Figure 26 shows that  $K_{IC}$  is decreased with increasing amounts of  $\alpha'$  and decreasing amounts of  $\alpha$ , but is not related to the amount of  $\beta$ . The decreased fracture toughness from increasing volume fractions of metastable phases ( $\alpha'$  in this case) was discussed by Curtis and Spurr<sup>(8)</sup>. The morphology of  $\alpha$ -platelets also affects toughness. Thinner  $\alpha$ -platelets produced by higher cooling rates decrease toughness. It is believed that the combined effects of increasing  $\alpha'$  and decreasing  $\alpha$ -platelet size are responsible for decreased toughness in a weldment. Both the amount of  $\alpha'$  and the  $\alpha$ -platelet size are uniquely related to cooling rate.

Figure 27 is a plot of the effect of phase contents on stress-corrosion resistance. Stress-corrosion resistance of the as-cycled and heat-treated specimens (solid line) showed minor differences as a function of  $\alpha'$  content. The thermal exposure reduced stress-corrosion resistance significantly (13  $\text{ksi}\sqrt{\text{in}}$ ), but this reduction was essentially independent of  $\alpha'$  content. These observations were consistent with the effect of cooling rate on stress-corrosion resistance shown in Figure 25. It was suspected that the reduction of stress-corrosion resistance by thermal exposure was caused by the precipitation of fine particles in the  $\alpha$  phase.

Fracture toughness of the heat-affected zones varied considerably, depending upon welding parameters and postweld treatments. Therefore, stress-corrosion behavior was also examined in terms of the ratio of  $K_{Isc}/K_{IC}$  to normalize differences in toughness. The effects of cooling rates and phase contents on the stress-corrosion susceptibility ratio ( $K_{Isc}/K_{IC}$ ) are plotted in Figures 28 and 29, respectively. It is important to realize that an

increase in the  $K_{Isc}/K_{Ic}$  ratio reflects a decrease in the stress-corrosion susceptibility of a material. In the as-cycled condition then, increasing cooling rates decrease stress-corrosion susceptibility appreciably (Figure 28). However, stress-corrosion susceptibility was less dependent upon cooling rate when postweld heat-treatment was employed. Figure 29 shows a strong trend of decreasing stress-corrosion susceptibility (increasing  $K_{Isc}/K_{Ic}$  ratio) with increasing amounts of  $\alpha'$ . At approximately 30%  $\alpha'$ ,  $K_{Isc}/K_{Ic}$  was essentially equal to one, indicating immunity to stress corrosion. However, it must be appreciated that  $K_{Ic}$  and  $K_{Isc}$  decreased with increasing amounts of  $\alpha'$  even though the ratio of  $K_{Isc}/K_{Ic}$  increased.

The above findings are supported by the fractographic evidence shown in Figures 30 through 33. Figure 30 shows the fracture surface of a synthetic HAZ specimen cooled from 2500F at 366F/sec and fracture-toughness tested. This specimen contained 30%  $\alpha'$  and exhibited the lowest toughness (34 ksi $\sqrt{in}$ ). In comparison, the specimen shown in Figure 31 was cooled at 25F/sec and heat-treated at 1600F for 2 hours to provide a  $K_{Ic}$  of 66 ksi $\sqrt{in}$ . The fracture mode for both specimens was dimple overload, although differences in dimple size and depth were evident, as expected. Figure 32 shows the fracture surface of a synthetic HAZ specimen cooled from 2500F at 366F/sec and stress-corrosion tested. A  $K_{Isc}$  value of approximately 32 ksi $\sqrt{in}$  (0.94  $K_{Ic}$ ) was required to produce the fracture. The fracture mode is essentially the same overload mode as obtained by fracture-toughness testing, thus indicating the essential immunity of this microstructure to stress corrosion. In contrast, specimens cooled at 25F/sec and heat treated at 1600F for 2 hours exhibited a quasi-cleavage fracture mode after stress-corrosion testing (Figure 33). This treatment produces microstructures with the lowest  $\alpha'$  content examined. The stress-corrosion immunity of microstructures containing substantial amounts of  $\alpha'$  has also been noted in Ti-6Al-4V and Ti-8Al-1Mo-1V alloys by Fager and Spurr<sup>(9)</sup>.

## Effect of Heat-Treatment and Thermal Exposure on Synthetic HAZ Microstructure and Mechanical Properties

Welding processes which produce a high heat-input also produce a HAZ of high toughness and stress-corrosion resistance. From a metallurgical point-of-view, such welding processes are ideal for joining Ti-6Al-6V-2Sn. Unfortunately, high heat-input processes produce wide and shallow fusion zones and low heat-input processes produce narrow and deep fusion zones, which are preferred for aircraft application because of fit-up, joint design, distortion, and economical considerations. In these cases, low toughness and stress-corrosion resistance are expected in the HAZ. To improve the mechanical properties, postweld heat-treatment must be performed. In this investigation, two heat-treatment conditions were employed: 1400F for 4 hours and 1600F for 2 hours, followed by air cooling in both cases.

Figures 34, 35, and 36 show the microstructure of specimens which experienced cooling rates from 2500F at 366F/sec, 100F/sec, and 25F/sec, respectively, followed by heat treat at 1400F for 4 hours. This heat-treatment coarsened  $\alpha$ -platelets and promoted some decomposition of  $\alpha'$  to  $\alpha + \beta$ . A heat-treatment of 1600F for 2 hours promoted further coarsening of  $\alpha$ -platelets and decomposition of  $\alpha'$  to  $\alpha + \beta$  (Figures 37, 38, and 39). Even at 500F, the decomposition of  $\alpha'$  to  $\alpha + \beta$  was still in progress, although at a slow rate (Figure 22). The net increase in  $\beta$  after 1000 hours was about 2%. This thermal exposure delineated  $\alpha$ -platelets from the  $\beta$ -phase background, as shown in Figures 40, 41, and 42. The effect of heat-treatments on phase content was previously summarized in Figures 22 and 23.

As a result of the changes in phase contents by heat-treatment, the  $K_{Ic}$  and  $K_{Isc}$  values were affected. In Figure 24, heat-treatment not only increased the fracture toughness but also reduced the differences in fracture toughness caused by differences in cooling rates. The thermal exposure at 500F for 1000 hours did not affect fracture toughness significantly.

The effect of heat-treatment on the stress-corrosion susceptibility was shown in Figure 28. Heat treatment increased stress-corrosion susceptibility (lower  $K_{Isc}/K_{Ic}$  ratio) by greater amounts at high cooling rates than at low cooling rates. The heat-treatment at 1600F for 2 hours increased the stress-corrosion susceptibility more than heat-treatment at 1400F for 4 hours and also eliminated the cooling-rate effect. An exposure at 500F for 1000 hours increased the stress-corrosion susceptibility even further. The effect of heat treatment on the stress-corrosion susceptibility is again attributed to the phase transformation products and microstructural morphology. If one compares Figures 22 and 23 to Figure 28, the curves in Figures 22 and 23 are similar but inverted from Figure 28. Figure 29 includes data points obtained from all conditions. It is clearly shown that the stress-corrosion susceptibility is related to the microstructural morphology, particularly  $\alpha'$  and, probably, fine  $\alpha$  precipitates.

#### FUSION ZONE STUDIES

##### Correlation Between Heat-Input and Cooling Rate

One of the important parameters of welding processes is the heat-input, in terms of Joules per inch. Therefore, the selection of the welding processes should consider not only the economics and practicality of the process, but also the metallurgical effects related to the different heat-inputs of the welding processes.

The heat-inputs and cooling rates for the four welding processes are listed in Table VII.

TABLE VII  
HEAT-INPUT AND COOLING RATE OF FOUR WELDING PROCESSES

	MANUAL* GTAW	PLASMA ARC	AUTOMATIC* GTAW	ELECTRON BEAM
Heat-Input (Kilo-Joules/inch)	78	54	26	7
Cooling Rate (F/sec)	25	64	110	1,000

\*Welded from both sides

The corresponding cooling rate for each process on the CCT diagram is shown in Figure 18. The hatched lines indicate the probable variations in cooling rates caused by typical variations of welding parameters, material thickness, and back-up material. It should be noted that the microstructure and mechanical properties in the fusion zone may not be the same as that of the HAZ near the fusion line because of melting and solidification during welding.

#### Solidification Pattern in the Fusion Zones

Metallurgically, fusion welding is analogous to a casting. The welding heat melts the base metal to form a pool of liquid that solidifies continuously in a mold formed by the base metal. The solidification structure in the "cast" fusion zone varies with the chemical gradient (chemical composition), the temperature gradient (diffusivity, thickness, travel speed, and heat-input), and the grain size of the "mold."

Figure 43 shows the surface solidification pattern of a manual GTA weld bead. The arced lines outline the shape of the molten pool where the growth of grains was momentarily stopped due to the manipulation of welding. The grain direction indicates the direction of temperature gradient during solidification. The photomacrograph in Figure 44 shows long columnar grains grown from the bottom of the double Vee-groove. Because of slow travel speed (about 2 in/min), the grain size in the overlapping area is fairly large. The hardness traverse, Rc 35 average, indicates that a slow cooling rate gives a relatively low hardness in the FZ as well as the HAZ.

Photomicrographs in three directions of the manual GTAW are shown in Figure 45. These three views show the columnar grain growth in the weld bead. The top-view plane intersects vertical grains and shows some equiaxed and some elongated grains in the direction of welding. The longitudinal view shows large, elongated grains containing feather-like  $\alpha$ -platelets in this plane. Grains in the transverse plan grow vertically.

The fusion zone pattern produced by plasma arc welding is shown in Figure 46. Since it is welded automatically, ripples are not visible. A photomacrostructure of the same weld is shown in Figure 47. The horizontally-oriented grains indicate that heat flow at the bottom of the joint is toward the base metal. At the upper part of the fusion zone, grains grow vertically because the shortest path to dissipate heat is through the bottom of the weld to the back-up bar. A 64F/sec cooling rate raises the hardness in the HAZ to Rc40. The photomicrographs in Figure 48 show some directionality caused by increased welding speed (6 IPM).

Figure 49 is a photomacrograph of a weld bead produced by the automatic GTA welding process. Some elongated grains in the direction of welding are visible in the center of the bead and equiaxed grains are seen near the HAZ. This indicates that the temperature gradient was higher in the direction of welding than in the transverse direction in the center of the bead. In the areas near the HAZ, the temperature gradients are almost equal in both directions. The wave-shaped lines are the outline of the molten pool due to a non-uniform advancing speed during welding. In the vertical plane, Figure 50, heat flows vertically down to the groove, as shown by the vertically oriented grains. Due to the relatively high cooling rate (110F/sec), hardness in the FZ, as well as HAZ, is increased.

Figure 51 shows the microstructure in three directions of a fusion zone welded by the automatic GTAW process. The grain growth direction is similar to that in the plasma arc welded fusion zone.

The high welding speed, 40 in/min, of the electron-beam welding process produced the extremely elongated solidification pattern shown in Figure 52. The high depth-to-width ratio of the weld bead resulted in lateral heat flow and grain growth in the same direction, Figure 53. Near the top of the bead, the heat flow is three-dimensional, which is revealed by the direction of grain growth due to the difference in solidification patterns between top and bottom portions of the weld. The brief heating and cooling cycle caused less solution of alloying elements on heating and hardening on cooling, thus shifting the high-hardness area into the FZ. The peak hardness in the EB weld is the highest among the welds produced by the four welding processes.

The extremely high cooling rate obtained by electron beam welding prevents the migration of alloying elements. Grain boundaries are not clearly delineated, and subgrain structures are visible in Figure 54. Because of the temperature gradient in the fusion zone, equiaxed grains are formed as shown in the longitudinal view.

#### MICROSTRUCTURE AND MECHANICAL PROPERTIES OF THE FUSION ZONES

Figures 55 through 58 show the microstructures in the fusion zones produced by the four welding processes. It is obvious that the fineness of the  $\alpha$  -platelets is related to the cooling rate associated with each welding process. More feather-like  $\alpha$  is observed in the manual GTA weld, Figure 55, than welds by any other welding process. On the other hand, the  $\alpha$  needles in the electron-beam fusion zone are so fine that they are hardly resolved, Figure 58. The needle size in Figures 56 and 57 is between these two extremes.

From the CCT diagram, Figure 18, once again we can predict that the fusion zones contain different amounts of phases due to differences in cooling rates. The results from X-ray diffraction measurements of the  $\alpha$ ,  $\alpha'$ , and  $\beta$  contents are shown in Table VIII. As expected, the phase contents are entirely related to the cooling rate, as shown in Figure 59. The cooling rate in the HAZ of the electron beam welds was greater than 1000F/sec. Therefore, dotted lines are used.

The room-temperature tensile test data are shown in Table IX. The longitudinal tensile specimens exhibited strengths which averaged the strengths of the base metal, HAZ, and FZ. The tensile strengths, as well as yield strengths obtained from the longitudinal specimens are about the same within a variation of 1.5%. Elongation data show a weak trend of lower elongation with increasing cooling rate, except for the electron beam welds. This was due to the fact that the gage section of the EB-welded tensile specimens contained more base metal than the specimens produced with the other welding processes. Figure 60 shows the graphic relationship between longitudinal tensile yield and elongation of fusion zones produced by various welding processes and heat treatments. The electron beam welds are out of place for the reason explained above.

TABLE VIII  
SUMMARY OF PHASE CONTENTS IN THE FUSION ZONES

WELDING PROCESS	COOLING RATE (F/SEC)	HEAT TREATMENT	$\alpha$	$\alpha'$	$\beta$ (%)
Base Metal		MA	93	0	7
Base Metal		STA	94	0	6
Manual GTAW	25	As-Welded	79	10	11
PAW	64	As-Welded	78	12	10
Automatic GTAW, Matching Filler	110	As-Welded	75	16	9
Automatic GTAW, 50% Ti-662 50T Ti-75A Filler	110	As-Welded	84	6	10
Automatic GTAW, 100% Ti-75A Filler	110	As-Welded	88	4	8
Automatic GTAW, Matching Filler	110	1400F-4 hrs	86	3	11
Automatic GTAW, Matching Filler	110	1400F-4 hrs 500F-1000 hrs	88	2	10
Electron Beam Welding	>1000	As-Welded	20	78	2



TABLE IX  
TENSILE PROPERTIES OF WELDED Ti-6Al-6V-2Sn PLATE AS-WELDED

PROCESS		<u>.2% YIELD</u> KSI	<u>ULT. STGTH.</u> KSI	ELONG %(2")	<u>MODULUS</u> 10 <sup>6</sup> PSI	FAILURE LOCATION
Manual GTAW	L	153.3	171.8	4.0	15.3	—
	T	154.6	167.5	4.7	16.3	FZ
PAW	L	155.7	173.2	3.7	15.0	—
	T	162.3	175.8	9.7	16.2	BM
Automatic GTAW	L	157.6	175.2	3.5	15.3	—
	T	163.8	174.8	8.0	17.0	BM
EBW	L	155.9	172.6	5.2	15.1	—
	T	163.3	173.0	13.5	17.3	BM

NOTE: L Longitudinal Tension  
T Transverse Tension  
BM Base Metal  
FZ Fusion Zone

In the transverse tensile tests, failure took place in the weakest zone. With the exception of manual GTAW, failure occurred in the base metal instead of the fusion zone. This occurred because the  $\alpha'$  and fine  $\alpha$ -platelets produced at higher cooling rates strengthened the fusion zones and part of the heat-affected zones. Although the manual GTAW produced more  $\alpha'$  in the fusion zone than in the base metal, failure took place in the fusion zone because of the extremely large columnar structure. Because failure took place in the base metal in the welds produced by the other three welding processes, the tensile yield strengths were essentially identical as shown in Table IX. However, the elongation in the electron beam welds was extremely high (13.5%) in comparison to the other welds (8%-9.7%). This was apparently caused by the relative width of the fusion zone to the base metal within the gage length which was the smallest for the electron beam weld.

A plot of  $F_{ty}$  vs  $K_{Ic}$ , Figure 61, indicates four effects: (1) decreases in cooling rates from the various welding process increases  $K_{Ic}$  and decreases  $F_{tu}$ , (2) addition of Ti-75A filler decreases  $F_{ty}$  and increases  $K_{Ic}$ , (3) post-weld heat-treatment at 1400F for 4 hours decreases  $F_{ty}$  and increases  $K_{Ic}$ , and (4) dual filler-metal welding provided the best combination of toughness and yield strength. The location of the data point for the EB fusion zone appears out of place relative to  $F_{ty}$  in the  $F_{ty}$  vs  $K_{Ic}$  plot of the electron beam for the reason discussed above.

The results of the four-point, reverse-bending fatigue tests for longitudinal welds are shown in Figure 62. The data scattering is attributed to the inhomogeneity of microstructure in the as-welded test specimens in the fusion zone. However, the data generally indicate that the welds with higher tensile strength exhibit higher fatigue strength. Fatigue cracks all initiated in the fusion zone, as shown in Figure 63.

The fracture-toughness and stress-corrosion data for the fusion zones are summarized in Table X. Fracture toughness was affected by  $\alpha'$  content as observed in the HAZ studies and, therefore, was a function of cooling rate, as shown in Figure 64. The effects of phase contents on the fracture-toughness and stress-corrosion resistance are shown in Figures 65 and 66, respectively. From these two plots, one recognizes the  $\alpha'$  again plays an important role on the  $K_{Ic}$  and  $K_{Isc}$ . Table X also shows that stress-corrosion susceptibility (based upon  $K_{Isc}/K_{Ic}$ ) decreased with increasing amounts of  $\alpha'$  as observed during the HAZ studies.

The fractographic structures from fracture-toughness tests on a manual GTA-welded fusion zone (slowest cooling rate) and electron beam welded fusion zone (fastest cooling rate) are shown in Figures 67 and 68, respectively. Both indicate dimple, overload fracture modes, although the dimple sizes vary.

Figures 69 and 70 are the stress-corrosion fracture surfaces of the manual GTA-welded and electron beam welded fusion zones. The fracture mode of the manual GTA weld is predominantly quasi-cleavage, typical of a stress-corrosion failure. The fracture mode of the electron beam weld is predominantly dimple overload, evidence of high resistance to stress-corrosion imparted by the high content of  $\alpha'$ . The change of fracture modes between fast and slow-cooled fusion-zone specimens is the same as observed in the heat-affected zone studies. In Table X, the stress-corrosion susceptibility ( $K_{Isc}/K_{Ic}$ ) approaches unity for electron beam welds.

TABLE X  
SUMMARY OF  $K_{Ic}$  and  $K_{Isc}$  OF THE FUSION ZONES

WELDING PROCESS	RECORDED AND ESTIMATED COOLING RATE (F/SEC)**	HEAT TREATMENT	$K_{Ic}$ (KSI $\sqrt{IN}$ )	$K_{Isc}$ (KSI $\sqrt{IN}$ )	$K_{Isc}/K_{Ic}$
Base Metal		Mill Annealed	44*	35	.79
Base Metal		STA	24	21	.88
Manual GTAW	25	As-Welded	50*	42	.84
PAW	64	As-Welded	48	40	.83
Automatic GTAW, Matching Filler	110	As-Welded	44	37	.84
Automatic GTAW, 50% Ti-662, 50% Ti-75A Filler	110	As-Welded	62*	51	.82
Automatic GTAW, 100% Ti-75A Filler	110	As-Welded	68*	73	1.07
Automatic GTAW, Matching Filler	110	1400F-4 hrs	57*	36	.63
Automatic GTAW, Matching Filler	110	1400F-4 hrs 500F-1000 hrs	54	26	.48
EBW	> 1000	As-Welded	34	31	.91

\*  $K_Q$

\*\* Measured in the HAZ, 2500F peak

### Effect of Composition Alteration on Fusion-Zone Microstructure and Mechanical Properties

By varying wire-feed rates of two dissimilar filler metals using the GTAW process, one can tailor fusion-zone mechanical properties for specific applications. The addition of Ti-75A filler metal has been shown to increase notch toughness in a Ti-662 weld<sup>(10)</sup>. This portion of the program studied the effect of additions of Ti-75A filler-metal along with Ti-662 filler in two ratios on the microstructure, mechanical properties, and alloy distribution in the fusion zone. It should be noted that the degree of base-metal dilution is not only affected by the ratio of filler metal, but also the geometry of the weld joint. Therefore, the effect of Ti-75A filler additions on the microstructure and mechanical properties applies rigorously only for the joint geometry described in Figure 7.

Figures 71 and 72 show the macrostructure and transverse hardness measurements in the fusion zone using 50% Ti-662/50% Ti-75A filler metals, and 100% Ti-75A filler metal, respectively. Since the automatic GTAW process was used, the columnar structure should be the same as that produced with single, matching filler metal, Figure 50. The grain size and hardness of these two welds do not have noticeable differences.

Figures 73 and 74 illustrate the microstructure in the fusion zone using 50% Ti-662/50% Ti-75A and 100% Ti-75A filler metal, respectively. The 50/50 fusion zone exhibits finer  $\alpha$  needles than the 100% Ti-75A fusion zone in Figure 72 and exhibits the same morphology as the 100% Ti-662 GTA-welded fusion zone of Figure 57. The phase contents determined by X-ray diffraction in the dual filler-metal welded fusion zone are listed in Table VIII. By adding Ti-75A filler metal, the level of  $\beta$ -stabilizers in the fusion zone was reduced. Thus, the  $\beta$  to  $\alpha$  transformation temperature was increased in the equilibrium condition as well as in the continuous cooling condition. As a result of this change of transformation temperature, the  $\alpha'$  and  $\beta$  phases were reduced according to the amount of Ti-75A filler added, as shown in Table VIII.

Figure 75 shows the microprobe measurements in the fusion zones deposited with 100% Ti-662, 50% Ti-662/50% Ti-75A, and 100% Ti-75A filler metal, respectively. The weld deposited with 100% Ti-662 was used as a baseline. As

expected, the three alloying elements are uniformly distributed near the nominal composition in the plate-thickness direction.

In the width direction of the 50/50 fusion zone, the aluminum content varied within the 6%-7% range. Vanadium was nearly 6% throughout the width of the weld, and tin varied from approximately 1.5% to 2%, with the low point near the center. In the thickness direction (solid line), vanadium varied from 4% at the top to 6.3% at the center of the weld; aluminum and tin were nearly unchanged throughout the thickness of the weld.

When only Ti-75A filler-metal was deposited, aluminum was again fairly uniformly distributed in both directions. Vanadium content increased from 2.5% at the top of the weld bead to 4% at the center in the plate thickness direction (solid lines) and decreased from 6% at the edge of the fusion zone to 3.2% at the center of the weld in the plate-width direction (dotted lines). Sn varied within 2% to 3% from the edge of the weld to its center. These chemical gradients were dependent upon the amount of filler-metal dilution and the mobility of the alloying elements.

Longitudinal tensile data are listed in Table XI.

TABLE XI  
TENSILE PROPERTIES OF Ti-6Al-6V-2Sn FUSION ZONE ADDING Ti-75A FILLER  
METAL, AS-WELDED (LONGITUDINAL TENSION ONLY)

RATIO		.2% YIELD STGTH	ULT. STGTH	ELONG. (2")%	MODULUS
Ti-662	Ti-75A	KSI	KSI		10 <sup>6</sup> PSI
100	0	157.6	175.2	3.5	15.3
50	50	155.5	172.4	3.8	15.2
0	100	146.3	167.7	4.3	15.3

The addition of Ti-75A filler-metal reduces tensile as well as yield strengths and increases elongation to a small but consistent amount.

S-N curves for reverse-bending fatigue of fusion zones produced by automatic GTA welding with and without Ti-75A filler-metal are shown in Figure 76. The fusion zone deposited with 100% Ti-75A which exhibited the lowest tensile strength also exhibited the lowest fatigue strength. This is consistent with the results obtained from the fatigue tests of fusion zones produced by various welding processes.

Fracture toughness decreases with increasing  $\alpha'$ , as noted in the previous sections. It was expected that the fusion zone deposited with 100% Ti-75A should have the highest  $K_{Ic}$  ( $68 \text{ ksi}\sqrt{\text{in}}$ ) value and that deposited with 100% Ti-662, the lowest ( $44 \text{ ksi}\sqrt{\text{in}}$ ). The results in Table X and Figure 77 are as expected. It should be noted that the addition of Ti-75A increased stress-corrosion resistance more than fracture toughness. The  $K_{Isc}$  of  $73 \text{ ksi}\sqrt{\text{in}}$  and the  $K_{Ic}$  of  $68 \text{ ksi}\sqrt{\text{in}}$  were considered equal within the range of data scattering. The relationship between  $K_{Isc}$  and  $K_{Ic}$  can be related to the phase contents in the fusion zone as listed in Table VIII.

#### Effect of Postweld Heat-Treatment on Fusion-Zone Microstructure and Mechanical Properties

The postweld heat-treatment used for the fusion-zone tests was 1400F for 4 hours in a vacuum furnace. This heat treatment was also one of those used for the synthetic HAZ tests. Higher temperatures will produce a microstructure which provides better toughness and ductility based upon the HAZ studies and the studies of Simpson and Wu<sup>(4)</sup>.

The macrostructure and hardness measurements in the fusion zone after heat-treatment at 1400F for 4 hours are shown in Figure 78. The hardness in the fusion zone is about 3 Rockwell C points lower than the hardness in the as-welded condition shown in Figure 50 as a result of this heat-treatment.

The microstructure of the fusion zone at 500X is shown in Figure 79. The  $\alpha$  platelets in the grains grew larger and continuous  $\alpha$  precipitates appear in the grain boundaries (compare to Figure 57). The microstructure in this Figure is identical with the microstructure in the HAZ cooled at 110F/sec and heat treated at 1400F for 4 hours, Figure 35.

When  $\alpha$  was growing during this heat-treatment, the reaction of  $\alpha'$  to  $\alpha + \beta$  was taking place. As a result of this reaction,  $\alpha$  content after heat-treatment is increased from 75% to 86%,  $\beta$  content from 9% to 11%, and  $\alpha'$  content is reduced from 16% to 3%, Table VIII. Because of the change of microstructure, morphology, and phase contents, the mechanical properties were affected accordingly.

A postweld heat-treatment of 1400F for 4 hours was expected to reduce tensile and yield strengths and increase elongation in the fusion zone. Table XII lists the tensile test results. Comparison with the as-welded, longitudinal tensile properties (Table IX) produced by automatic GTAW demonstrates this effect.

TABLE XII  
TENSILE PROPERTIES OF THE FUSION ZONE, AUTOMATIC GTAW,  
POSTWELD HEAT TREATED AT 1400F FOR 4 HOURS

.2% YIELD STGTH	ULT. STGTH	ELONG.	MODULUS	FAILURE
KSI	KSI	(2")%	10 <sup>6</sup> PSI	LOCATION
L 147.4	158.9	11.8	16.4	- -
T 155.6	164.8	9.0	17.5	FZ

L - Longitudinal Tension

T - Transverse Tension

FZ- Fusion Zone

Average of three tests

The transverse tensile tests showed the failure location to be in the fusion zone instead of in the base metal as in the as-welded condition. The narrow fusion zone (about 0.5-inch), as compared to the 2-inch gage length, limited the elongation to 9%. This heat-treatment produced about the same tensile strength as adding 100% Ti-75A filler-metal, but lower strength than the slow cooling rate obtained from manual GTAW.

Reverse-bending fatigue behavior for postweld heat-treated automatic GTAW fusion zones is shown in Figure 80. The fatigue strength of heat-treated welds is 5000 psi lower than that of the as-welded condition. This is also consistent with the results obtained in the previous sections which show that fatigue strength is dependent upon tensile strength.

The postweld heat-treatment reduced the amount of  $\alpha'$  in the fusion zone and this reduction increased fracture toughness from 44 ksi $\sqrt{\text{in}}$  in the as-welded condition to 57 ksi $\sqrt{\text{in}}$ . The increase in fracture toughness by postweld heat-treatment (13 ksi $\sqrt{\text{in}}$ ) was not as much as obtained by the addition of Ti-75A filler metal which produced an increase of 24 ksi $\sqrt{\text{in}}$ . However, the stress-corrosion resistance remained about the same (36 ksi $\sqrt{\text{in}}$ ) as observed for the as-welded condition (37 ksi $\sqrt{\text{in}}$ ).

The FZ studies show that the effects of postweld heat-treatment on fracture toughness and stress-corrosion resistance were similar to the effects observed in the HAZ studies.

#### Effect of Thermal Exposure on Fusion Zone Microstructure and Mechanical Properties

The GTA welded fusion zone postweld heat-treated at 1400F for 4 hours and thermally exposed at 500F for 1000 hours did not show significant changes in microstructure based upon optical metallography. The macrostructure of the fusion zone and hardness traverse measurements are shown in Figure 81. The thermal exposure increased the hardness about 3 Rockwell C points (from an average of 36  $R_C$  to an average of 39  $R_C$ ). The microstructure of the fusion zone is shown in Figure 82. The fine  $\alpha$  particles in the background indicated that, during the 500F exposure, decomposition of  $\alpha'$  to  $\alpha + \beta$  was taking place, but at a slow rate. At the same time,  $\beta$  transformed to  $\alpha$ . As a result of the two reactions,  $\alpha$  increased to 88% from 86% after the heat-treatment at 1400F for 4 hours;  $\alpha'$  decreased from 3% to 2%; and  $\beta$  decreased to 1% (Table VIII). The precipitation had a significant effect as revealed in the HAZ studies on the mechanical properties, especially on stress-corrosion resistance.

The 500F - 1000 hour thermal exposure increased tensile strength slightly and decreased elongation. For convenience, the tensile properties in the fusion zones in the as-welded and heat-treated conditions are also listed in Table XIII.



TABLE XIII  
TENSILE PROPERTIES\* OF THE FUSION ZONE, AUTOMATIC GTAW,  
POSTWELD HEAT TREATED AT 1400F FOR 4 HOURS PLUS 500F FOR 1000 HOURS

CONDITION	.2% YIELD STGTH	ULT. STGTH	ELONG.	MODULUS
	KSI	KSI	(2")%	10 <sup>6</sup> PSI
As-Welded	157.6	175.2	3.5	15.3
1400F-4 hrs.	147.4	158.9	11.8	16.4
1400F-4 hrs., plus 500F-1000 hrs.	146.5	162.0	9.0	16.5

\*Longitudinal tensile only

The reverse-bending fatigue behavior of the fusion zone after exposure at 500F for 1000 hours is shown in Figure 80. At high stress, the fatigue life of the exposed fusion zone was slightly less than that without exposure. At low stress, the fatigue strength of the exposed fusion zone was practically the same as that without exposure. Among the as-welded and two heat-treatment conditions, the as-welded fusion zone which had the highest tensile strength also exhibited approximately 5000 psi greater fatigue strength for the heat-treated condition.

A thermal exposure at 500F for 1000 hours reduced fracture toughness slightly in the fusion zone. The fracture toughness of the fusion zone in the heat-treated condition was 57 ksi√in, Table X. After 1000 hours at 500F, it was reduced to 54 ksi√in. The fracture toughness in the synthetic HAZ experiencing a cooling rate of 25F/sec plus heat-treatment at 1400F for 4 hours also was lowered by 6 ksi√in after the treatment at 1400F for 4 hours plus 500F for 1000 hours.

However, the effect of thermal exposure on stress-corrosion resistance is rather drastic, as demonstrated in the HAZ study. Referring to Table X again, stress-corrosion resistance was reduced by 10 ksi√in. due to the 1000-hour exposure at 500F.

All the evidence disclosed in various parts of this report indicate that the mechanisms of failure in the fracture-toughness and stress-corrosion tests are entirely different. Since a detailed study of these mechanism differences was not within the scope of this program, this subject should be investigated further.

V

CONCLUSIONS

Based upon the experimental results, conclusions can be drawn as follows:

1. Correlation has been established between the heat-input of welding processes and cooling rates of heat-affected zones.
2. A continuous cooling transformation diagram can be used to predict the mechanical properties in the fusion and heat-affected zones produced by various welding processes.
3. The results of this investigation showed how Ti-6Al-6V-2Sn can be welded to achieve a fracture toughness of  $57 \text{ ksi}\sqrt{\text{in}}$  minimum with a yield strength of 147 ksi.
4. Fracture toughness in the weld can be improved by slow cooling, postweld heat-treatment at or above 1400F, or by adding pure titanium filler metal using the dual filler-metal method.
5. Alpha-prime reduces fracture toughness but is immune to stress corrosion.
6. Fatigue strengths increases with the increase of tensile strength.
7. A 1000-hour exposure at 500F decreases stress-corrosion resistance drastically.

## VI RECOMMENDATIONS

This program has successfully determined the correlation between micro-structure and mechanical properties in terms of welding processes, cooling rates, postweld heat-treatment, and thermal exposure. The continuation of this approach for other titanium alloys will enable welding engineers to understand the metallurgical reaction during welding and heat-treatment. Thereby, an appropriate welding process and heat-treatment can be selected to construct a weldment achieving these objectives. In addition, the mechanism of reduced stress-corrosion resistance in the fusion and heat-affected zones due to 500F thermal exposure was postulated as a result of the precipitation of fine particles. This postulation and a method for avoiding the effect on stress-corrosion resistance should be studied in the future.

## VII

### APPLICATION OF PROGRAM RESULTS TO PRACTICE

In this program, the metallurgical reactions occurring during welding, heat treatment, and thermal exposure were correlated with the mechanical properties of the heat-affected and fusion zones of Ti-6Al-6V-2Sn. The effects of these reactions on the microstructure and mechanical properties of a weldment is summarized in Table XIV.

It should be noted that the microstructures and mechanical properties obtained from the synthetic HAZ study were in basic agreement with those from the fusion zones experiencing the same cooling rate. The values with no underlines in Table XIV were estimated by extrapolation and interpolation from the experimentally measured relationships. The quantity of  $\alpha'$  is used to represent the metallographic results in Table XIV because  $\alpha'$  quantity is inversely proportional to the thickness of  $\alpha$ -platelets. The combination of  $\alpha'$  quantity and  $\alpha$ -platelet thickness is uniquely related to cooling rate and mechanical properties. The practical implications of this summary relative to the selection of welding processes and parameters follow.

#### AS-WELDED EFFECTS

In the as-welded conditions, increased cooling rates (and, therefore, increased amounts of  $\alpha'$ ) produced by various processes decreased  $K_{IC}$  and  $K_{ISCC}$  to levels below those for base metal. Yield strength showed a small increase with increasing cooling rate, although the values were close to those for base metal. The elongation values were low in all as-welded cases, while fatigue strength was essentially constant and slightly lower than the fatigue strength of base metal.

TABLE XIV  
SUMMARY OF THE CORRELATION OF MICROSTRUCTURE AND MECHANICAL PROPERTIES  
IN WELDMENT PRODUCED BY FOUR WELDING PROCESSES

PROCESSES			MANUAL GTAW		PAW		AUTO. GTAW		EBW		BASEMETAL
			HAZ	FZ	HAZ	FZ	HAZ	FZ	HAZ	FZ	MA
EFFECT OF COOLING RATE	As-Welded	$\alpha'$	10	10	12	12	16	16	78	78	0
		F <sub>ty</sub>	-	153	-	156	-	158	-	156	153
		Elongation	-	4.0	-	3.7	-	3.5	-	5.2	13.0
		Fat. Stgth.	-	55.0	-	55.0	-	55.0	-	55.0	60
		K <sub>Ic</sub>	60	50	48	48	48	44	34	34	44
		K <sub>Isc</sub>	38	42	40	40	26	37	31	31	35
EFFECT OF HEAT TREATMENT	1400F 4 hrs.	$\alpha'$	4	4	4	4	17	3	16	16	
		F <sub>ty</sub>	-	145	-	147	-	147	-	150	
		Elongation	-	13	-	12	-	11.8	-	11	
		Fat. Stgth.	-	40	-	40	-	40	-	40	
		K <sub>Ic</sub>	63	63	50	60	46	57	46	46	
		K <sub>Isc</sub>	38	38	37	37	40	36	35	35	
	1600F 2 hrs.	$\alpha'$	3	3	3	3	4	3	5	5	
		F <sub>ty</sub>	-	142	-	144	-	145	-	147	
		Elongation	-	15	-	13	-	13	-	12	
		Fat. Stgth.	-	40	-	40	-	40	-	40	
		K <sub>Ic</sub>	66	66	64	64	51	51	48	48	
		K <sub>Isc</sub>	41	41	40	40	28	37	36	36	
EFFECT OF CHEMICAL ALTERATION	50/50	$\alpha'$	4	4	5	5	6	6	8	8	
		F <sub>ty</sub>	-	152	-	154	155	155	-	156	
		Elongation	-	5.0	-	4.0	3.8	3.8	-	5.5	
		Fat. Stgth.	-	40	-	40	40	40	-	40	
		K <sub>Ic</sub>	60	68	48	65	48	62	34	50	
		K <sub>Isc</sub>	38	58	40	54	37	51	31	40	
	100% Ti-75A	$\alpha'$	3	3	4	4	4	4	6	6	
		F <sub>ty</sub>	-	142	-	145	-	146	-	148	
		Elongation	-	6.0	-	5.0	-	4.3	-	7.0	
		Fat. Stgth.	-	40	-	40	-	40	-	40	
		K <sub>Ic</sub>	60	70	48	68	68	68	34	53	
		K <sub>Isc</sub>	38	56	40	55	73	73	31	42	
EFFECT OF THERMAL EXPOSURE	1400F 4 hrs. plus 500F 1000 hrs.	$\alpha'$	2	2	3	3	10	2	13	13	
		F <sub>ty</sub>	-	146	-	146	-	146	-	146	
		Elongation	-	11	-	10	-	9.0	-	10	
		Fat. Stgth.	-	40	-	40	-	40	-	40	
		K <sub>Ic</sub>	60	60	55	55	54	54	42	42	
		K <sub>Isc</sub>	27	27	28	28	26	26	26	26	

Note:  $\alpha'$  in %  
F<sub>ty</sub> in ksi longitudinal  
Elongation in % longitudinal  
Fatigue strength in ksi at  $5 \times 10^6$  cycles  
K<sub>Ic</sub> in ksi  $\sqrt{\text{in}}$   
K<sub>Isc</sub> in ksi  $\sqrt{\text{in}}$   
 $\frac{10}{10}$  experimentally measured value  
 $\frac{10}{10}$  estimated value

### POSTWELD HEAT-TREATMENT EFFECTS

The postweld heat-treatments improved elongation to approach that of the base metal, lowered yield strength slightly, reduced fatigue strength to a constant level (2/3 of base-metal fatigue strength), and increased fracture toughness significantly with no major changes in stress-corrosion resistance. The 1400F heat-treatment produced a marked change in properties compared to the as-welded condition. The differences between properties obtained after the 1400F and 1600F heat-treatments were much smaller.

### EFFECTS OF CHEMICAL ALTERATION OF THE FUSION ZONE

The effects of chemical alteration of the fusion zones were similar to those produced by heat-treat with two exceptions. Elongation values were lower and toughness and stress-corrosion resistance were higher than obtained by heat-treatment alone.

The postweld heat-treatment can be replaced by using the dual filler-metal method adding commercially pure titanium filler metal to the fusion zone. Although residual stresses and the hardening of the heat-affected zone cannot be avoided, the ductile, tougher fusion zone could absorb some strain to reduce the possibility of cracking. In addition, preheat and postheat will reduce cooling rate and thereby increase toughness and ductility in the HAZ as well.

### THERMAL EXPOSURE EFFECTS

Thermal exposure at 500F for long periods of time produced a marked reduction in stress-corrosion resistance and a minor reduction in toughness and ductility, but no effect on fatigue strength. This phenomenon appeared to be related to fine precipitation in the  $\alpha$  phase during the thermal exposure.

### WELDING PROCESS SELECTION

In general, the toughness of a weldment should be higher than that of the base metal to accommodate the possibility of undetectable defects. Since toughness is so important and so sensitive to welding processes and parameters, it should weigh heavily in the selection of welding procedures for a specific application.

It should be emphasized that the material thickness used in this program necessitated two-pass welding using the manual and automatic GTA processes. The heat-input required for this two-pass GTA welding was less than that required if a single-pass weld could have been made. The heat-input for single pass, automatic GTA welding should be greater than that required for single-pass welding by the PAW and EBW processes. Thus, the cooling rates and corresponding mechanical properties obtained from the automatic GTAW were listed between PAW and EBW; whereas, single-pass automatic GTA welding would place this process between manual GTAW and PAW relative to cooling rates.

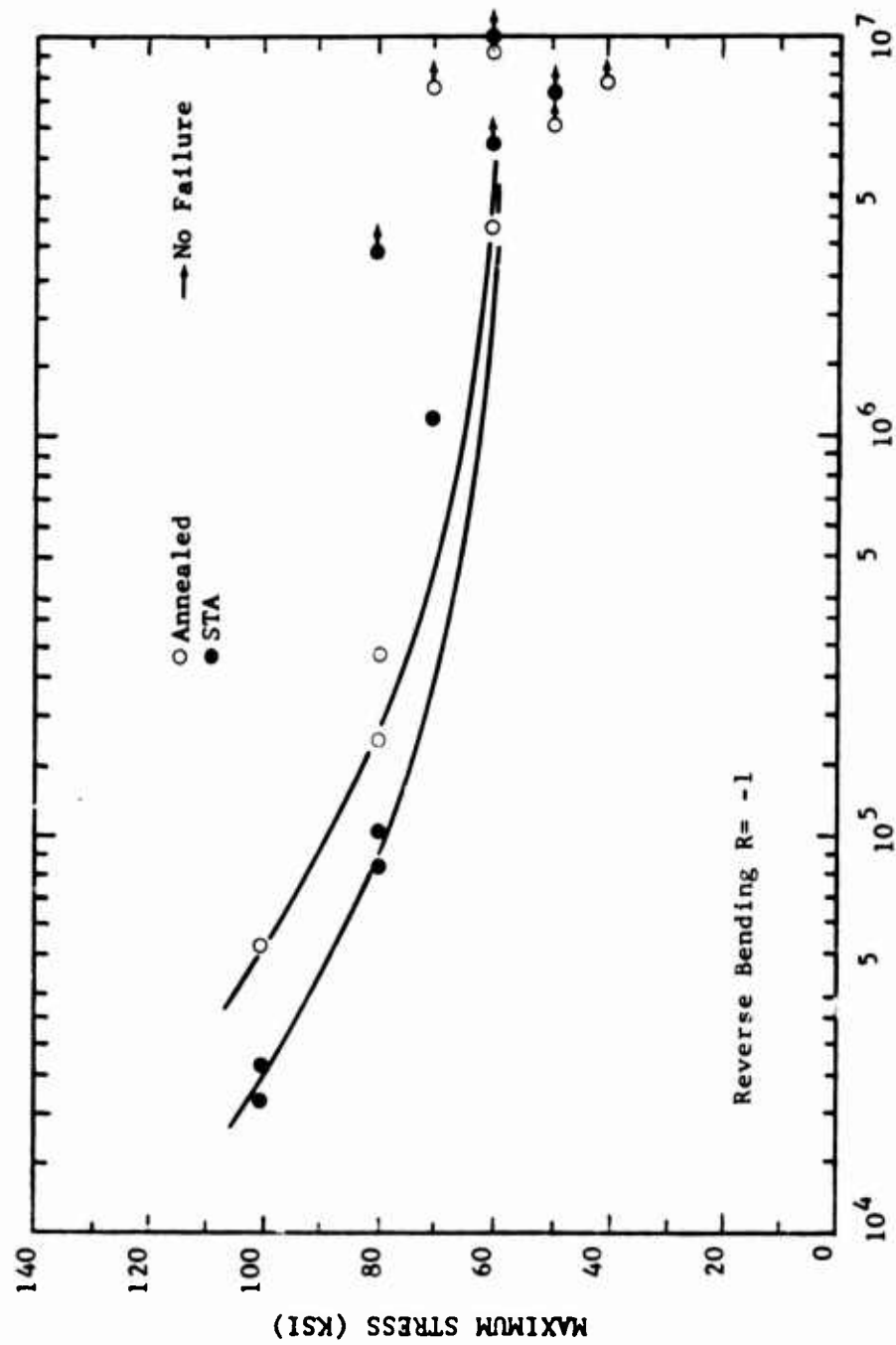
The four welding processes investigated in this program may be directly compared with each other on the basis of single-pass weldments of 0.125-inch or less in thickness. For a weldment which cannot be heat treated after welding, the manual GTA process is most attractive metallurgically. However, this process may not be sufficiently economical nor produce joints of sufficient uniformity to permit its selection. Then, the automatic GTAW process will be the next preference, followed by PAW. Electron beam welding is least attractive from a metallurgical standpoint. As thicknesses increase, process selection shifts to PAW and then EBW, with selection of a welding process controlled primarily by process considerations rather than metallurgical considerations. If preheat can be employed, the as-welded properties of the joints will be improved for each of these processes, although the order of preference of these processes will still remain the same.

In general, titanium should not be used in the as-welded condition because high residual stresses are produced by welding. Normally, a titanium weldment is stress relieved at 1200F for 2 hours in air. If a 200F increase in temperature is used for postweld heat treatment, the elongation can be improved approaching that of the base metal at the expense of a reduction in the fatigue strength. Both the fracture toughness and stress-corrosion resistance will exceed those of the base metal due to this treatment. Then, the efficient welding processes of high heat concentration such as PAW and EBW can be used with simple butt joints. If a vacuum furnace is available, economics permit, and distortion does not present a problem, a 1600F heat-treatment will improve the fracture toughness even higher in a PA weld without further reduction of fatigue strength.



VIII  
REFERENCES

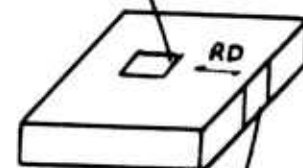
1. Wu, K. C., "Weldability Study of Titanium 8Al-1Mo-1V, Rene' 41, and Rene' 63," Northrop Report NOR 65-250, October 1965.
2. Wu, K. C., "Qualitative Evaluation of the Heat-Affected Zone in the Tungsten Inert Gas Welding of Titanium Alloys," Watervliet Arsenal Memorandum Report, May 19, 1961.
3. Lewis, R. E. and Wu, K. C., "A Study of Weld Heat-Affected Zone in Titanium 6Al-6V-2Sn," Welding Journal Research Supplement 42, June 1963, pp 241S to 251S.
4. Simpson, R. P. and Wu, K. C., "Microstructure-Property Control With Postweld Heat Treatment of Ti-6Al-6V-2Sn," to be published in the Welding Journal Research Supplement.
5. Srawley, J. E. and Brown, W. F., "Fracture Toughness Testing," NASA TN-D-2599, January 1965.
6. Payne, W. W., "Practical Specimens for  $K_{IC}$  Measurement," Second Annual Workshop in Fracture Mechanics, Denver University, August 1965.
7. Duwez, P., "Effect of Rate of Cooling on the Alpha-Beta Transformation in Titanium and Titanium-Molybdenum Alloy," Transaction AIME Journal of Metals, September 1951, p 765.
8. Curtis, R. E. and Spurr, W. F., "Effect of Microstructure on the Fracture Properties of Titanium Alloys in Air and Salt Solution," Transaction ASM, 61, March 1968, p 115.
9. Fager, D. F. and Spurr, W. F., "Some Characteristics of Aqueous Stress-Corrosion in Titanium Alloys," Transaction ASM, 61, June 1968, p 283-292.
10. Wu, K. C., "Dual Filler-Metal Welding of Ti-6Al-6V-2Sn and 6061 Aluminum Alloys," Welding Journal Research Supplement 48, p 359S, August 1969.



CYCLES TO FAILURE  
 FIGURE 1. S-N CURVES FOR Ti-6Al-6V-2Sn BASE METAL



Top View



Transverse View  
Hardness  $R_c$  35

FIGURE 2. BASE METAL MICROSTRUCTURE, AS-RECEIVED  
MILL ANNEALED 500X

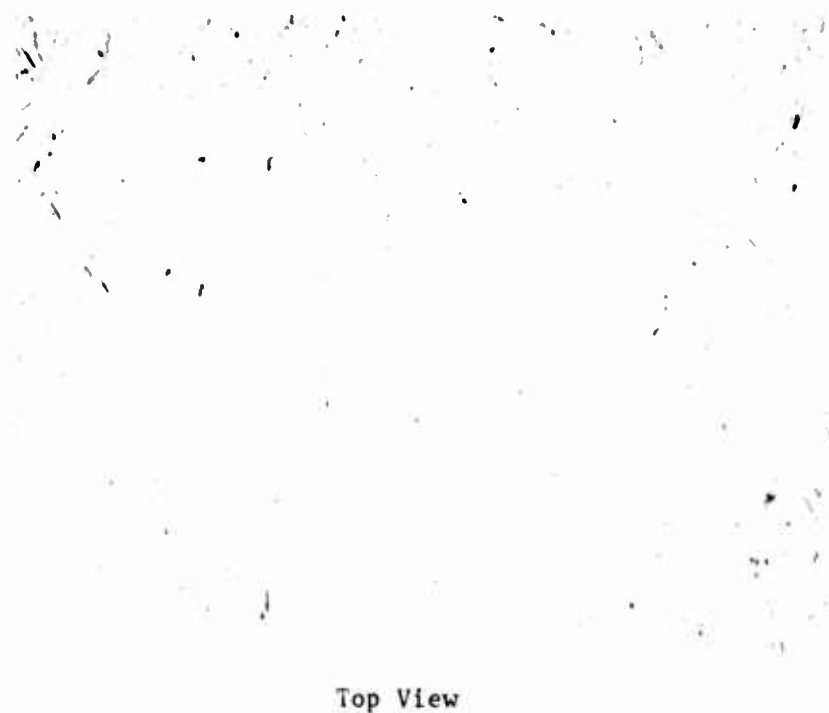


Top View



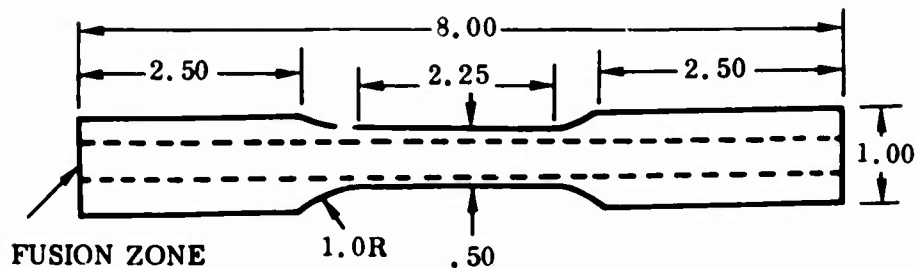
Transverse View  
Hardness  $R_c$  38

FIGURE 3. BASE METAL MICROSTRUCTURE, SOLUTION-TREATED  
1650F - 1 HR, WATER QUENCH 500X

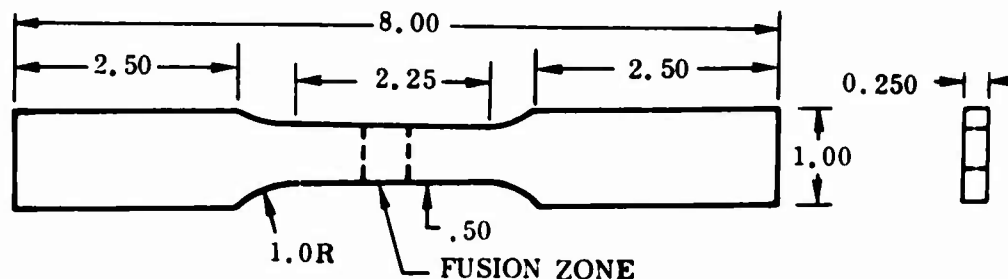


Hardness  $R_c$  41

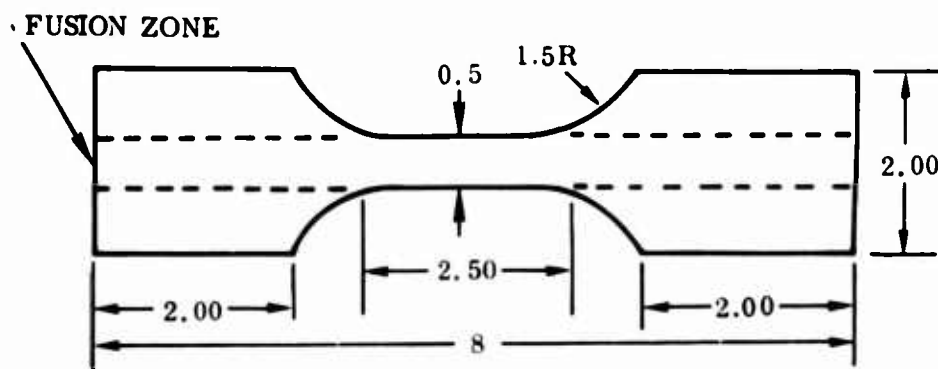
FIGURE 4. BASE METAL MICROSTRUCTURE, SOLUTION TREATED 1650F - 1 HR, WATER QUENCH, AND AGED 1050F - 4 HRS 500X



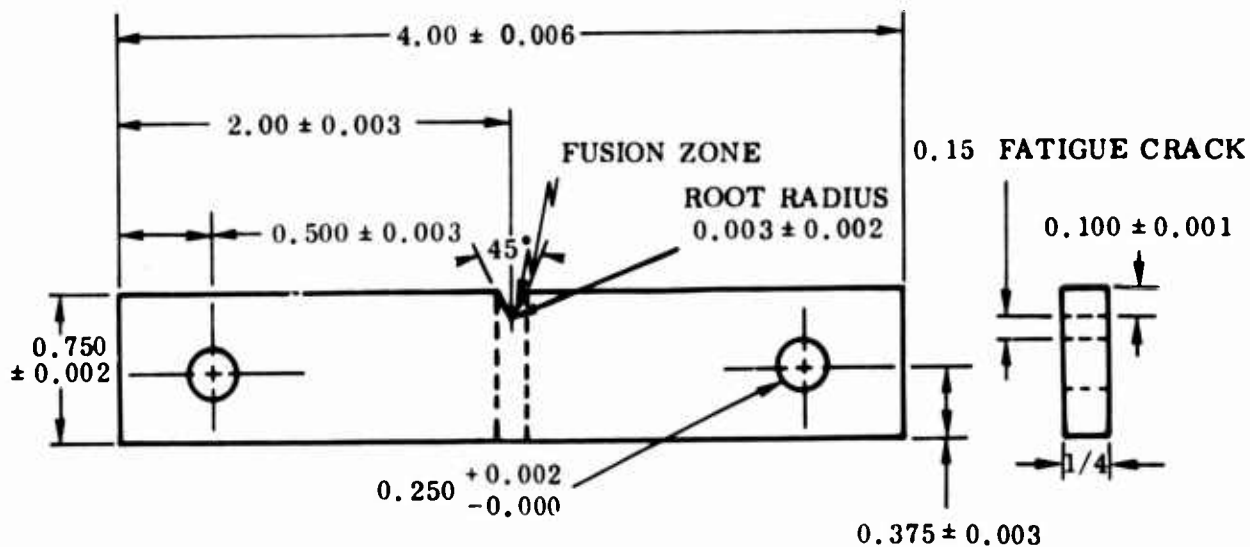
LONGITUDINAL TENSILE TEST SPECIMEN



TRANSVERSE TENSILE TEST SPECIMEN



FATIGUE TEST SPECIMEN



SINGLE-EDGE-NOTCHED SPECIMEN FOR FRACTURE  
TOUGHNESS AND STRESS CORROSION TESTS  
(DIMENSION IN INCHES)

FIGURE 5. CONFIGURATION OF MECHANICAL TEST SPECIMENS



FIGURE 6. THE GLEEBLE

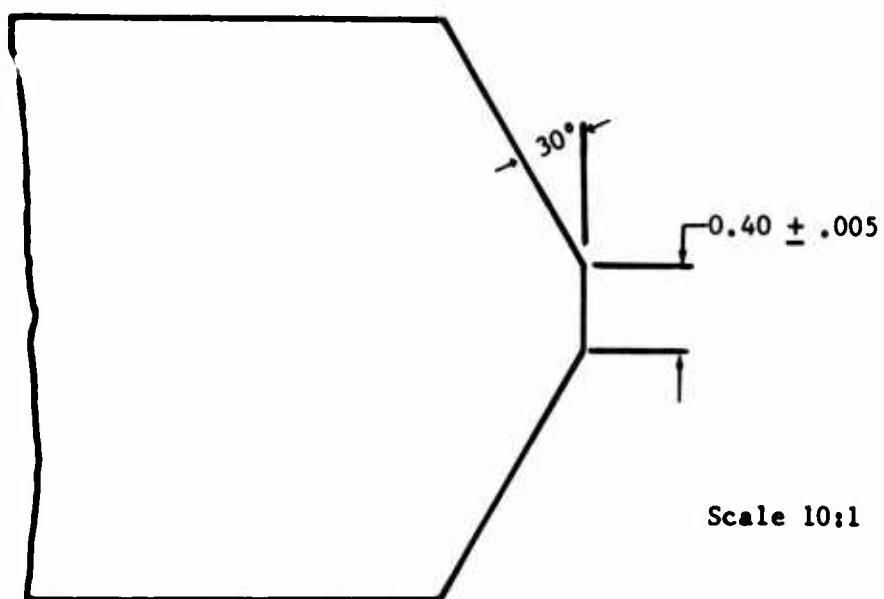


FIGURE 7. JOINT CONFIGURATION FOR AUTOMATIC AND MANUAL  
GTA WELDING





FIGURE 8. MANUAL GTA WELDING SET-UP IN AN ATMOSPHERE CHAMBER



FIGURE 9. AUTOMATIC GTA WELDING EQUIPMENT MODIFIED FOR DUAL FILLER-METAL PROCESS



FIGURE 10. MANUAL GTA WELDED PLATE

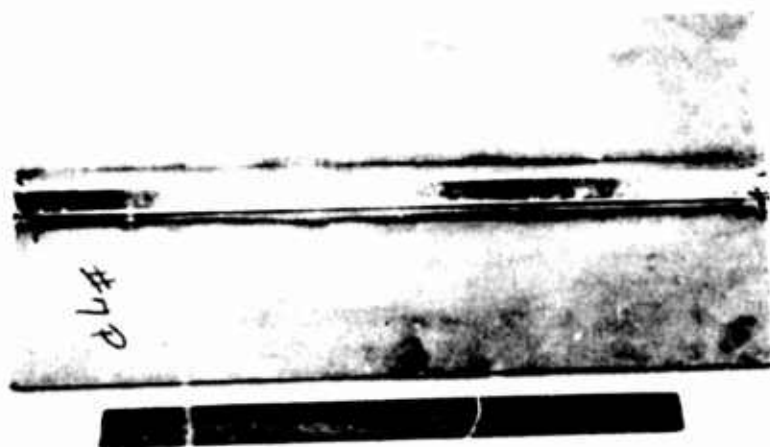


FIGURE 11. PLASMA ARC WELDED PLATE

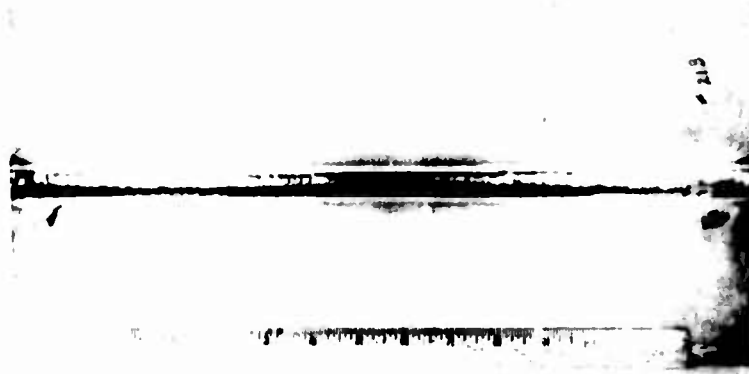


FIGURE 12. AUTOMATIC GTA WELDED PLATE

2 -



FIGURE 13. ELECTRON BEAM WELDED PLATE

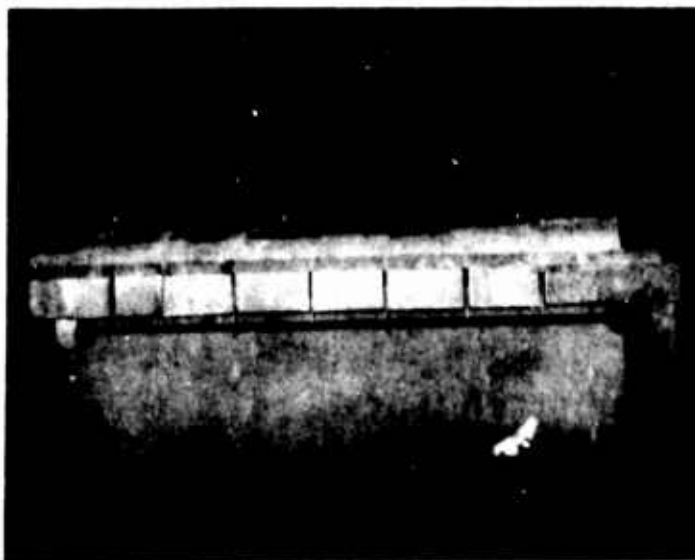


FIGURE 14. WELDING PLATE SET-UP FOR RECORDING THERMAL CYCLES IN THE HEAT-AFFECTED ZONE

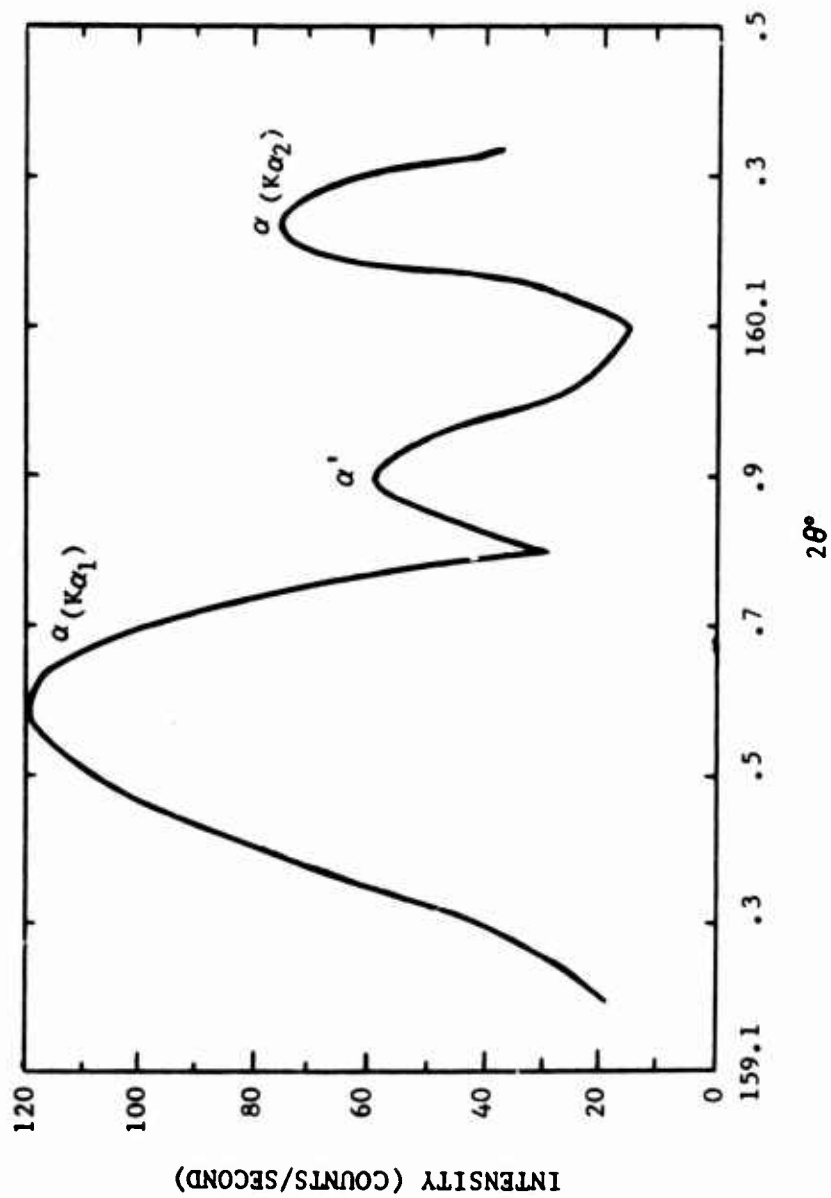


FIGURE 15. X-RAY DIFFRACTION INTENSITY RECORDING FOR ALPHA PHASE IN A HEAT-AFFECTED ZONE SPECIMEN COOLED FROM 2500F AT A COOLING RATE OF 366F/SEC

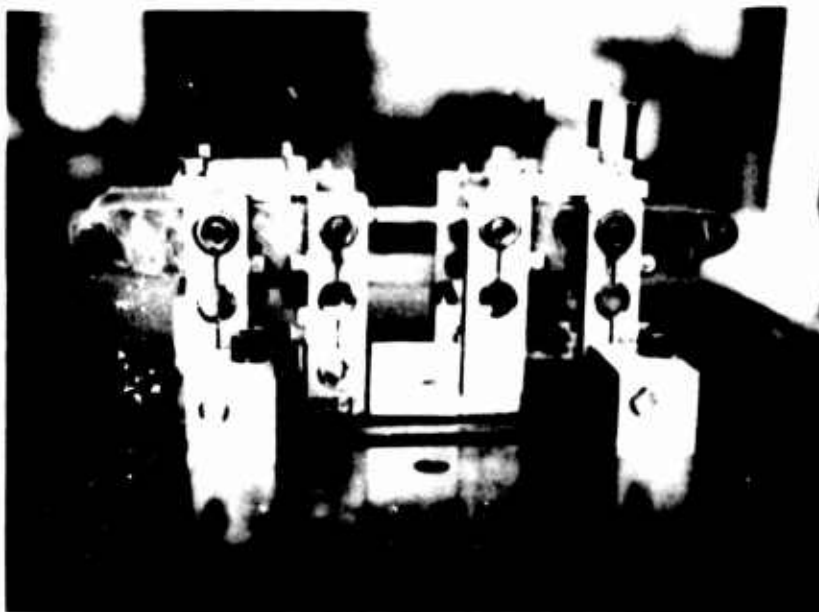
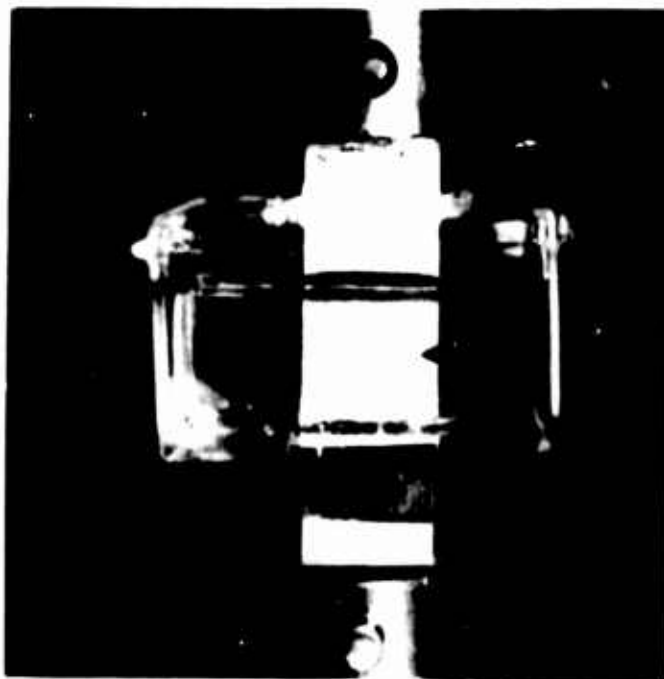


FIGURE 16. REVERSE BENDING FATIGUE TEST IN PROGRESS



A. Specimen Installed for Precracking Operation



B. Specimen Installed for Stress-Corrosion Test

FIGURE 17. STRESS-CORROSION TEST SET-UP

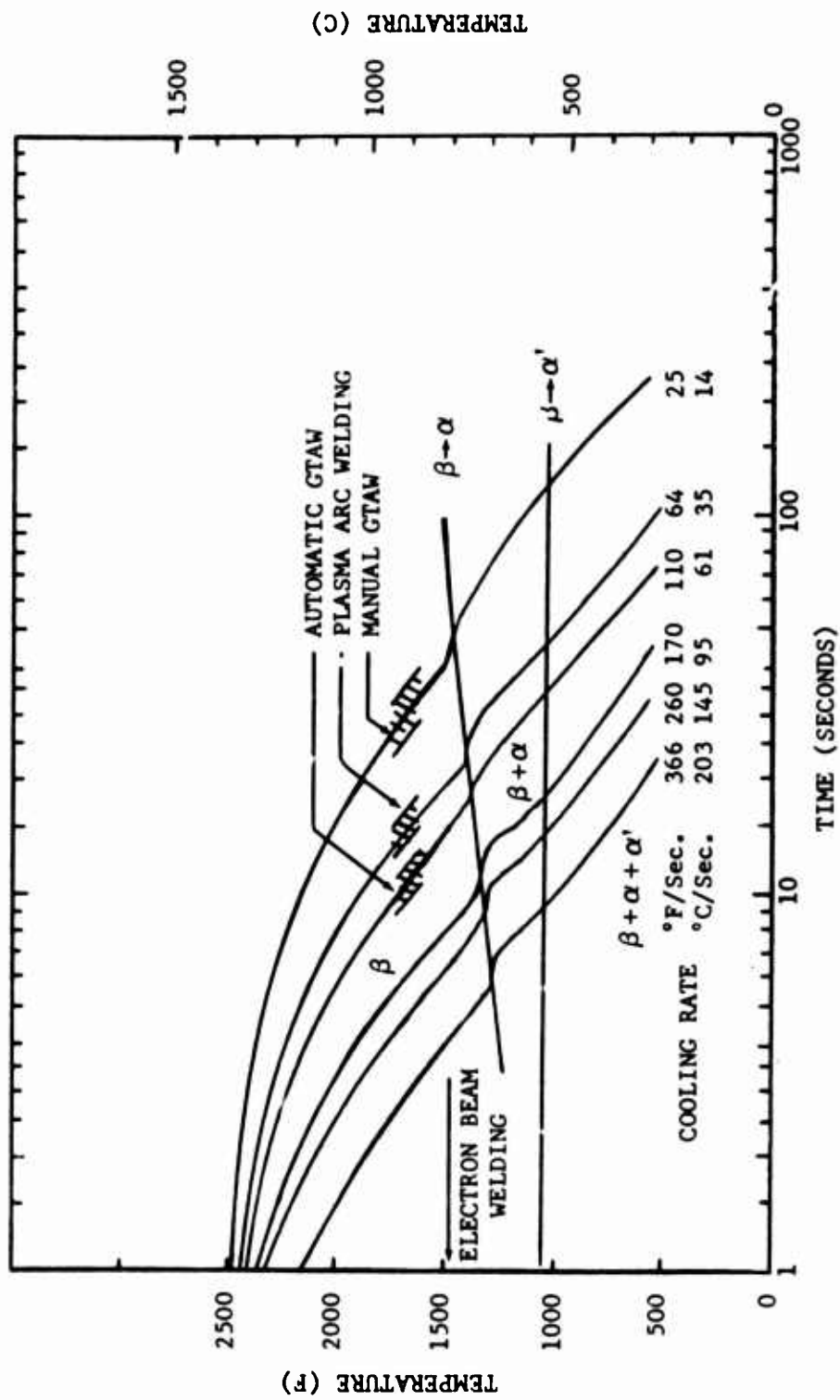


FIGURE 18. CONTINUOUS COOLING TRANSFORMATION DIAGRAM FOR Ti-6Al-6V-2Sn





FIGURE 19. MICROSTRUCTURE OF SYNTHETIC HEAT-AFFECTED  
ZONE COOLED AT 366F/SECOND 500X

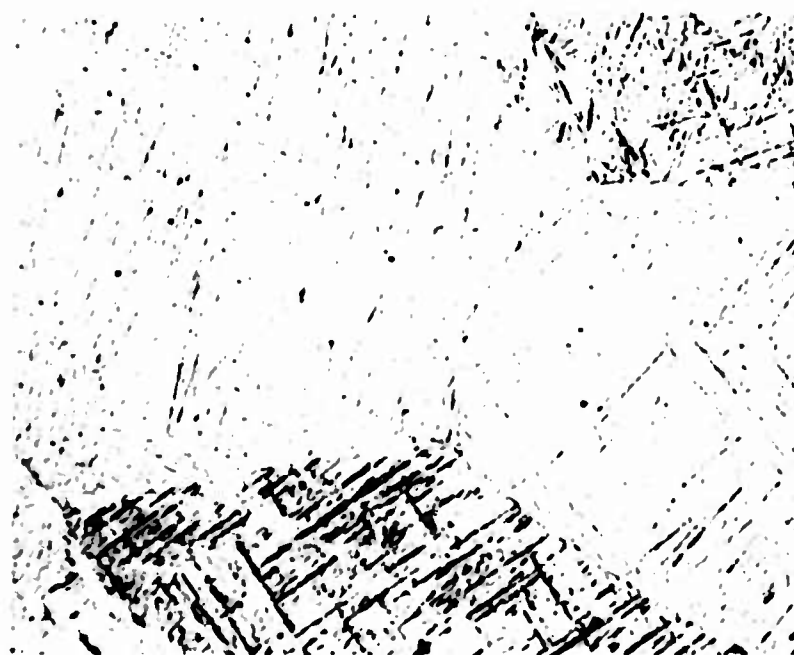


FIGURE 20. MICROSTRUCTURE OF SYNTHETIC HEAT-AFFECTED  
ZONE COOLED AT 110F/SECOND 500X



FIGURE 21. MICROSTRUCTURE OF SYNTHETIC HEAT-AFFECTED  
ZONE COOLED AT 25F/SECOND 500X

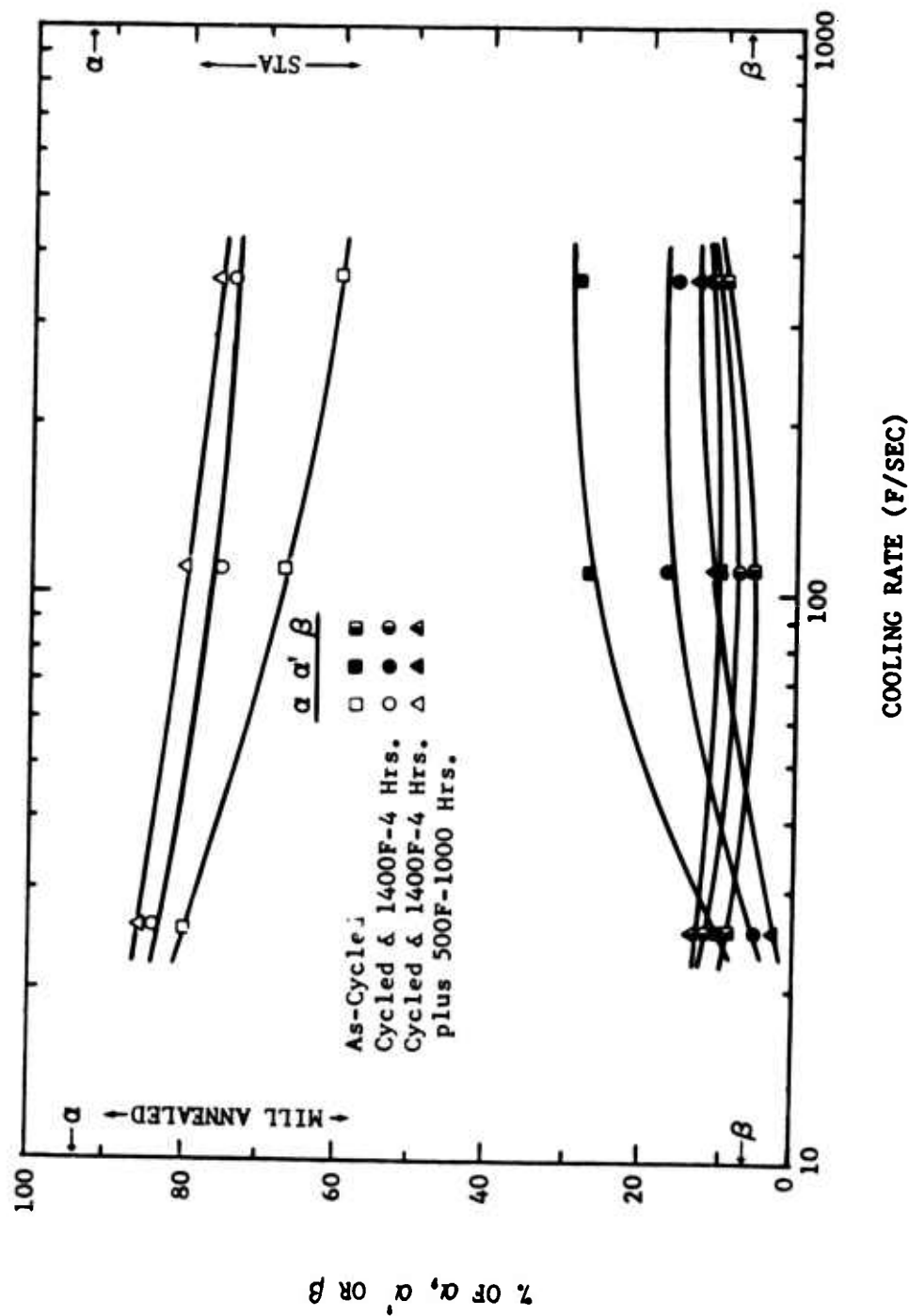


FIGURE 22. EFFECT OF COOLING RATE ON PHASE CONTENTS IN THE SYNTHETIC HEAT-AFFECTED ZONE COOLED FROM 2500F IN AS-CYCLED, HEAT TREATED, AND THERMALLY EXPOSED CONDITIONS

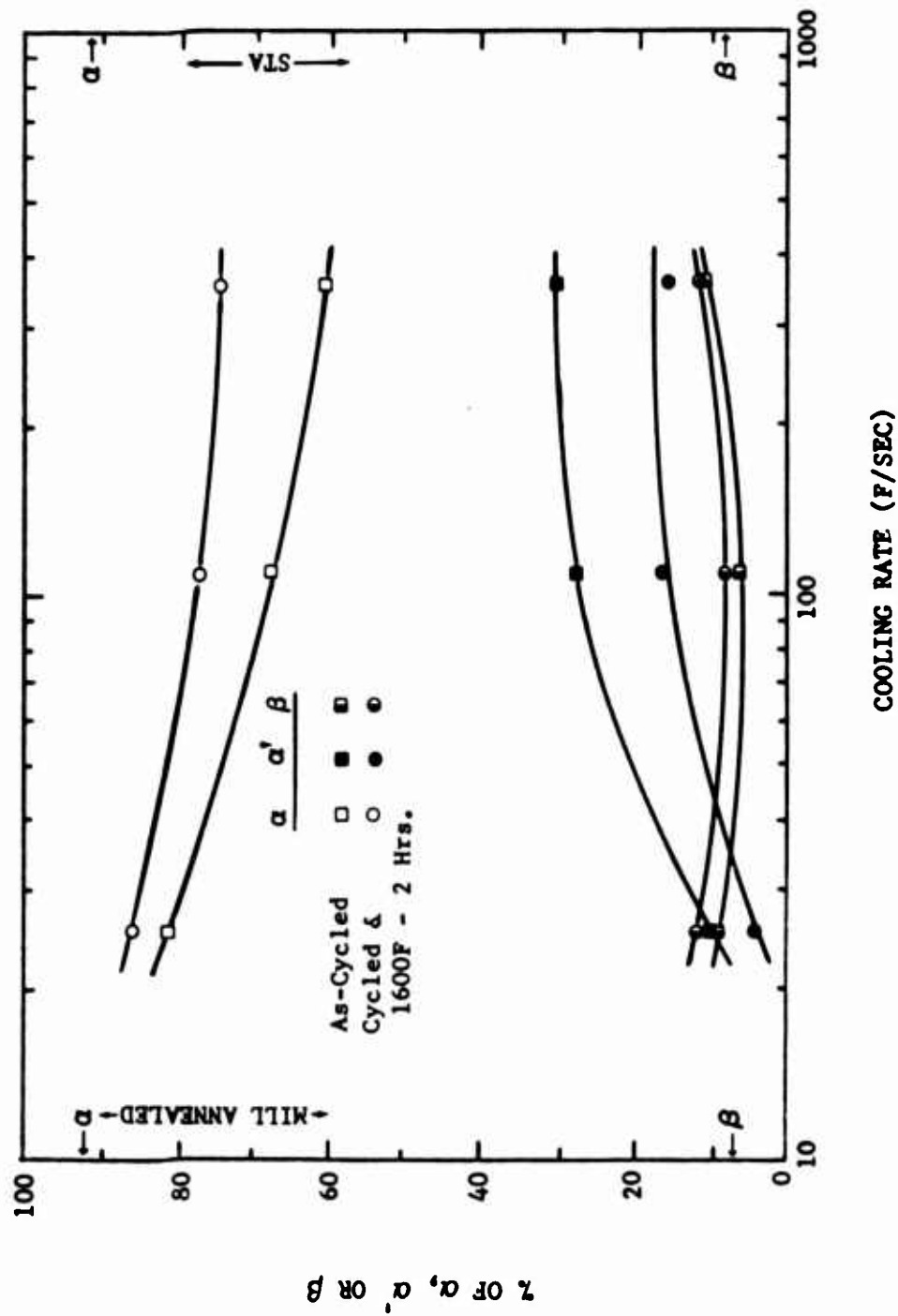


FIGURE 23. EFFECT OF COOLING RATE ON PHASE CONTENTS IN THE SYNTHETIC HEAT-AFFECTED ZONE BEFORE AND AFTER HEAT TREATMENT AT 1600F - 2 HRS.

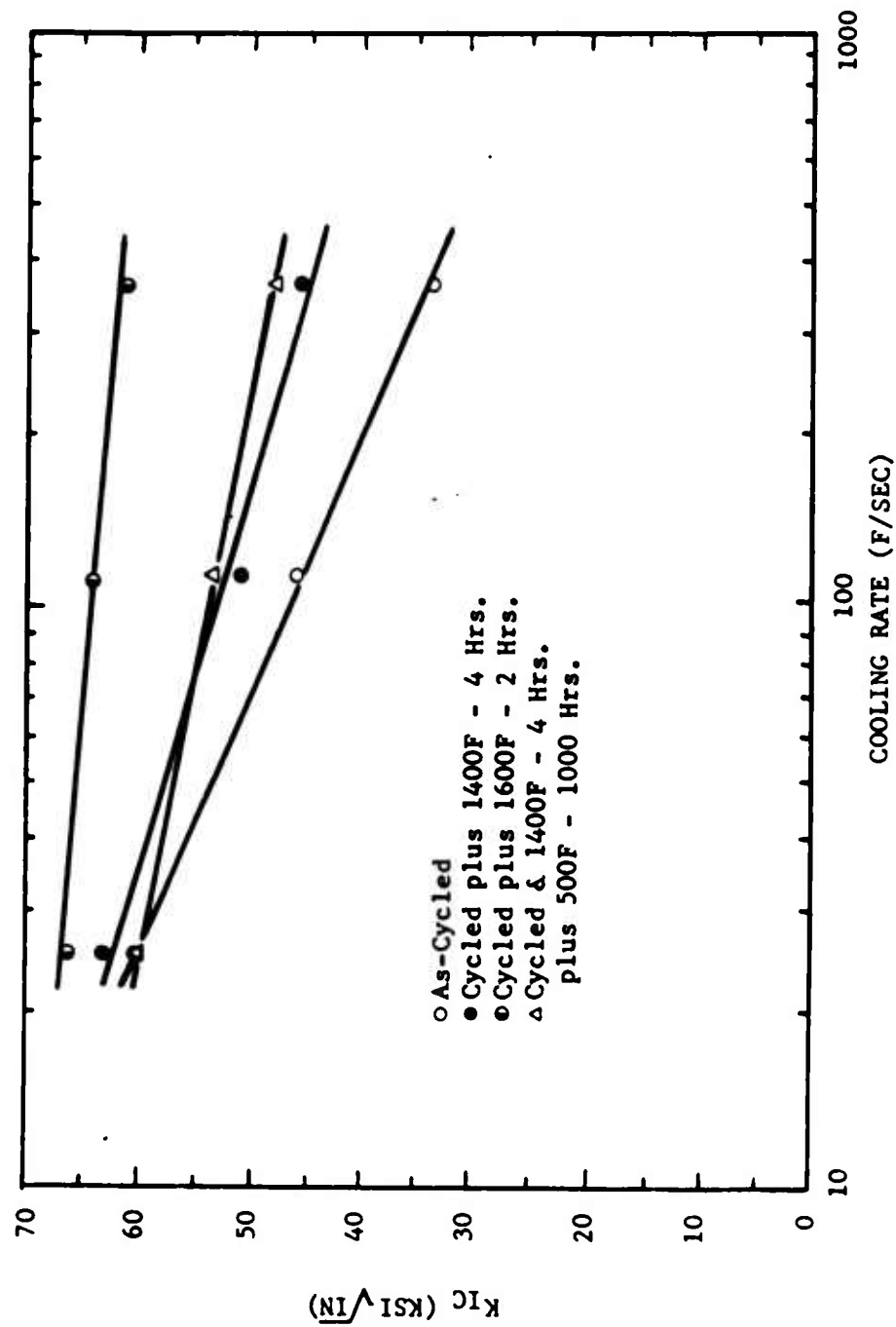


FIGURE 24. EFFECT OF COOLING RATE AND POST-CYCLE HEAT TREATMENT ON FRACTURE TOUGHNESS IN THE SYNTHETIC HEAT-AFFECTED ZONE

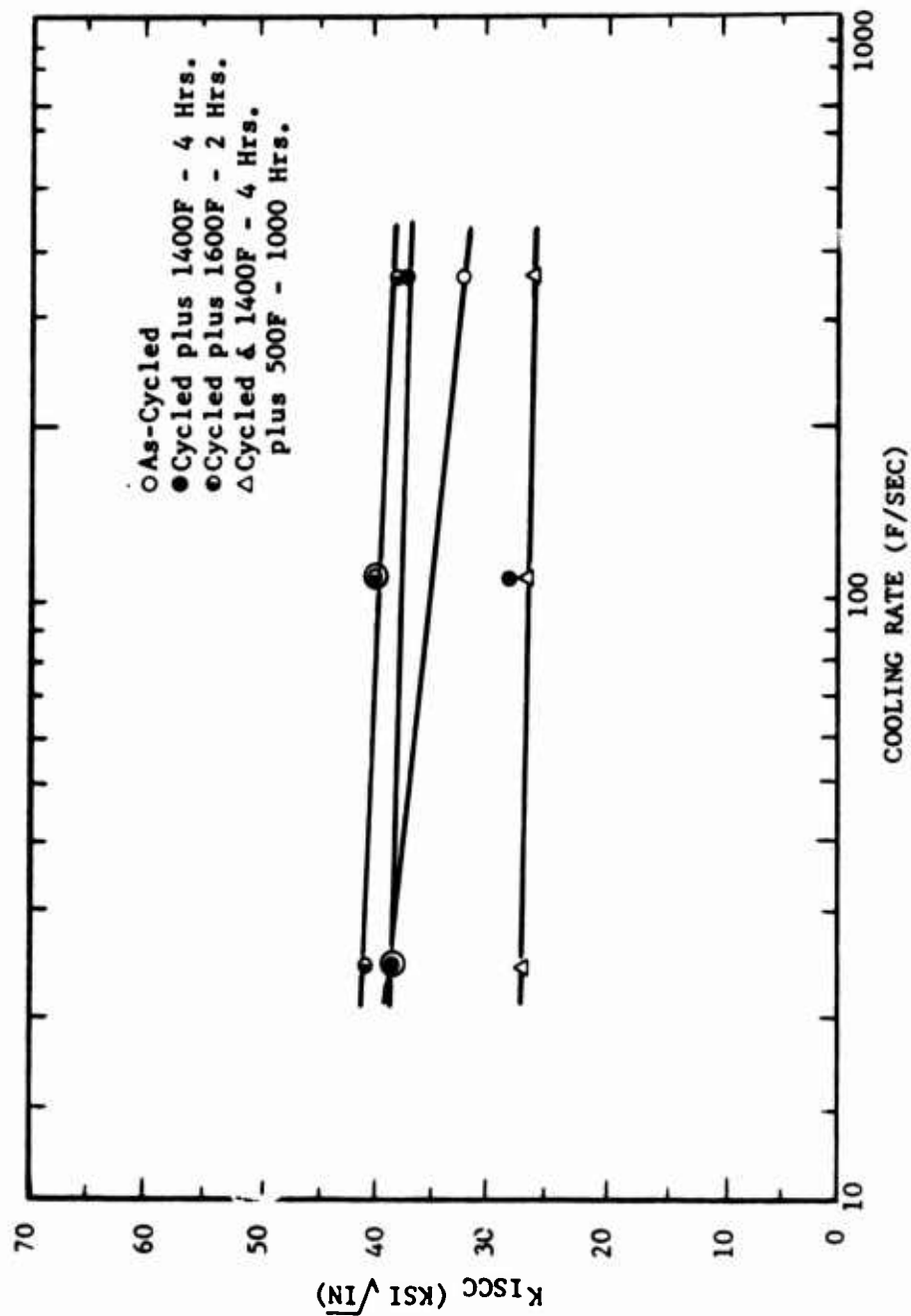


FIGURE 25. EFFECT OF COOLING RATE AND POST-CYCLE HEAT TREATMENT ON STRESS-CORROSION RESISTANCE IN THE SYNTHETIC HEAT-AFFECTED ZONE

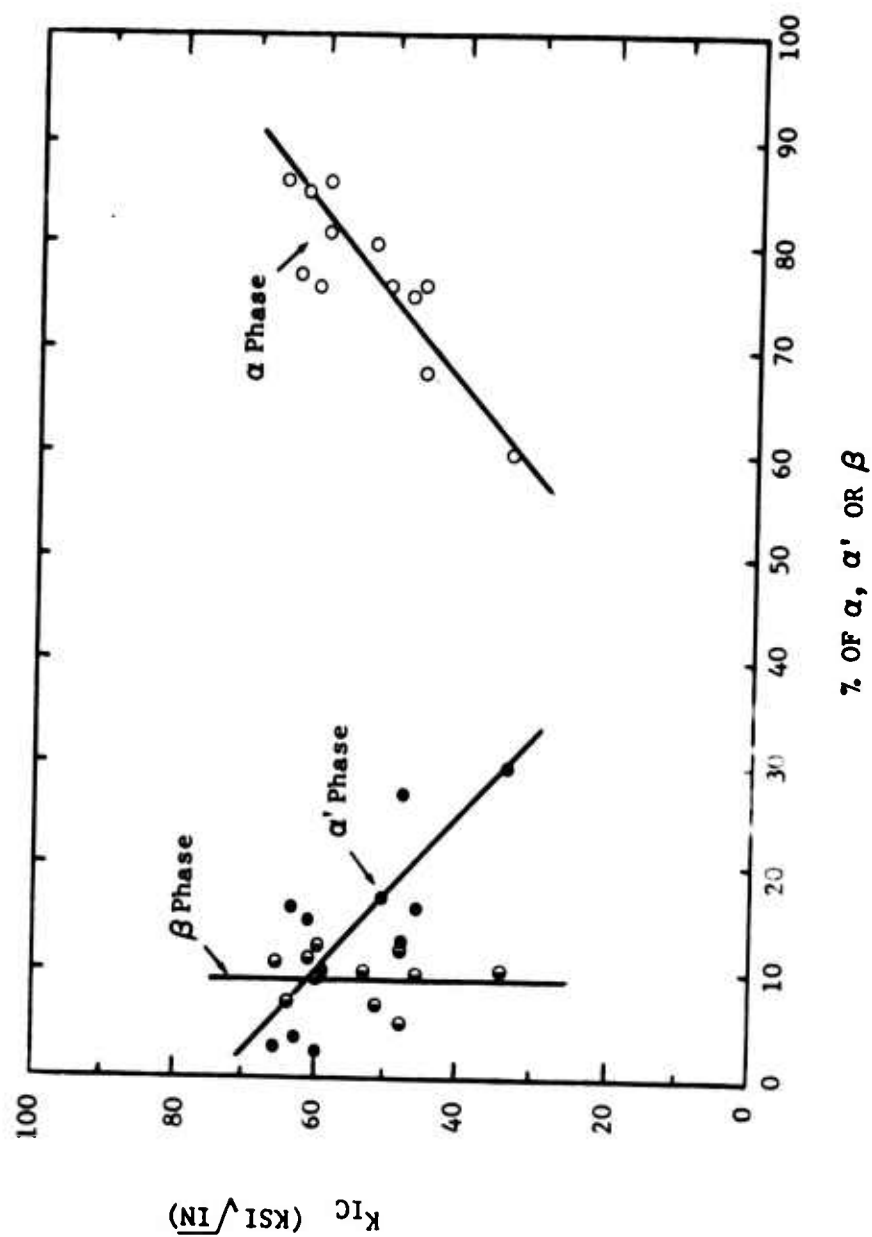


FIGURE 26. EFFECT OF PHASE CONTENTS ON FRACTURE TOUGHNESS OF THE SYNTHETIC HEAT-AFFECTED ZONE, ALL CONDITIONS

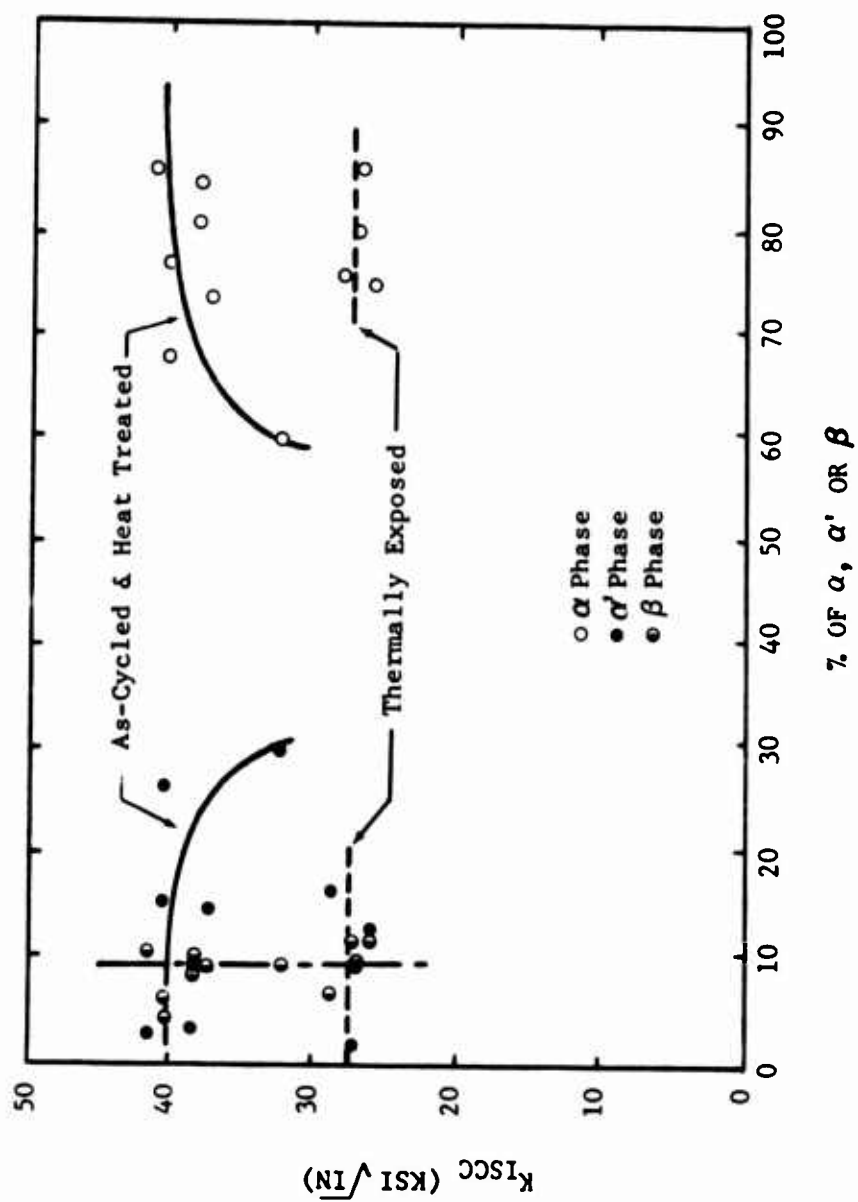


FIGURE 27. EFFECT OF PHASE CONTENTS ON STRESS-CORROSION RESISTANCE OF THE SYNTHETIC HEAT-AFFECTED ZONE, ALL CONDITIONS



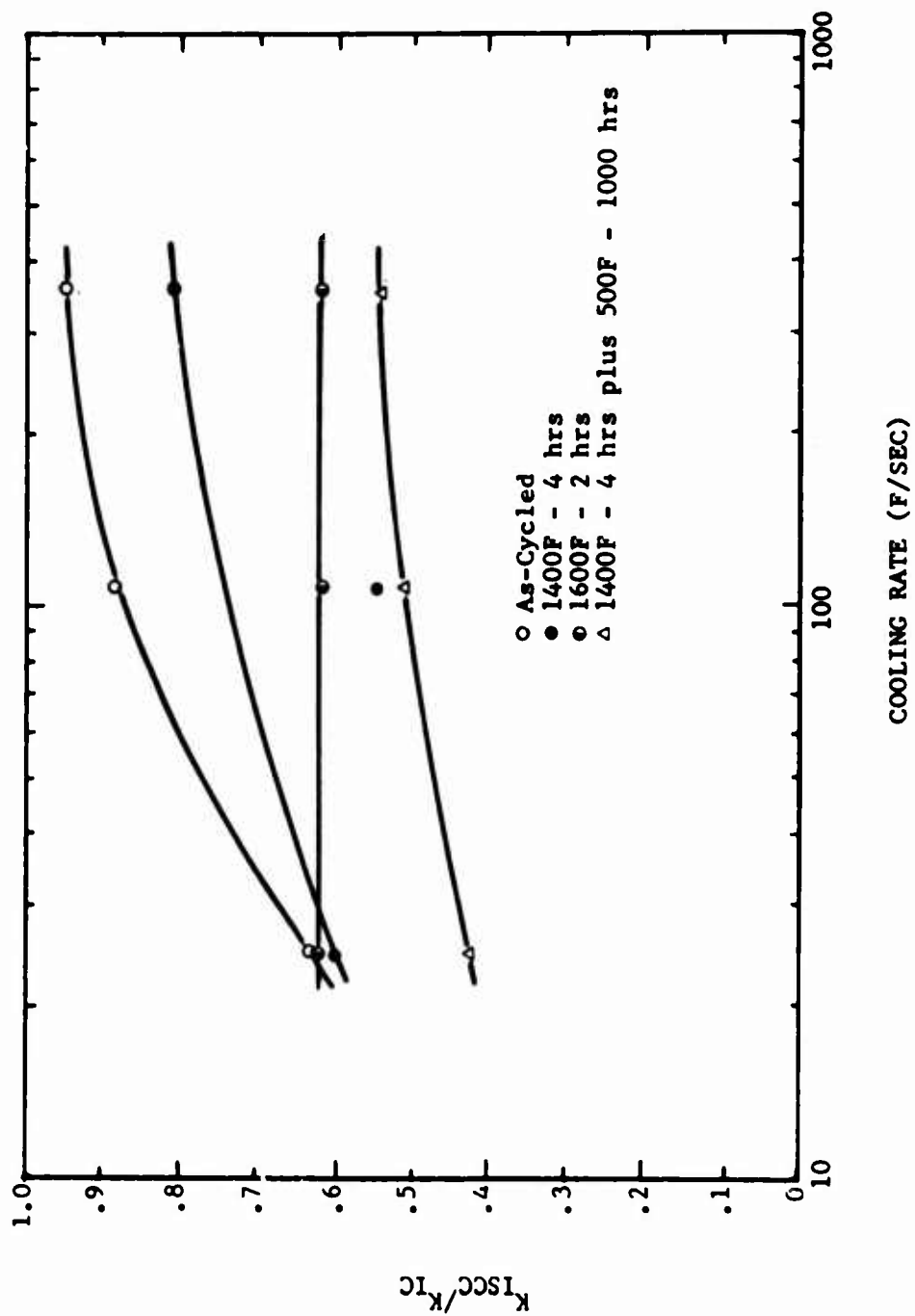


FIGURE 28. EFFECT OF COOLING RATE ON STRESS-CORROSION SUSCEPTIBILITY RATIO OF THE SYNTHETIC HEAT-AFFECTED ZONE, ALL CONDITIONS

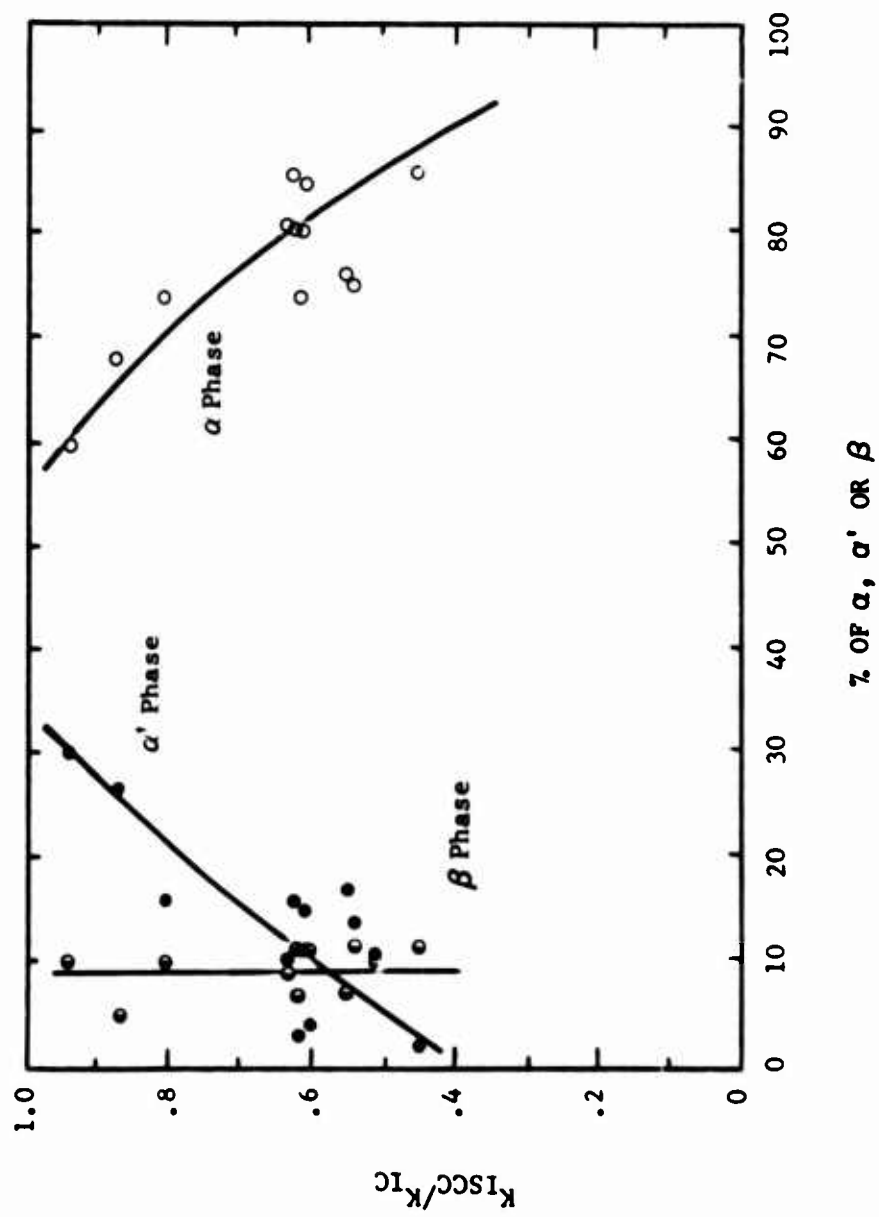
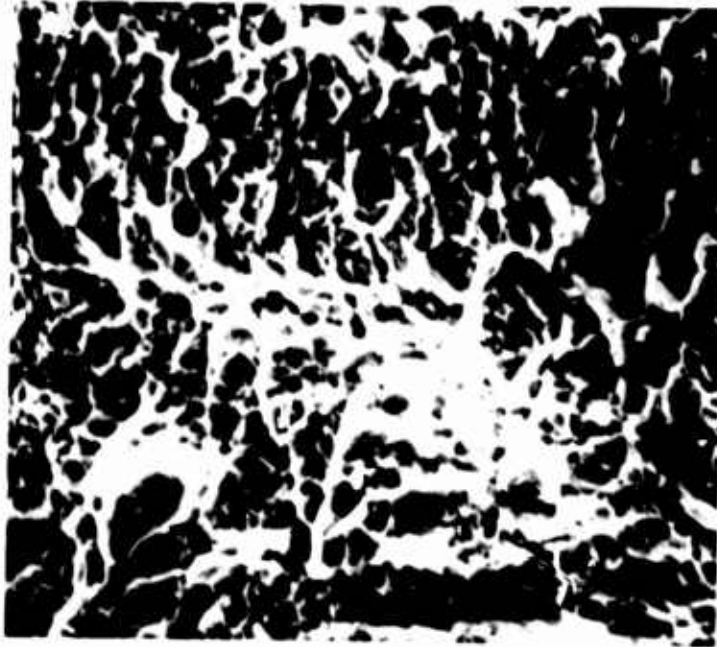


FIGURE 29. EFFECT OF PHASE CONTENTS ON STRESS-CORROSION SUSCEPTIBILITY RATIO OF THE SYNTHETIC HEAT-AFFECTED ZONE, ALL CONDITIONS



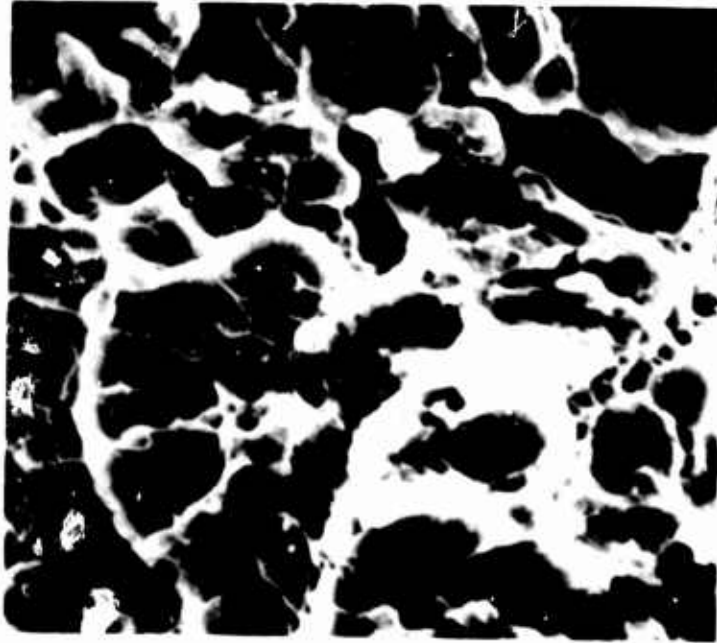
(a)

6X



(b)

700X



(c)

2100X

FIGURE 30. FRACTURE SURFACE OF A SYNTHETIC HEAT-AFFECTED ZONE SPECIMEN  
COOLED AT 366F/SEC AND FRACTURE-TOUGHNESS TESTED

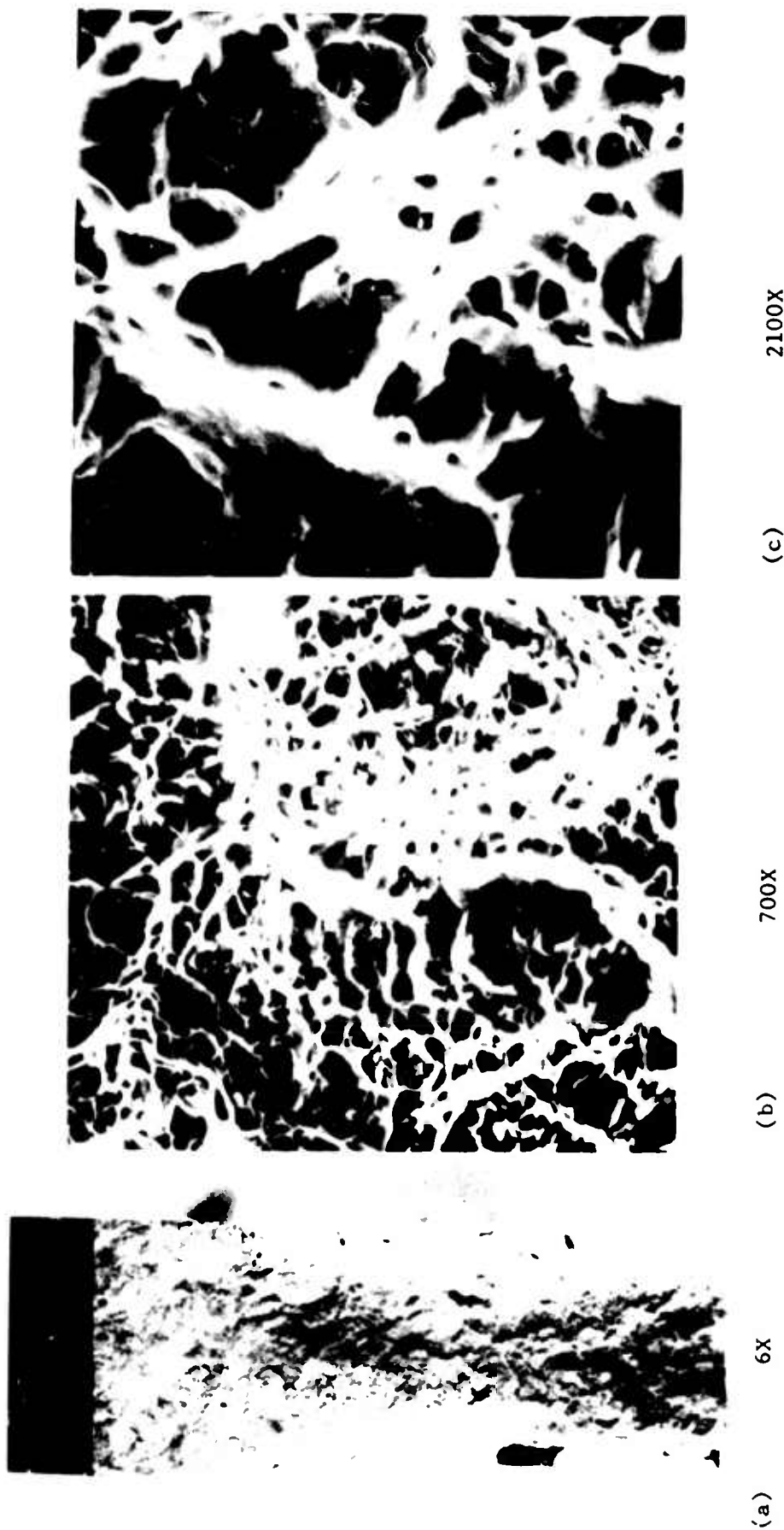
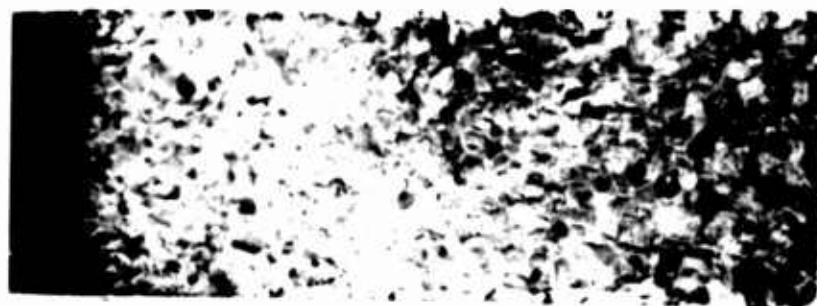


FIGURE 31. FRACTURE SURFACE OF A SYNTHETIC HEAT-AFFECTED ZONE SPECIMEN COOLED AT 25F/SEC,  
HEAT TREATED AT 1600F FOR 2 HRS AND FRACTURE-TOUGHNESS TESTED



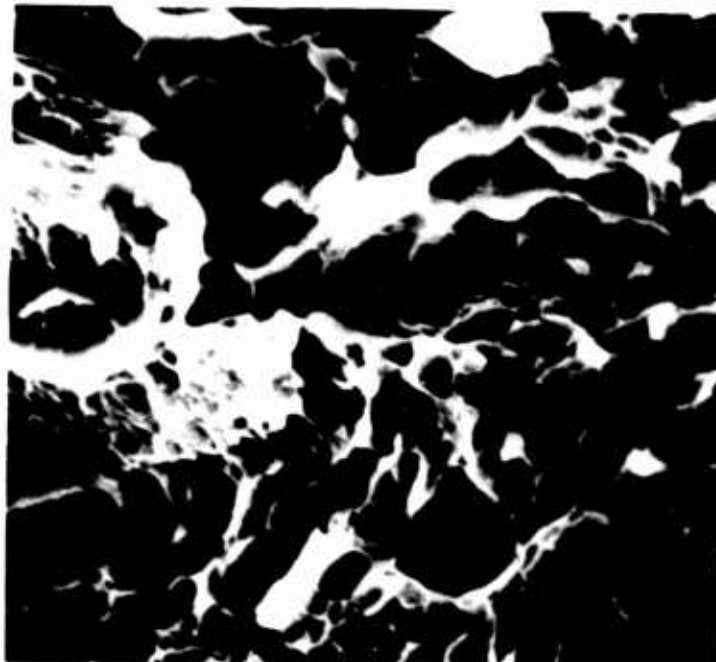
(a)

6X



(b)

700X



(c)

2100X

FIGURE 32. FRACTURE SURFACE OF A SYNTHETIC HEAT-AFFECTED ZONE SPECIMEN COOLED AT 366F/SEC AND STRESS-CORROSION TESTED

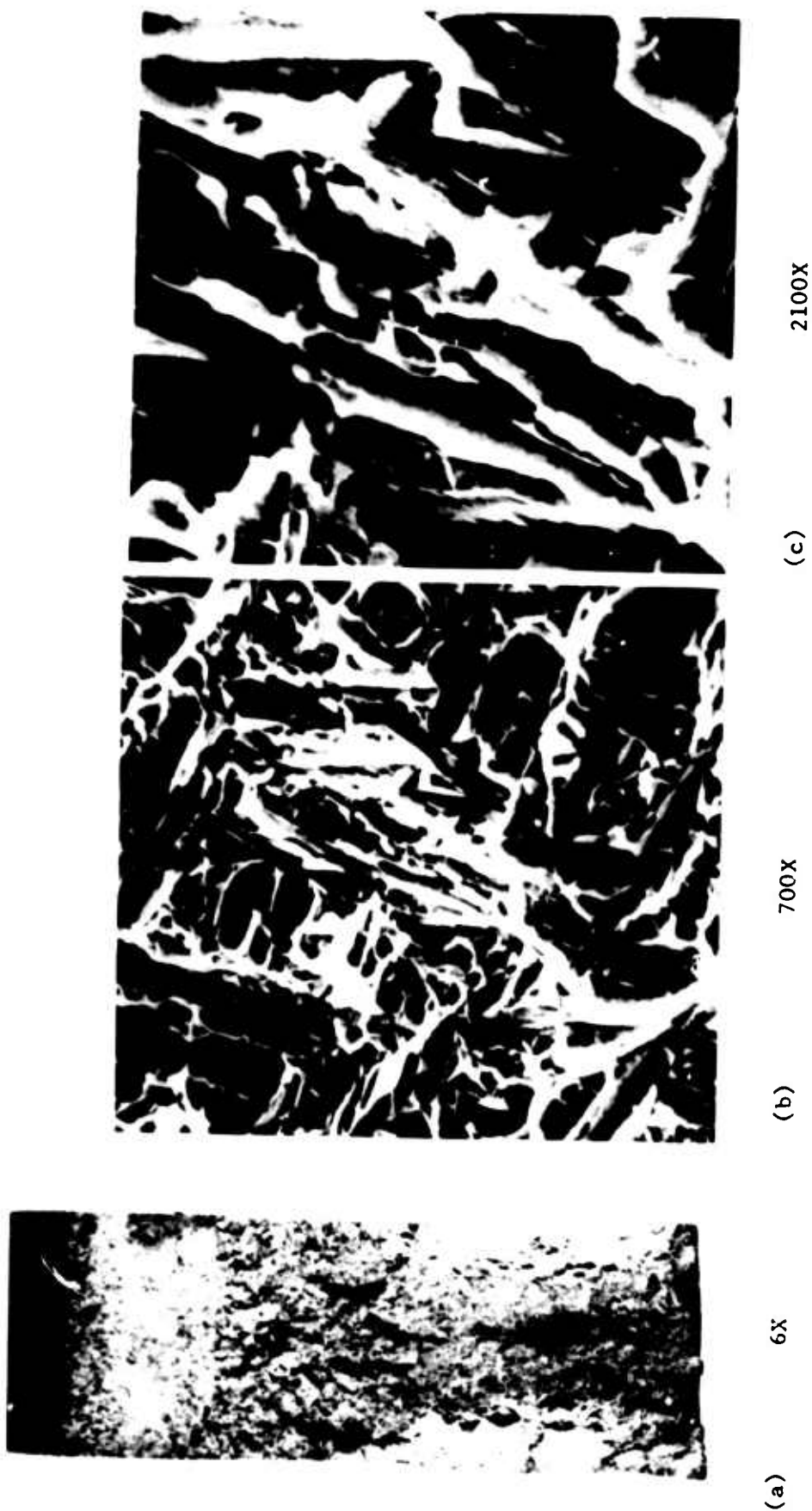


FIGURE 33. FRACTURE SURFACE OF A SYNTHETIC HEAT-AFFECTED ZONE SPECIMEN COOLED AT 25F/SEC, HEAT TREATED AT 1600F FOR 2 HRS AND STRESS-CORROSION TESTED

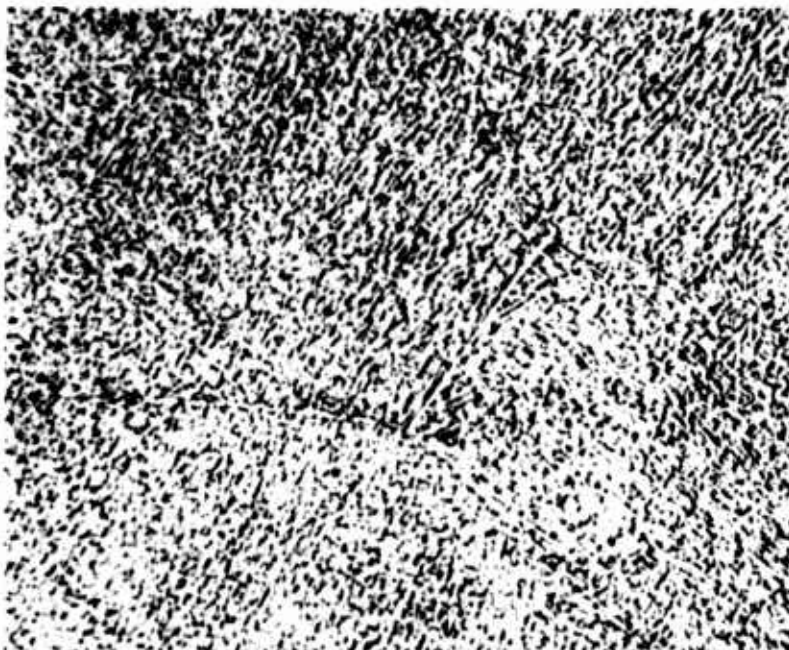


FIGURE 34. SYNTHETIC HEAT-AFFECTED ZONE,  
366F/SEC, 1400F - 4 HRS 500X

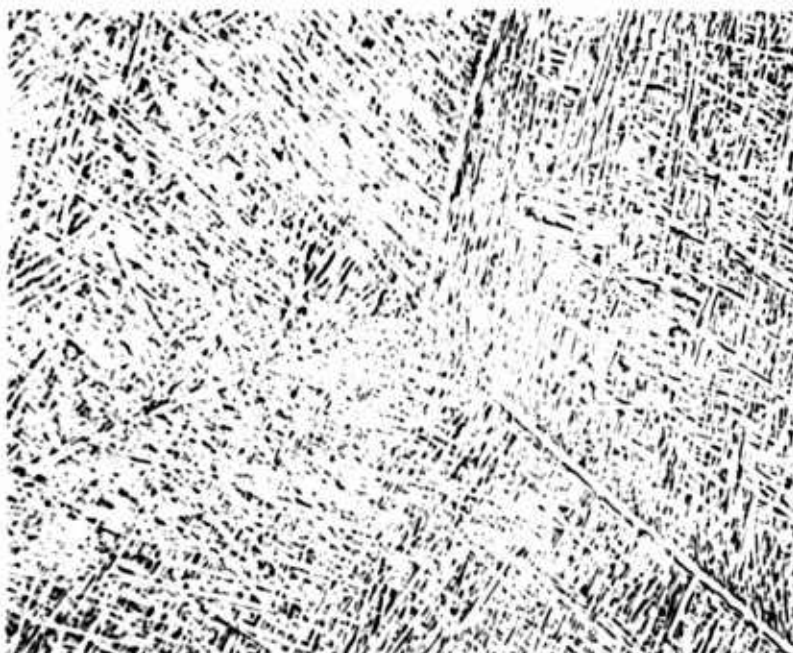


FIGURE 35. SYNTHETIC HEAT-AFFECTED ZONE,  
110F/SEC, 1400F - 4 HRS 500X



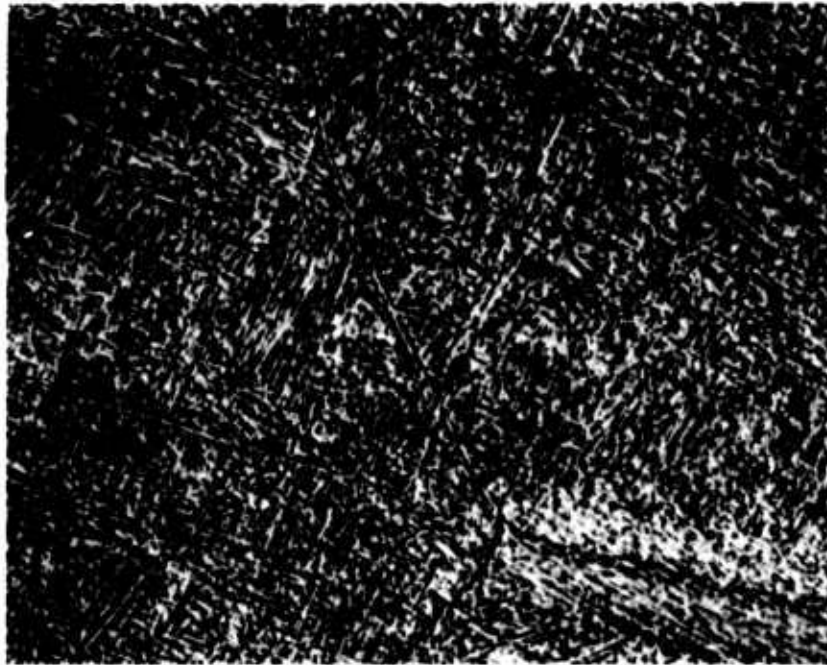


FIGURE 36. SYNTHETIC HEAT-AFFECTED ZONE, 25F/SEC,  
1400F - 4 HRS 500X

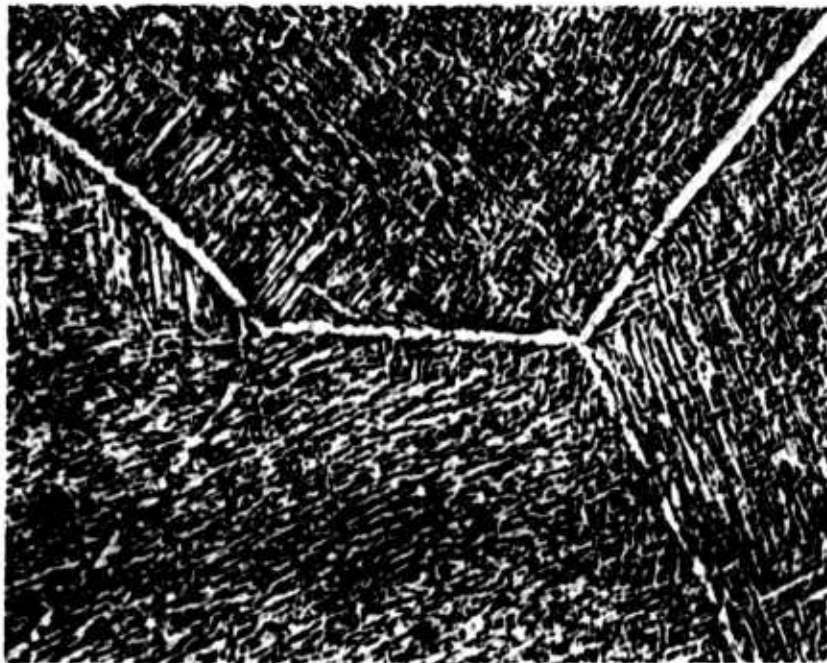


FIGURE 37. SYNTHETIC HEAT-AFFECTED ZONE, 366F/SEC,  
1600F - 2 HRS 500X





FIGURE 38. SYNTHETIC HEAT AFFECTED ZONE, 110F/SEC,  
1600F - 2 HRS 500X

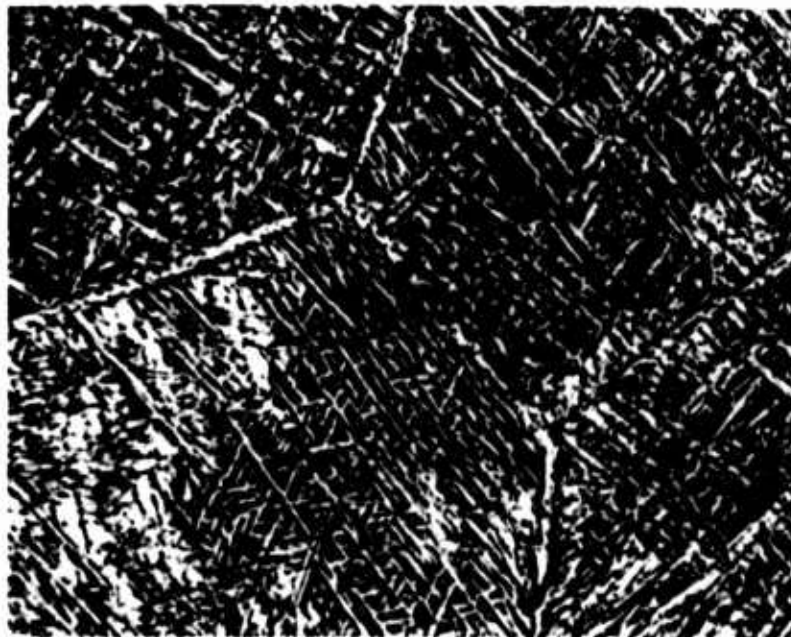


FIGURE 39. SYNTHETIC HEAT-AFFECTED ZONE, 25F/SEC,  
1600F - 2 HRS 500X

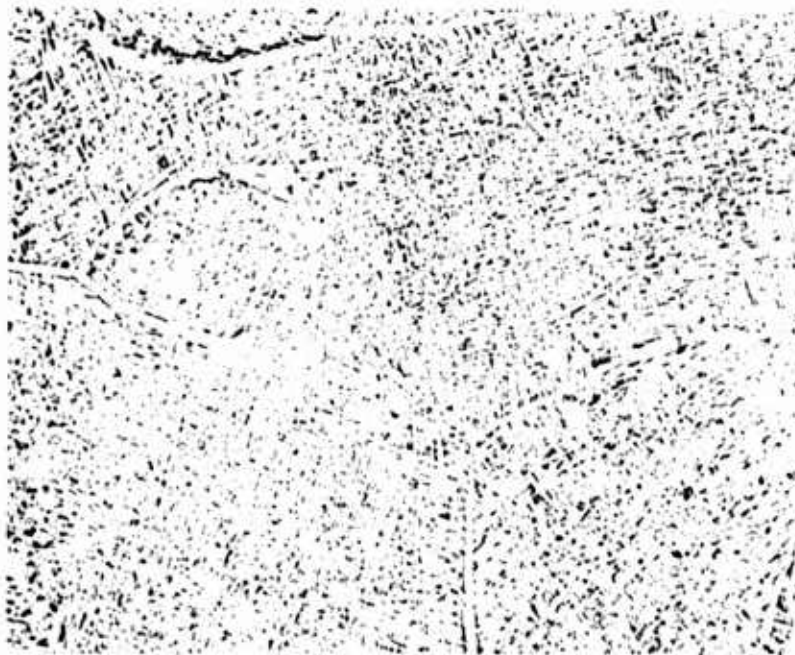


FIGURE 40. SYNTHETIC HEAT-AFFECTED ZONE, 366F/SEC,  
1400 F - 4 HRS PLUS 500F - 1000 HRS  
500X

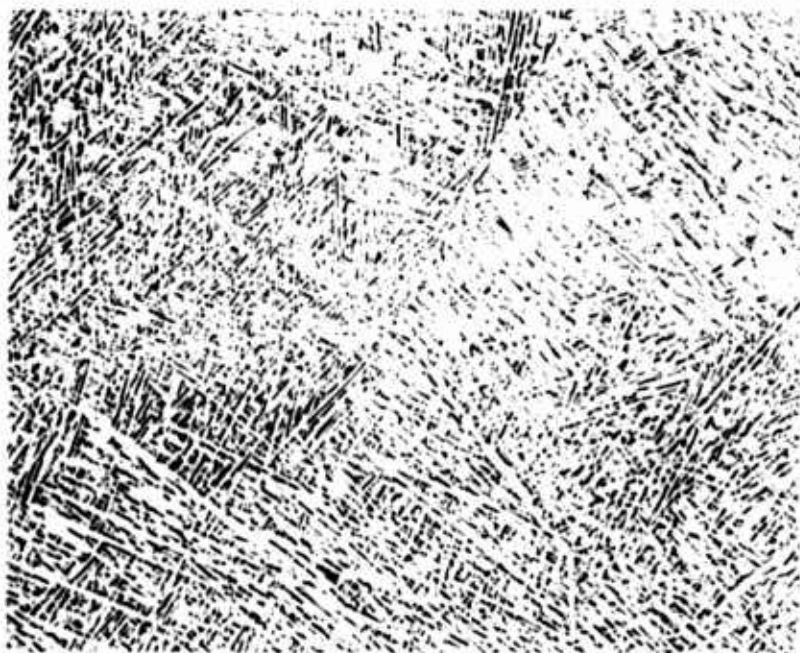


FIGURE 41. SYNTHETIC HEAT-AFFECTED ZONE, 110F/SEC,  
1400F - 4 HRS PLUS 500F - 1000 HRS  
500X



FIGURE 42. SYNTHETIC HEAT-AFFECTED ZONE, 25F/SEC,  
1400F - 4 HRS PLUS 500F - 1000 HRS



FIGURE 43. SOLIDIFICATION PATTERN OF WELD LEAD,  
MANUAL GTAW PROCESS 5X

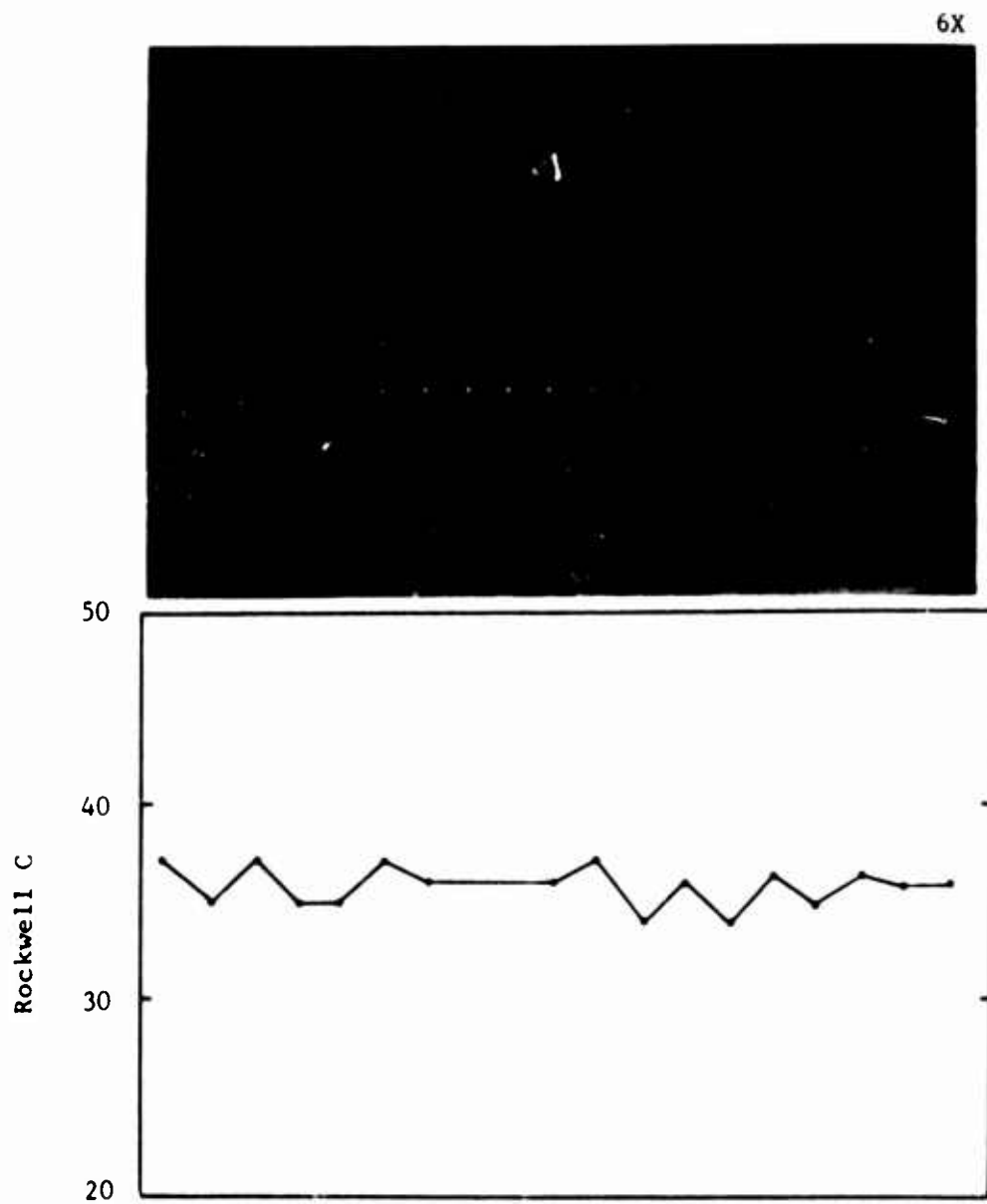
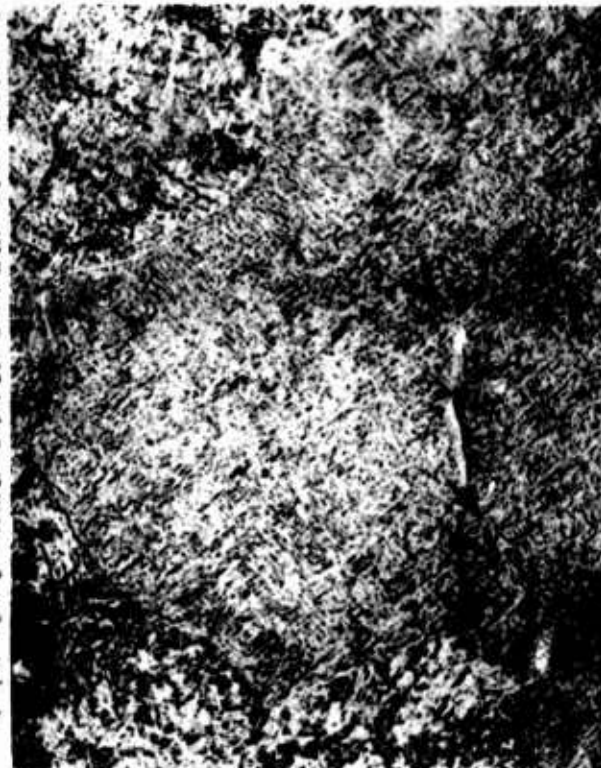
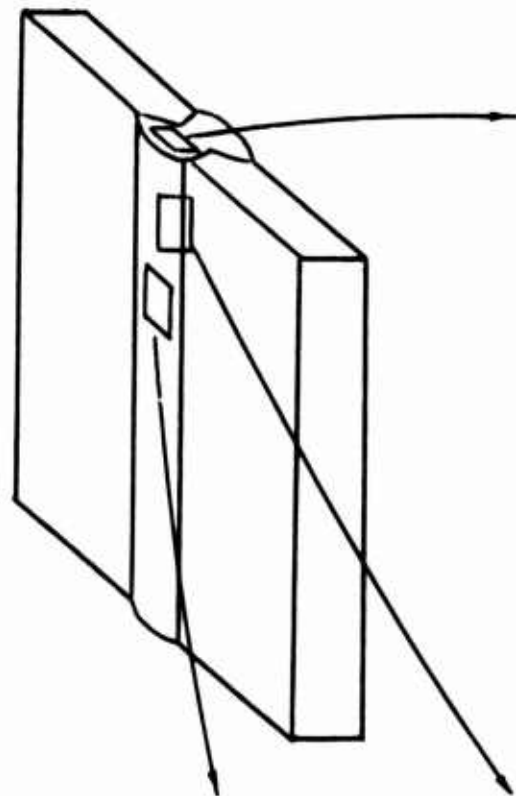
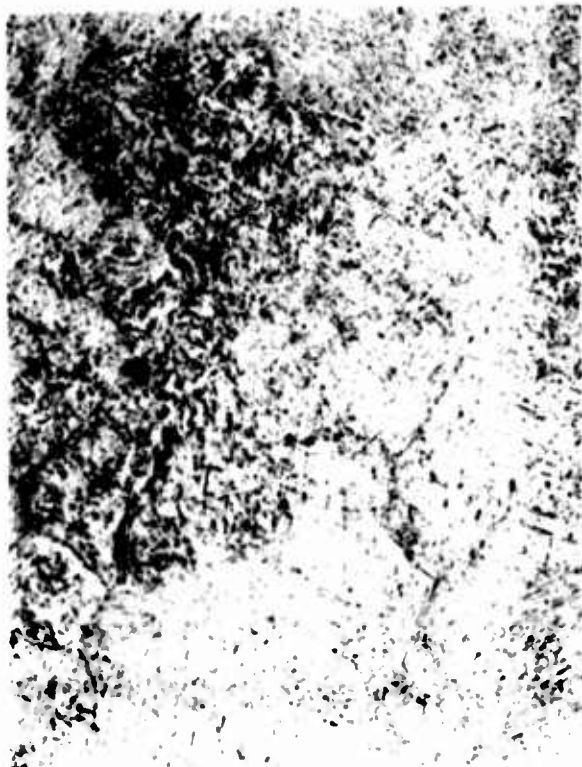


FIGURE 44. MACROSTRUCTURE AND HARDNESS MEASUREMENTS IN A MANUAL GTA WELD USING Ti-6Al-6V-2Sn FILLER METAL

Top View



Longitudinal View



Transverse View

FIGURE 45. MICROSTRUCTURE IN THREE DIRECTIONS OF THE Ti-6Al-6V-2Sn FUSION ZONE USING MATCHING FILLER METAL, MANUAL GTAW PROCESS, AS-WELDED, 100X

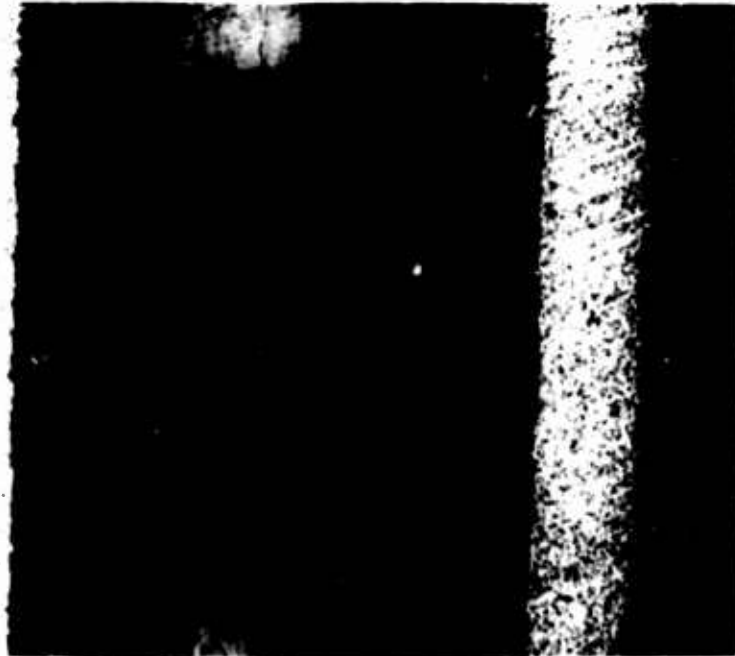


FIGURE 46. SOLIDIFICATION PATTERN OF A WELD BEAD,  
PLASMA ARC WELDING PROCESS 5X

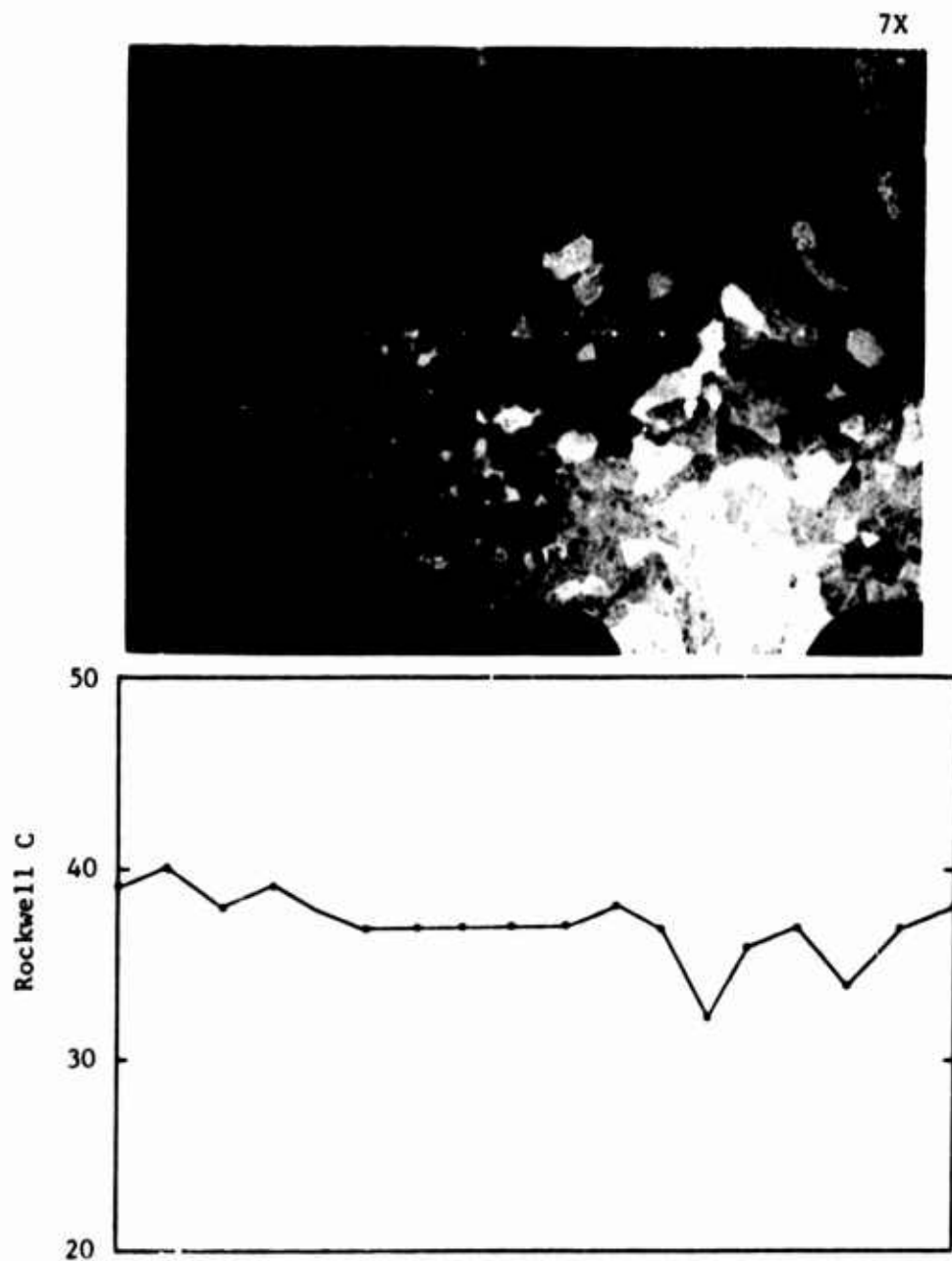
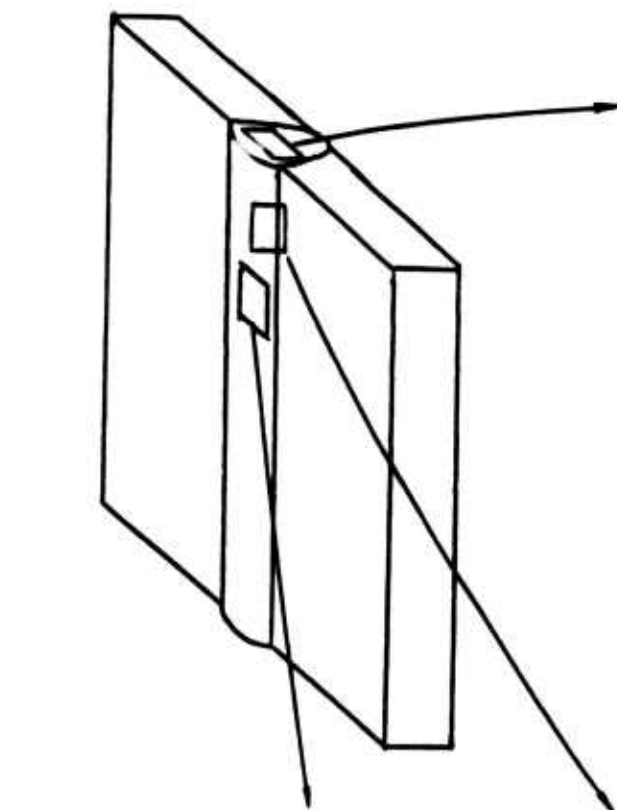


FIGURE 47. MACROSTRUCTURE AND HARDNESS MEASUREMENTS IN A PLASMA ARC WELD WITHOUT FILLER METAL



Top View



Transverse View



Longitudinal View

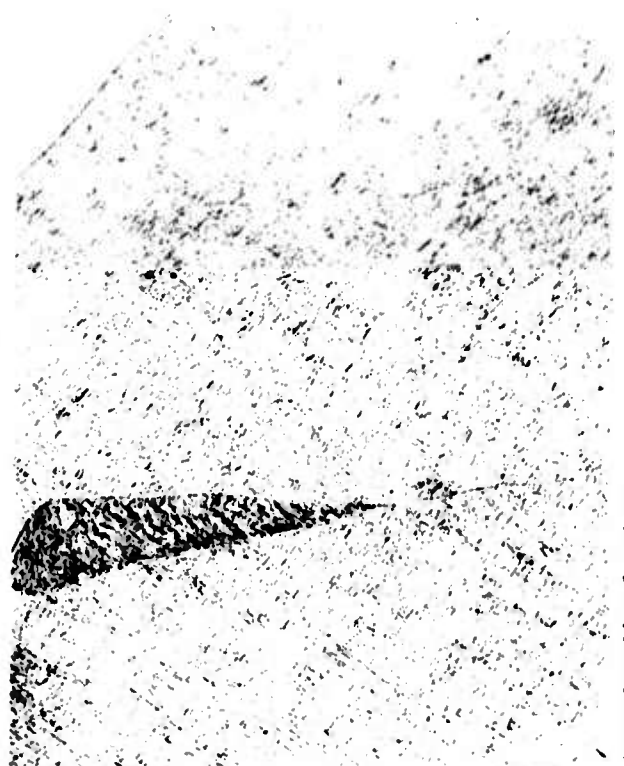


FIGURE 48. MICROSTRUCTURE IN THREE DIRECTIONS OF THE Ti-6Al-6V-2Sn FUSION ZONE WITHOUT FILLER METAL, PLASMA ARC WELDING PROCESS, AS-WELDED, 100X

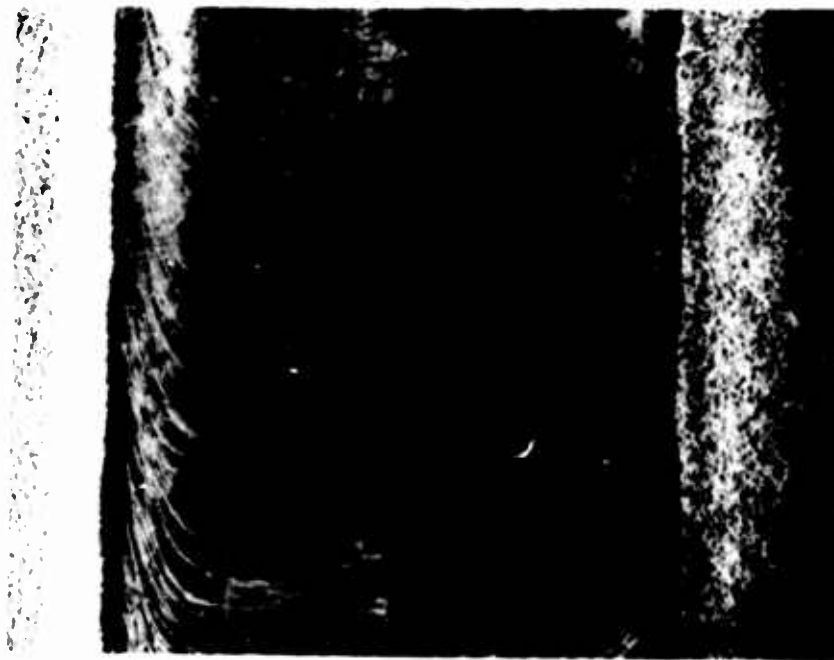


FIGURE 49. SOLIDIFICATION PATTERN OF A WELD BEAD,  
AUTOMATIC GTAW PROCESS 5X

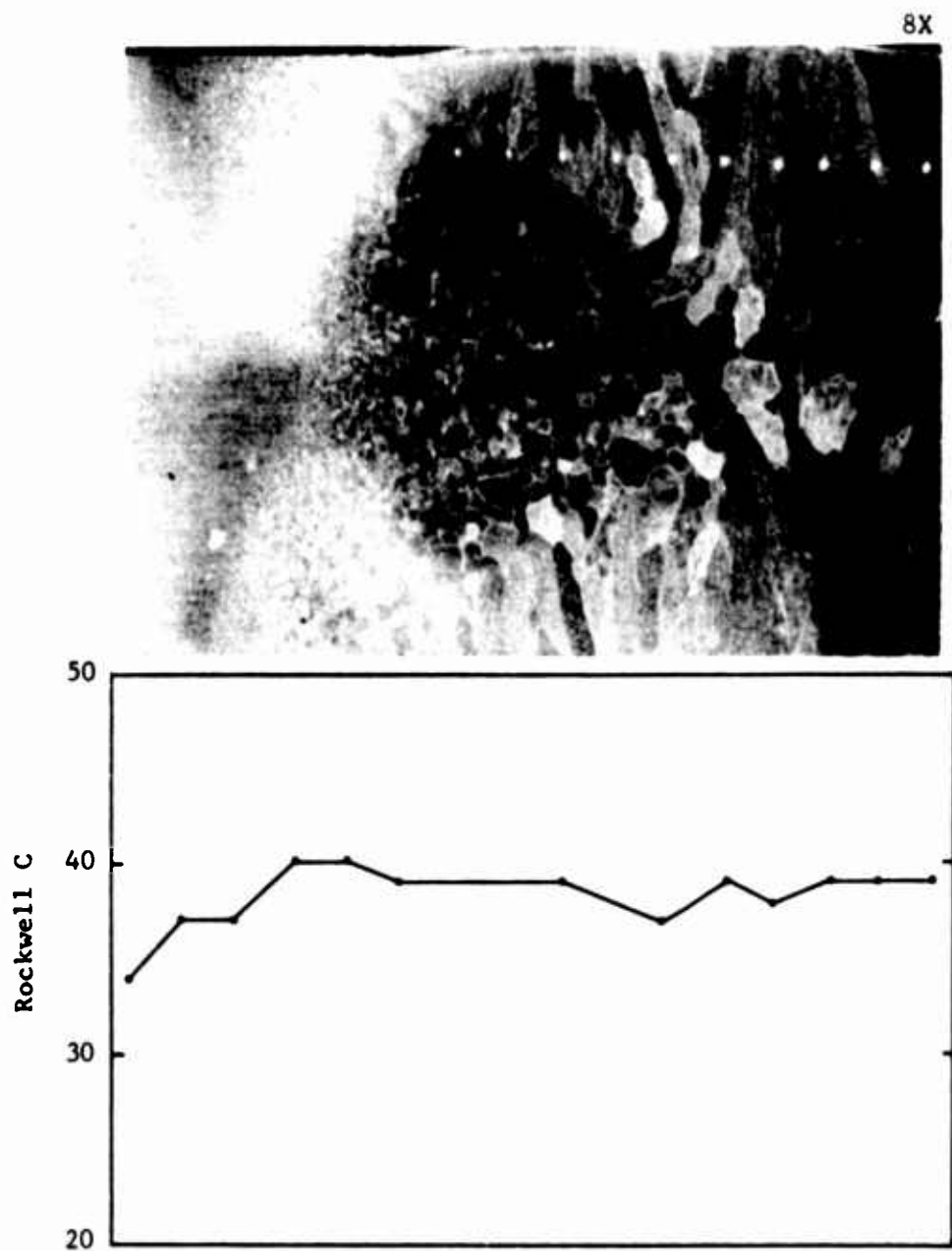


FIGURE 50. MACROSTRUCTURE AND HARDNESS MEASUREMENTS IN AN AUTOMATIC GTA WELD USING Ti-6Al-6V-2Sn FILLER METAL

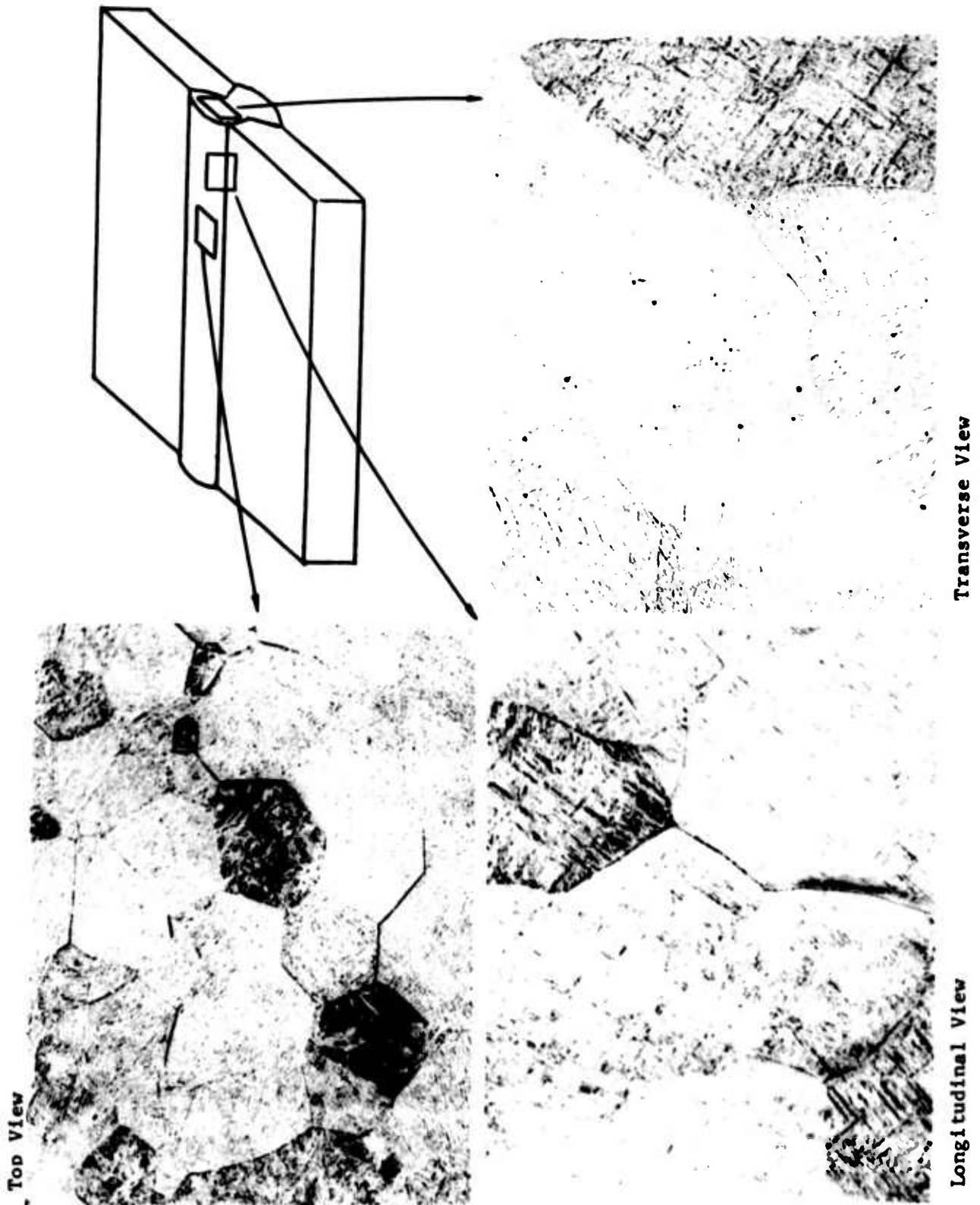


FIGURE 51. MICROSTRUCTURE IN THREE DIRECTIONS OF THE Ti-6Al-6V-2Sn FUSION ZONE, MATCHING FILLER METAL, AUTOMATIC GTAW PROCESS, AS-WELDED, 100X



FIGURE 52. SOLIDIFICATION PATTERN OF A WELD BEAD,  
ELECTRON BEAM WELDING PROCESS 20X

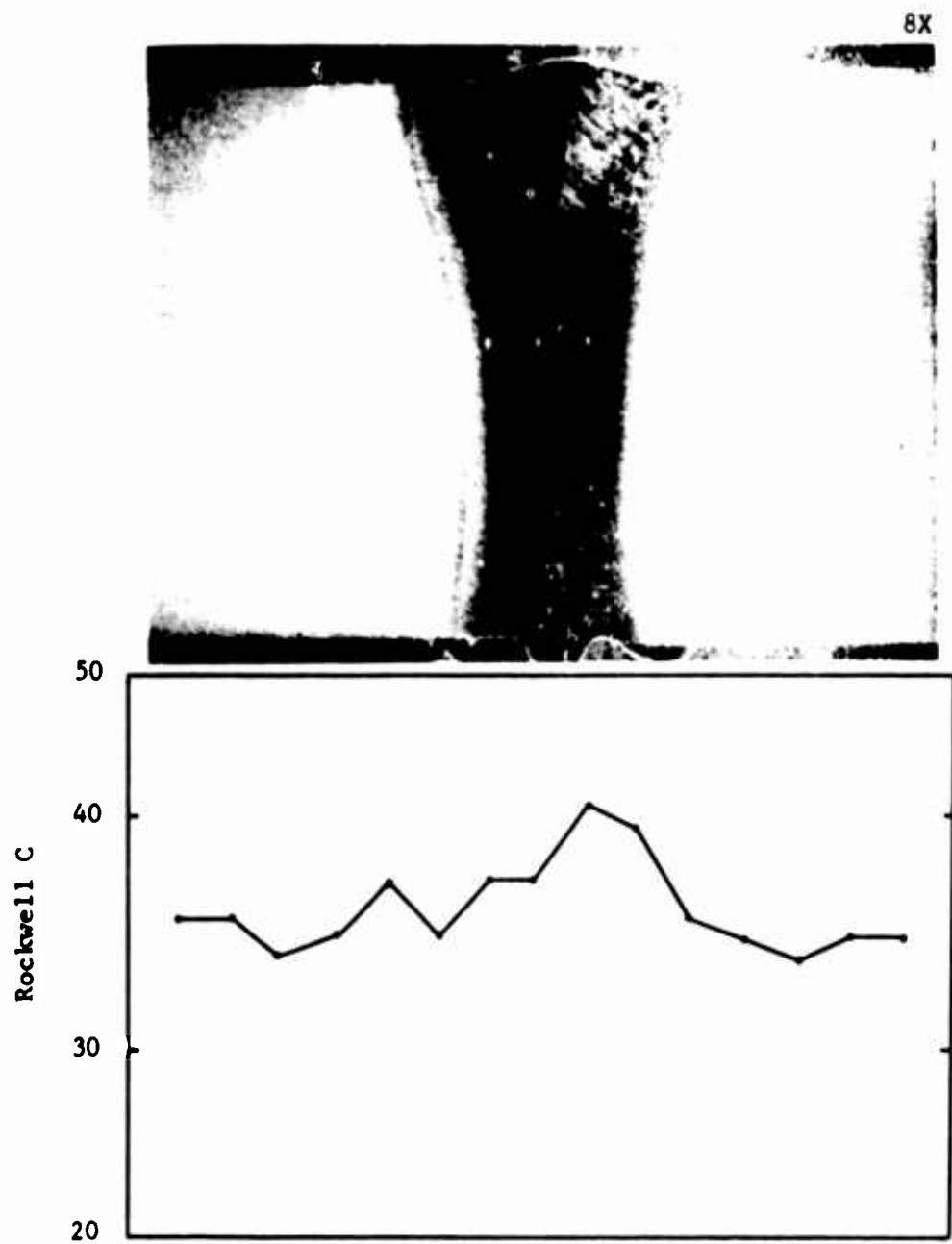
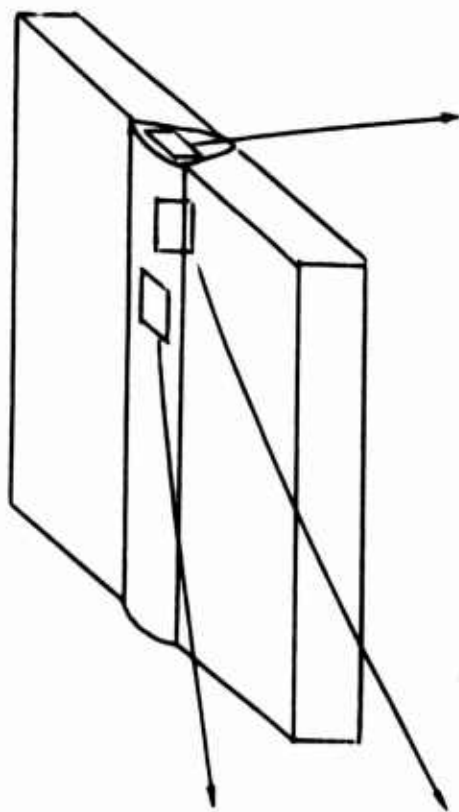


FIGURE 53. MACROSTRUCTURE AND HARDNESS MEASUREMENTS IN AN ELECTRON BEAM WELD WITHOUT FILLER METAL

Top View



Transverse View

Longitudinal View

FIGURE 54. MICROSTRUCTURE IN THREE DIRECTIONS OF THE Ti-6Al-6V-2Sn FUSION ZONE WITHOUT FILLER METAL, ELECTRON BEAM WELDING PROCESS, AS-WELDED, 100X

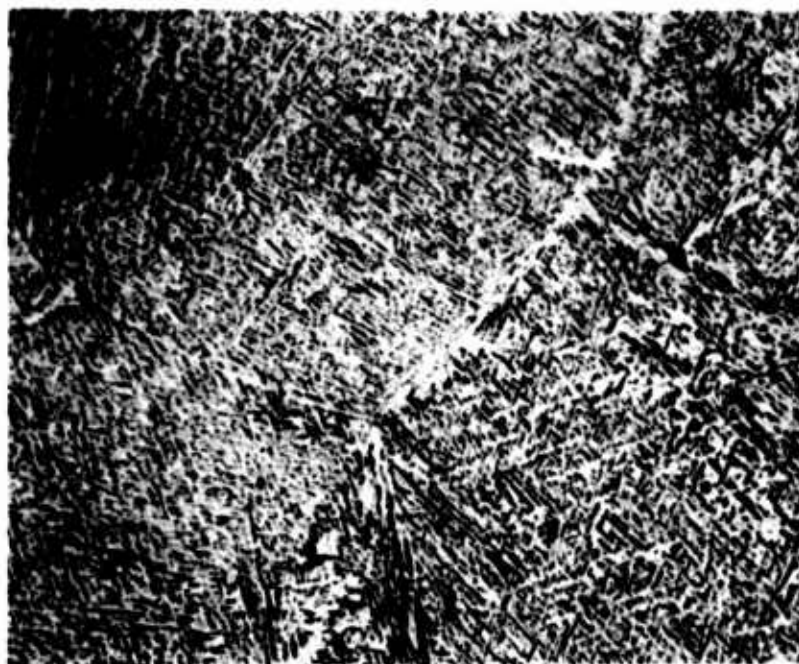


FIGURE 55. FUSION ZONE MICROSTRUCTURE, MANUAL GTAW,  
AS-WELDED 500X

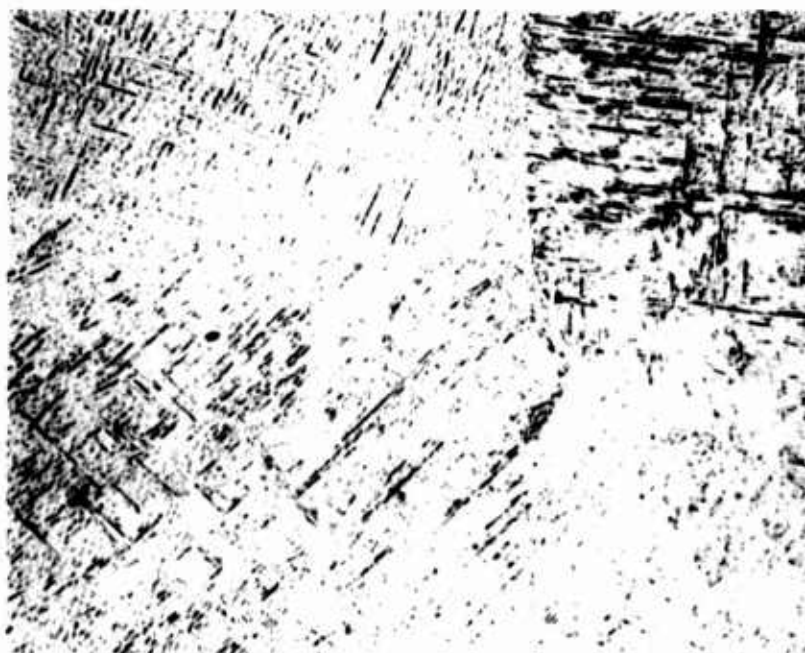


FIGURE 56. FUSION ZONE MICROSTRUCTURE, PLASMA ARC  
WELDING, AS-WELDED 500X





FIGURE 57. FUSION ZONE MICROSTRUCTURE, AUTOMATIC GTAW,  
AS-WELDED 500X

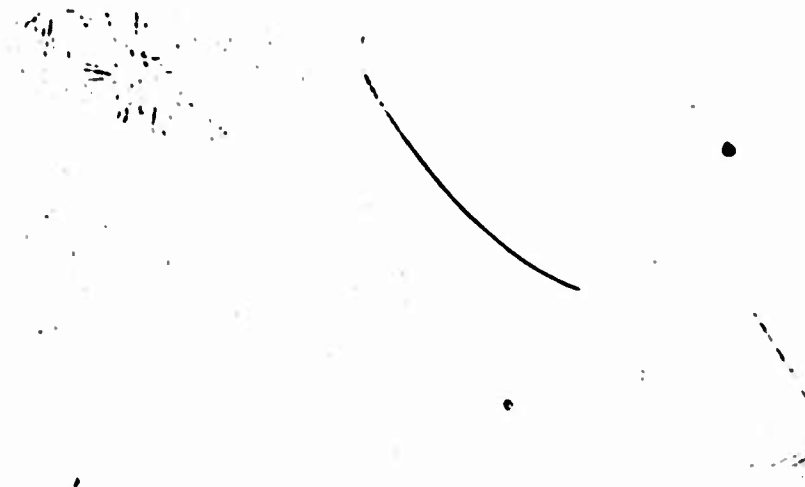


FIGURE 58. FUSION ZONE MICROSTRUCTURE, ELECTRON BEAM  
WELDING, AS-WELDED 500X

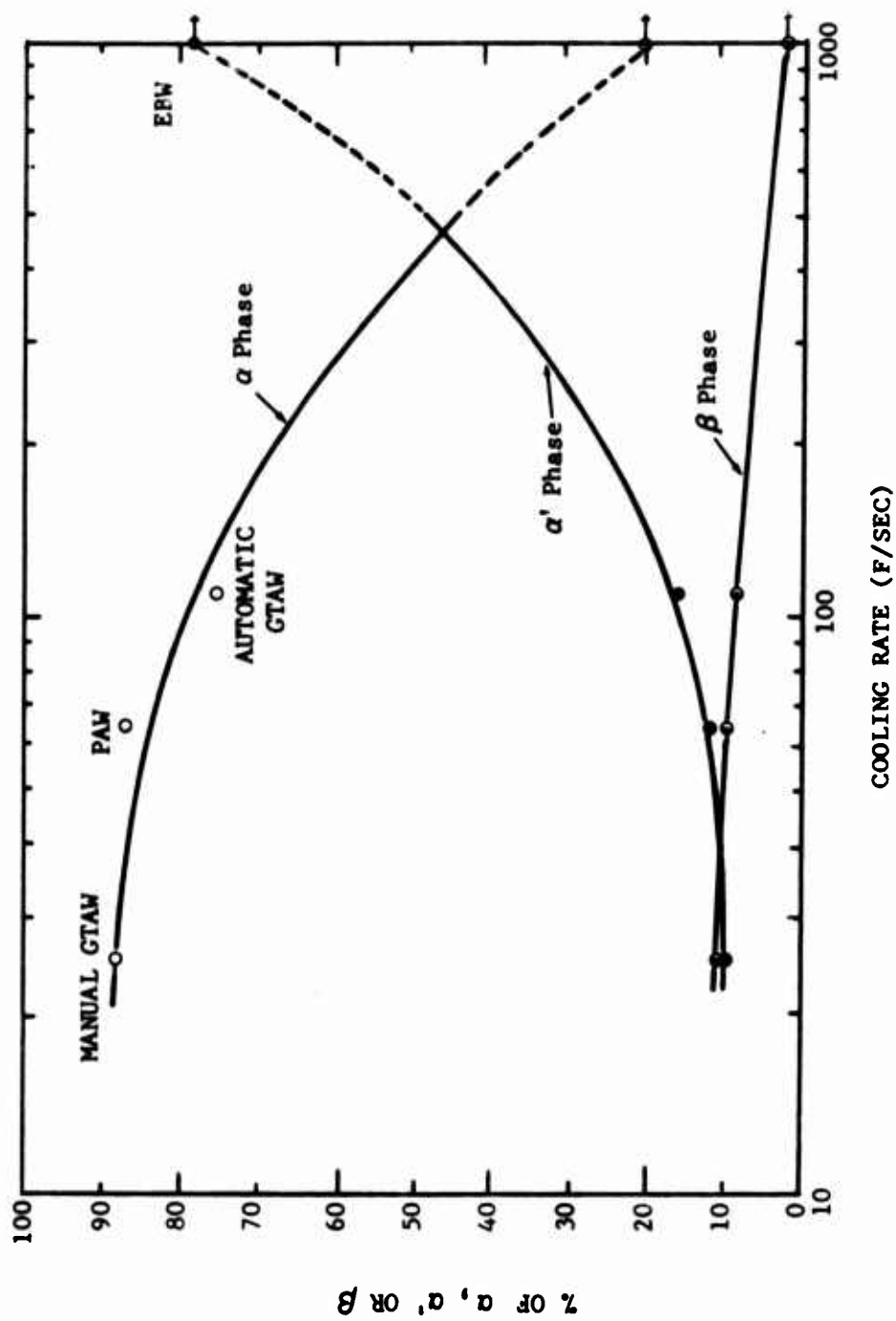


FIGURE 59. EFFECT OF COOLING RATE ON PHASE CONTENTS IN FUSION ZONES, AS-WELDED

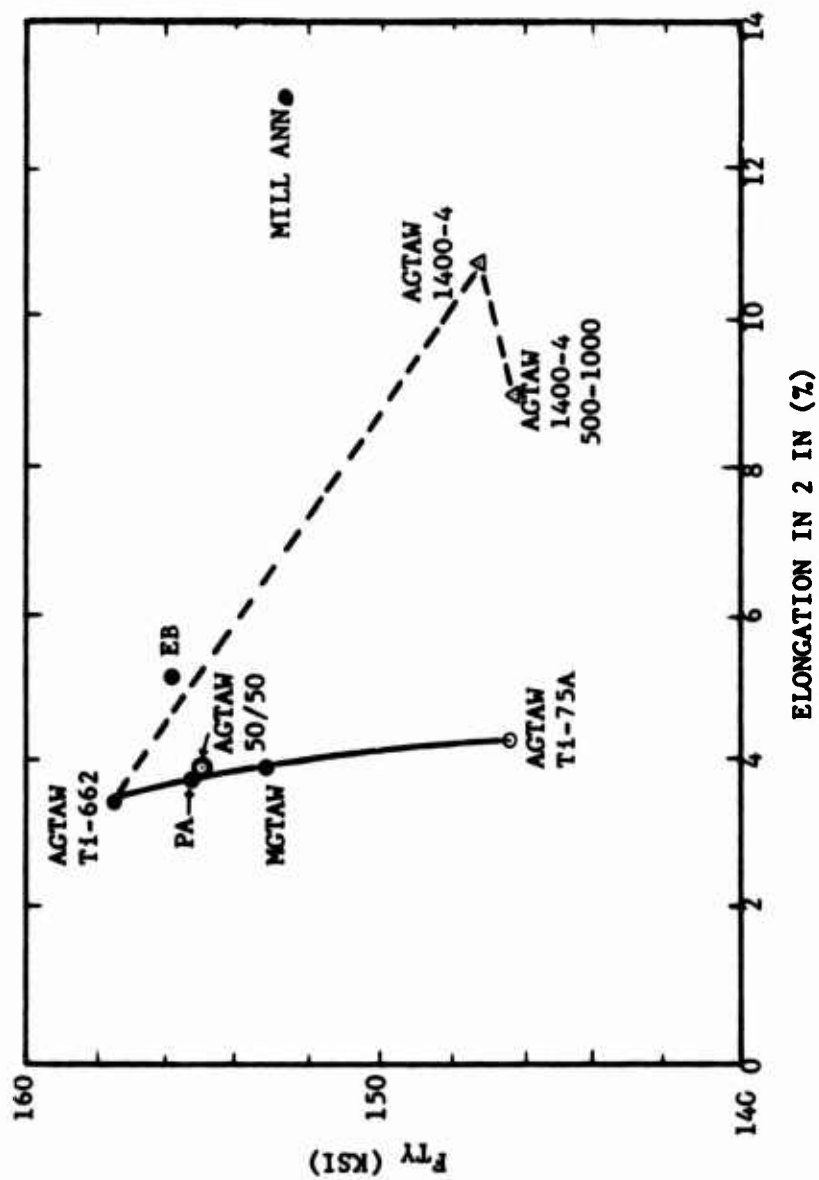


FIGURE 60. TENSILE YIELD - ELONGATION RELATIONSHIP FOR THE FUSION ZONES PRODUCED BY VARIOUS WELDING PROCESSES AND HEAT TREATMENTS

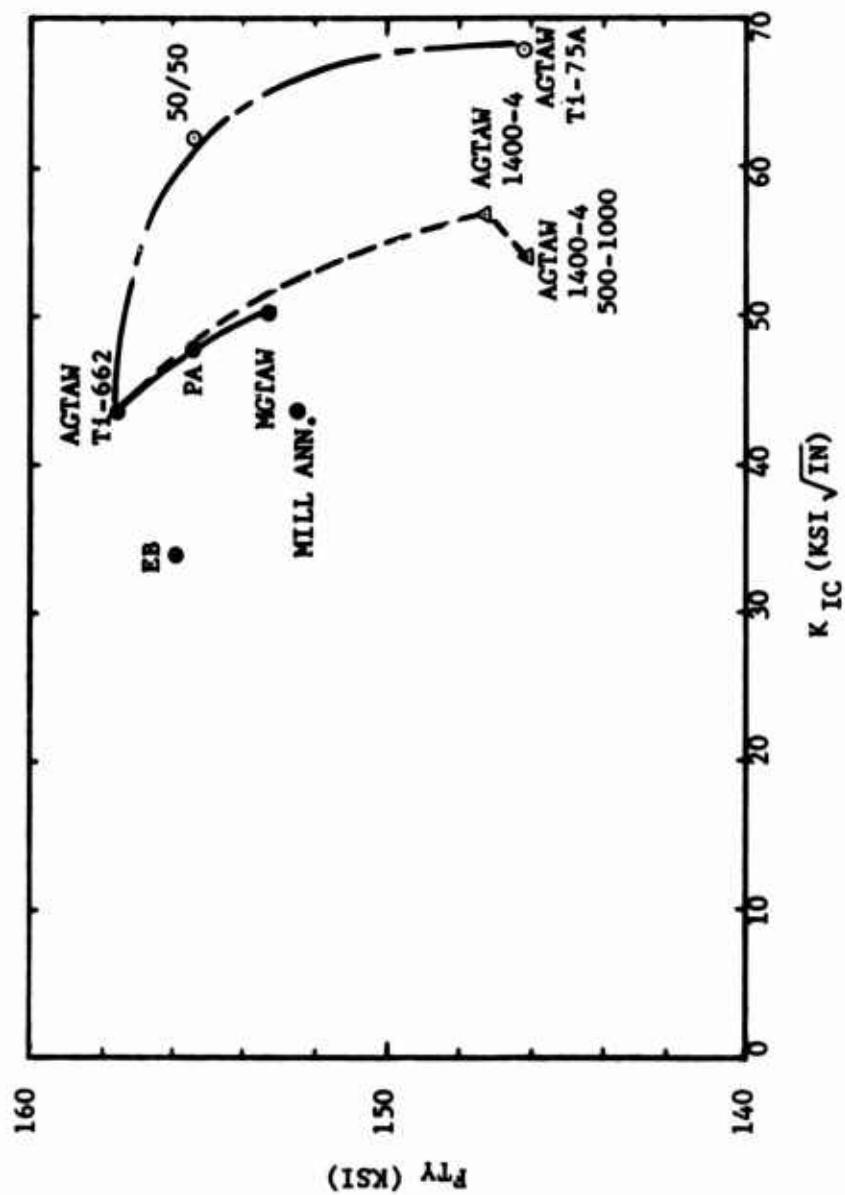


FIGURE 61. TENSILE YIELD - FRACTURE TOUGHNESS RELATIONSHIP FOR THE FUSION ZONES PRODUCED BY VARIOUS WELDING PROCESSES AND HEAT TREATMENTS



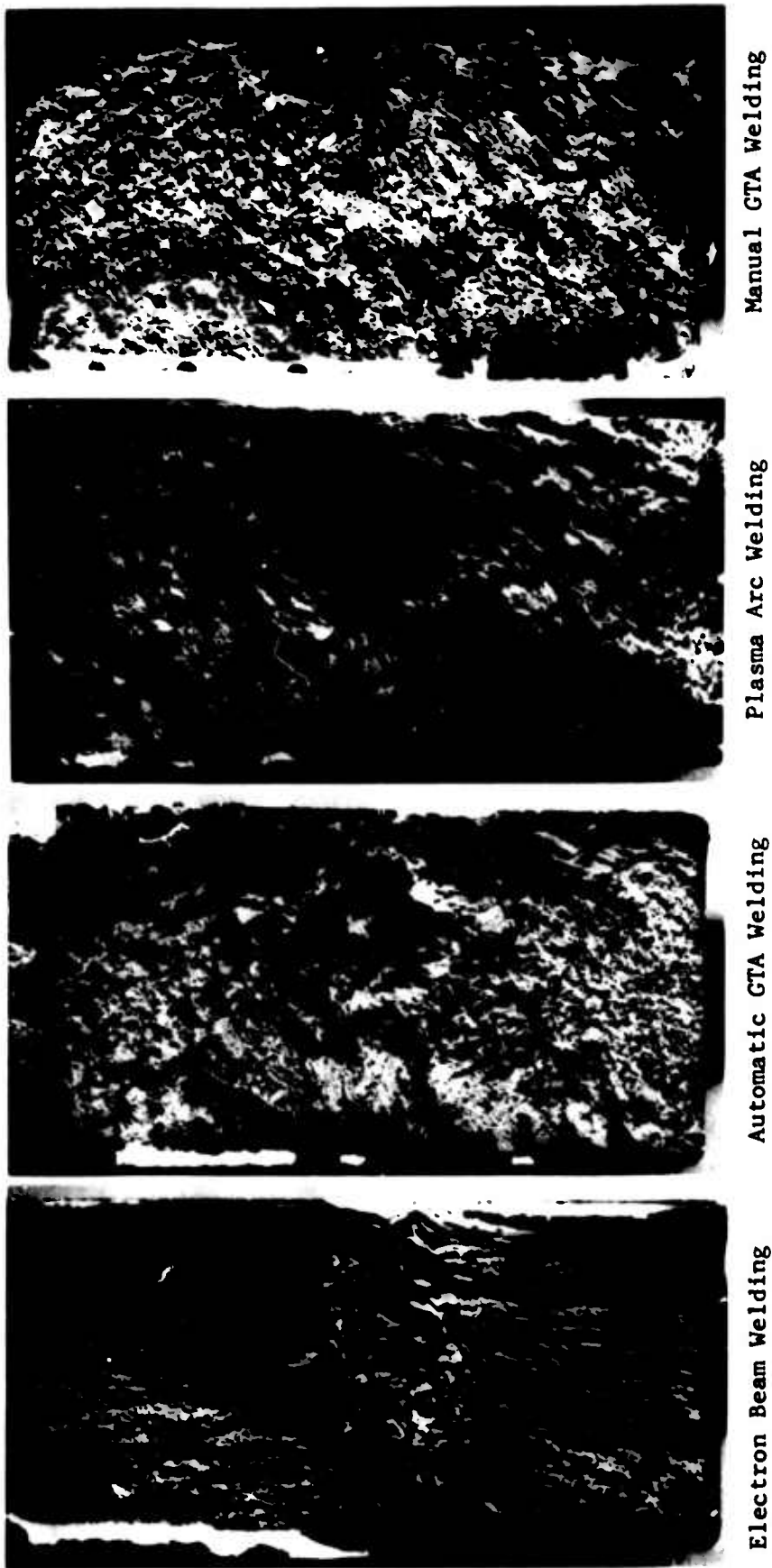


FIGURE 63. FRACTURE SURFACE OF THE FATIGUE TESTED SPECIMENS

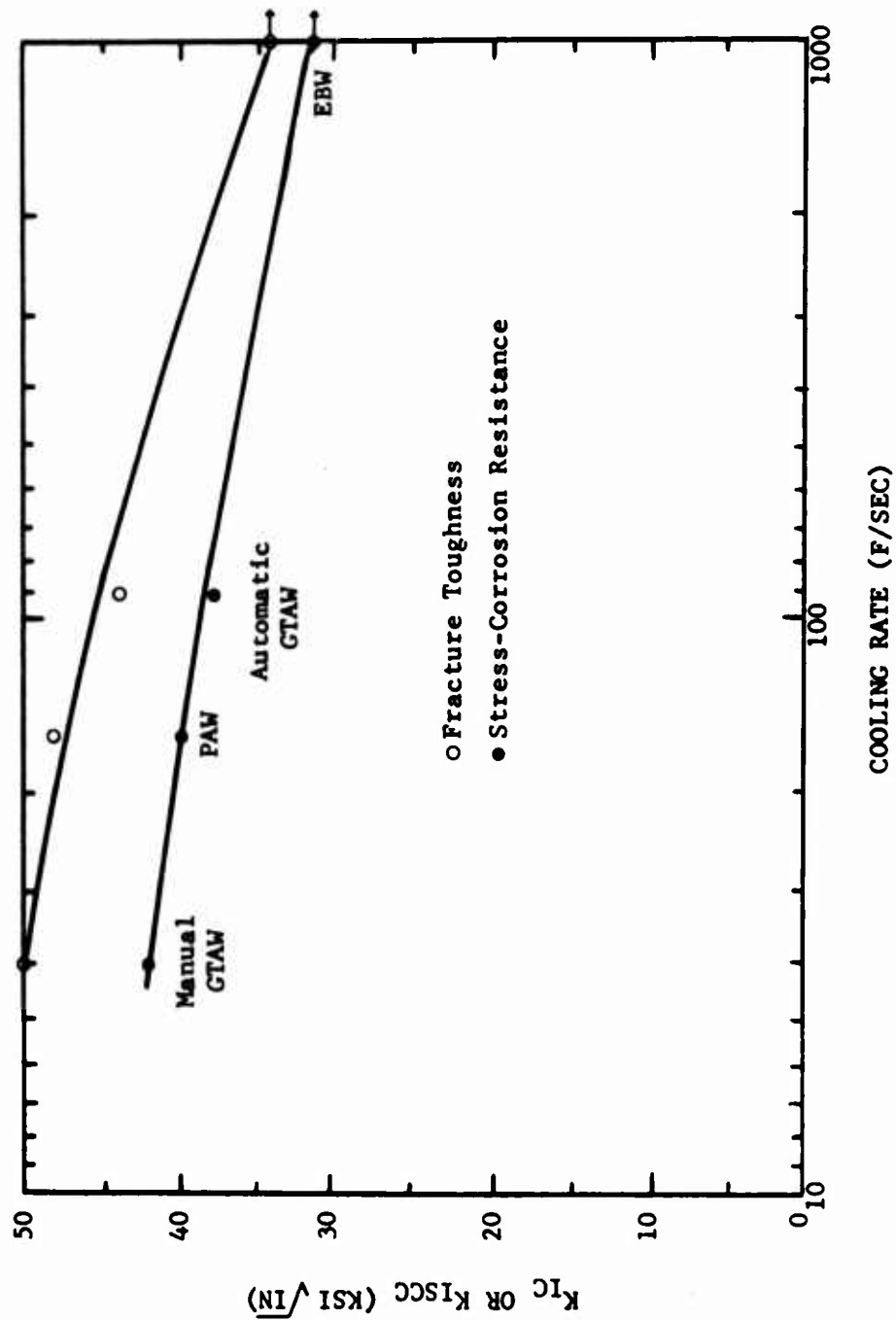


FIGURE 64. EFFECT OF COOLING RATE ON FRACTURE TOUGHNESS AND STRESS-CORROSION RESISTANCE OF FUSION ZONES

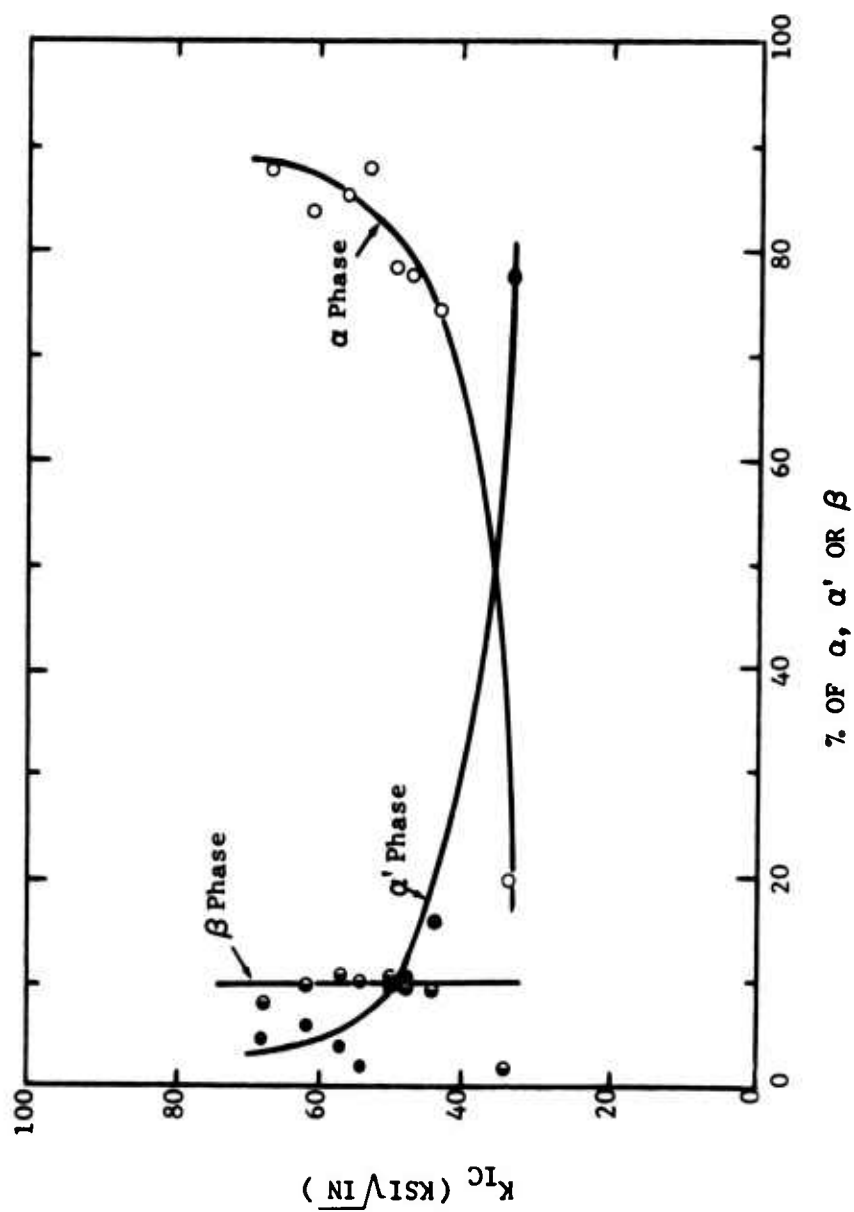


FIGURE 65. EFFECT OF PHASE CONTENT ON FRACTURE TOUGHNESS OF FUSION ZONES, ALL CONDITIONS



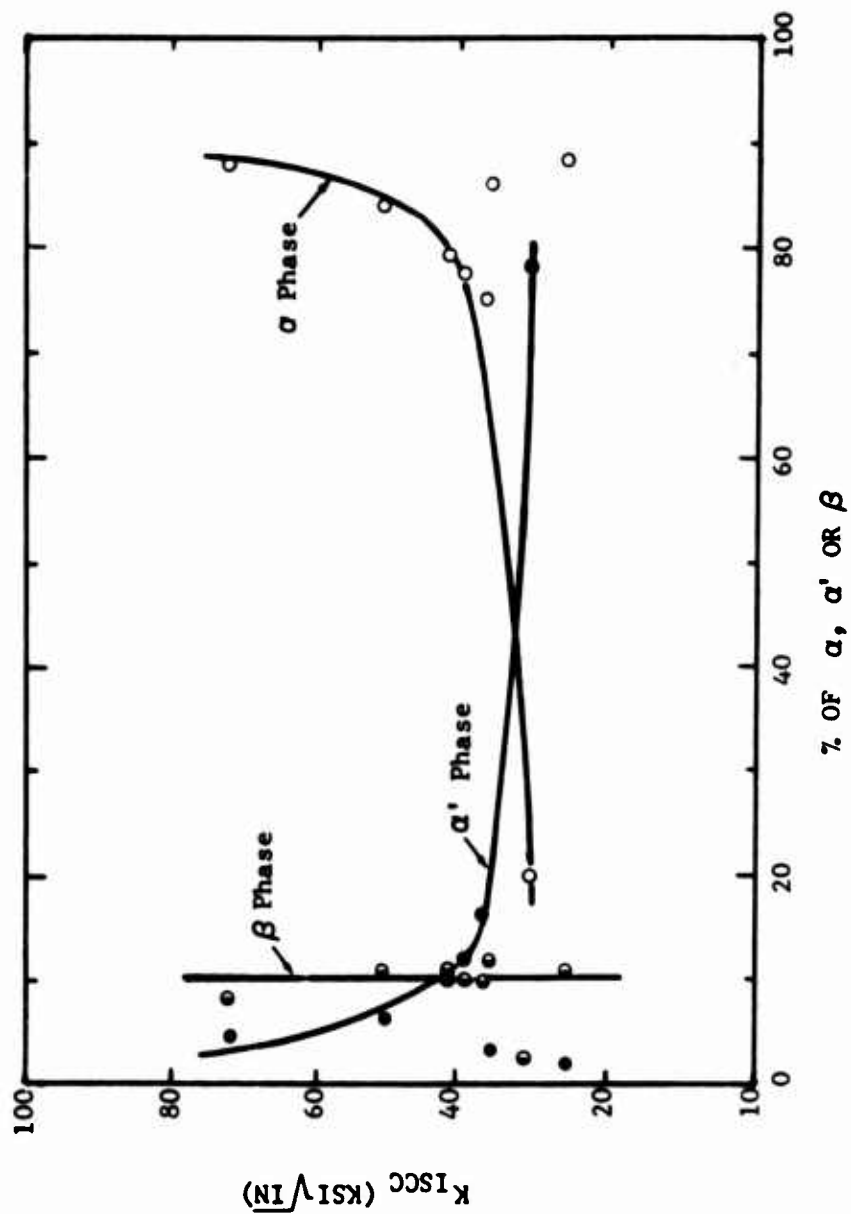
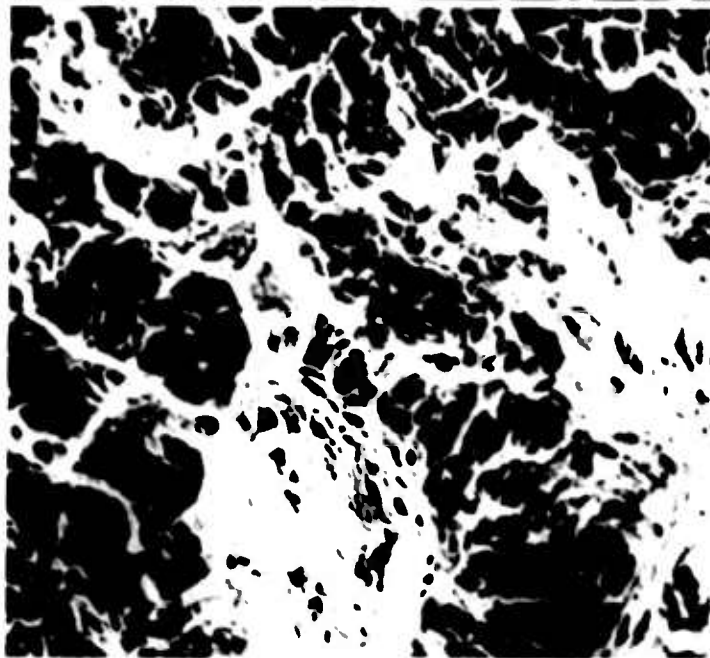


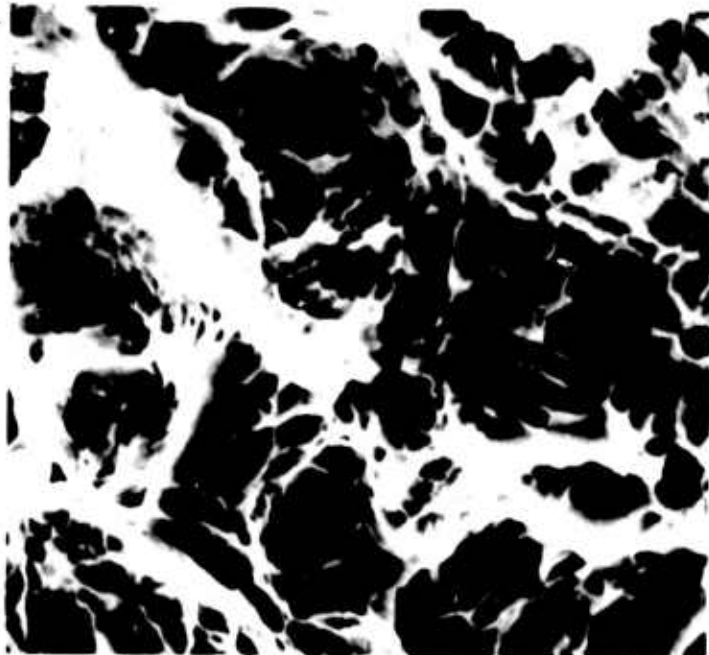
FIGURE 66. EFFECT OF PHASE CONTENT ON STRESS-CORROSION RESISTANCE OF FUSION ZONES, ALL CONDITIONS



(a) 6X



(b) 700X



(c) 2100X

FIGURE 67. FRACTURE SURFACE OF A MANUAL GTA WELDED FUSION ZONE  
FRACTURE-TOUGHNESS TESTED

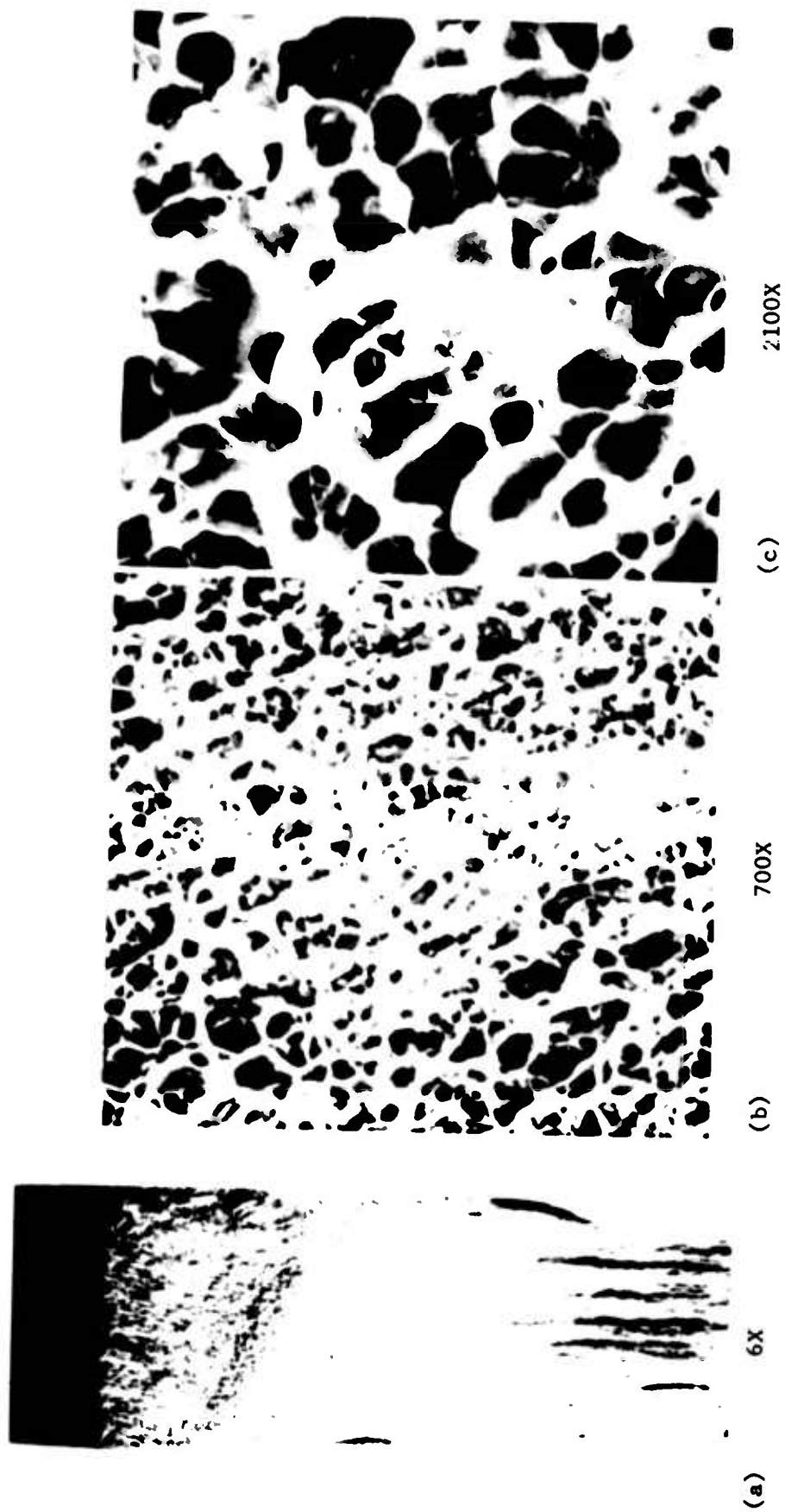


FIGURE 68. FRACTURE SURFACE OF AN ELECTRON BEAM WELDED  
FUSION ZONE FRACTURE-TOUGHNESS TESTED

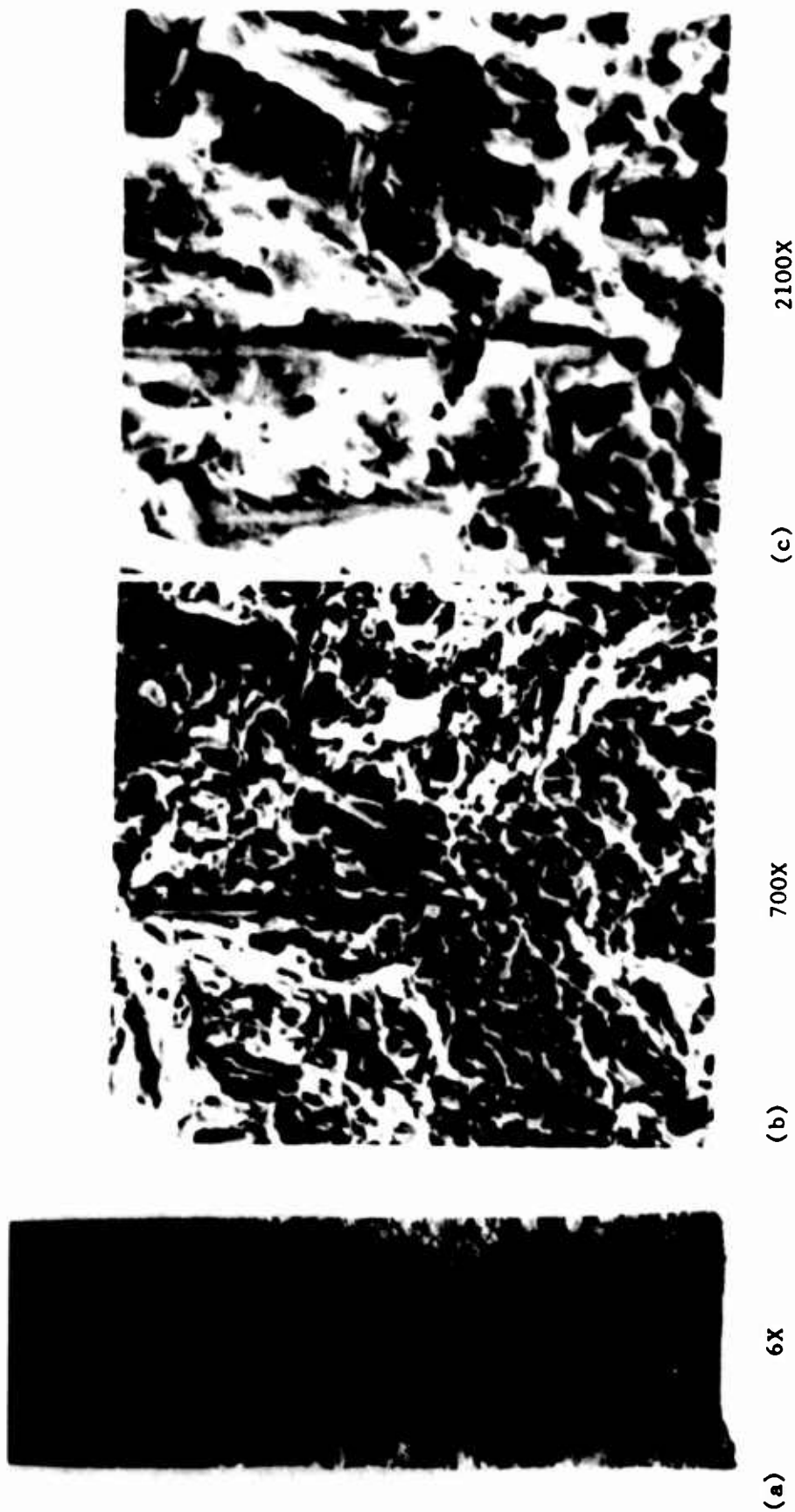


FIGURE 69. FRACTURE SURFACE OF A MANUAL GTA WELDED  
FUSION ZONE STRESS-CORROSION TESTED

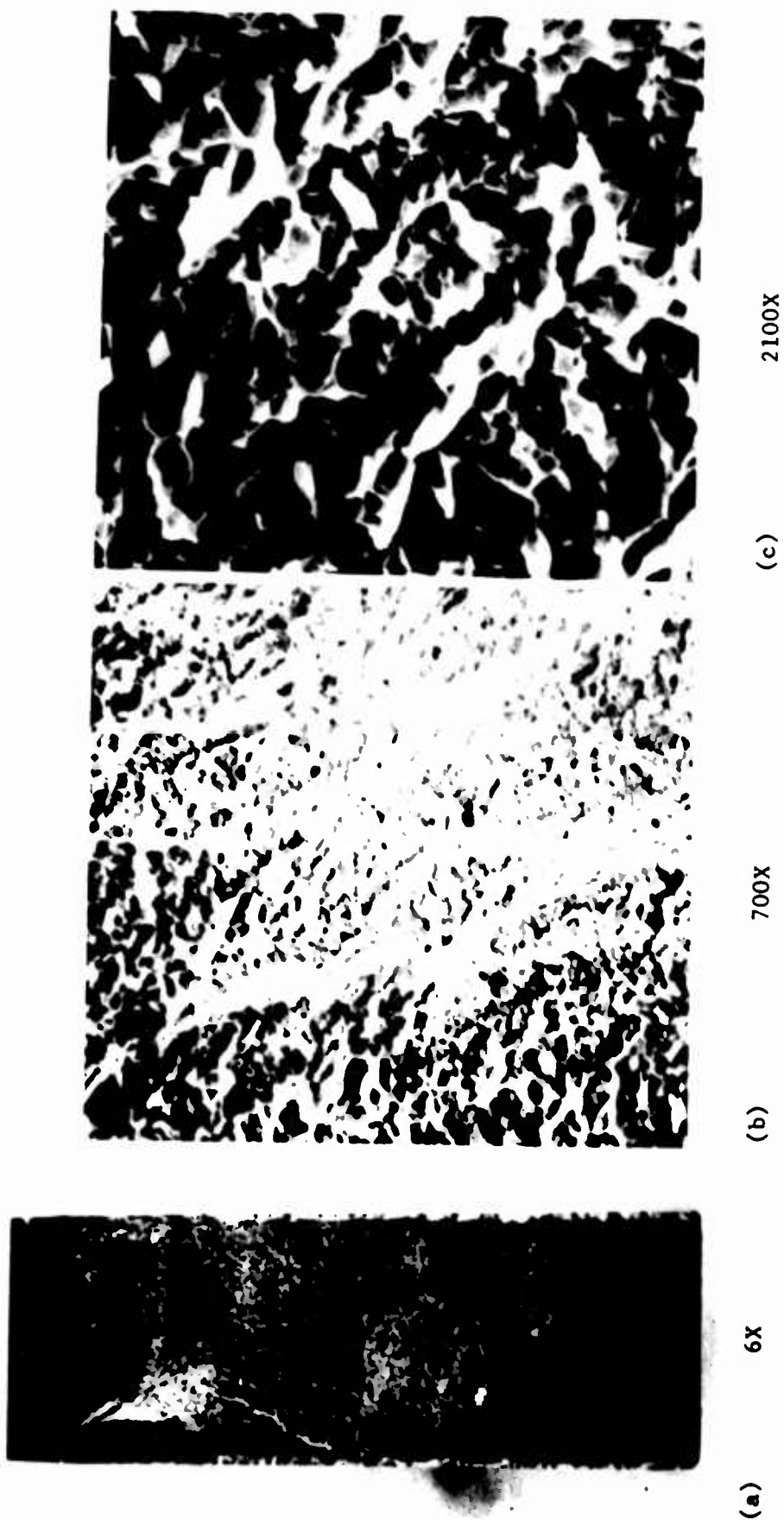


FIGURE 70. FRACTURE SURFACE OF AN ELECTRON BEAM WELDED  
FUSION ZONE STRESS-CORROSION TESTED

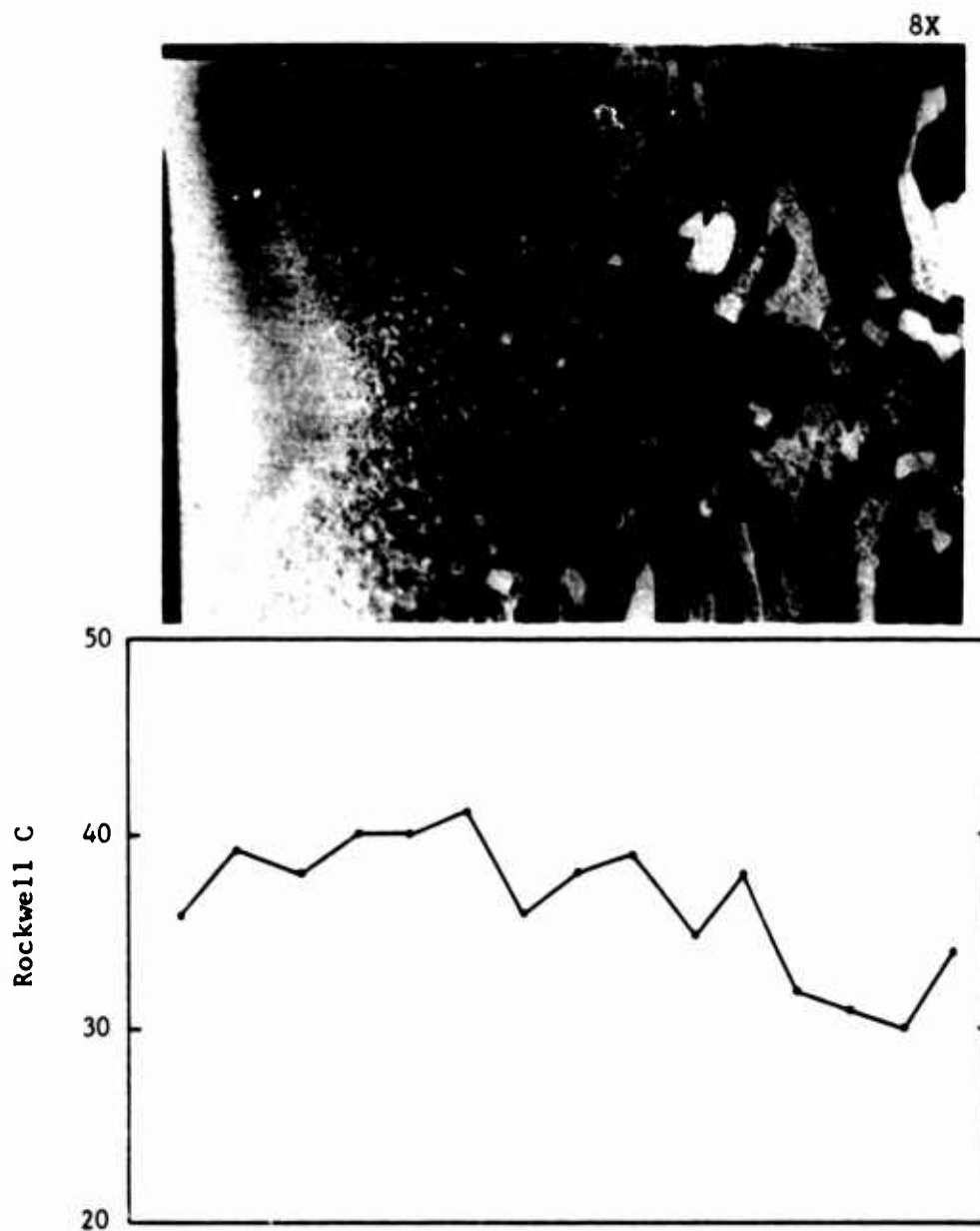


FIGURE 71. MACROSTRUCTURE AND HARDNESS MEASUREMENTS IN AN AUTOMATIC GTA WELD USING 50% Ti-662 AND 50% Ti-75A FILLER METAL

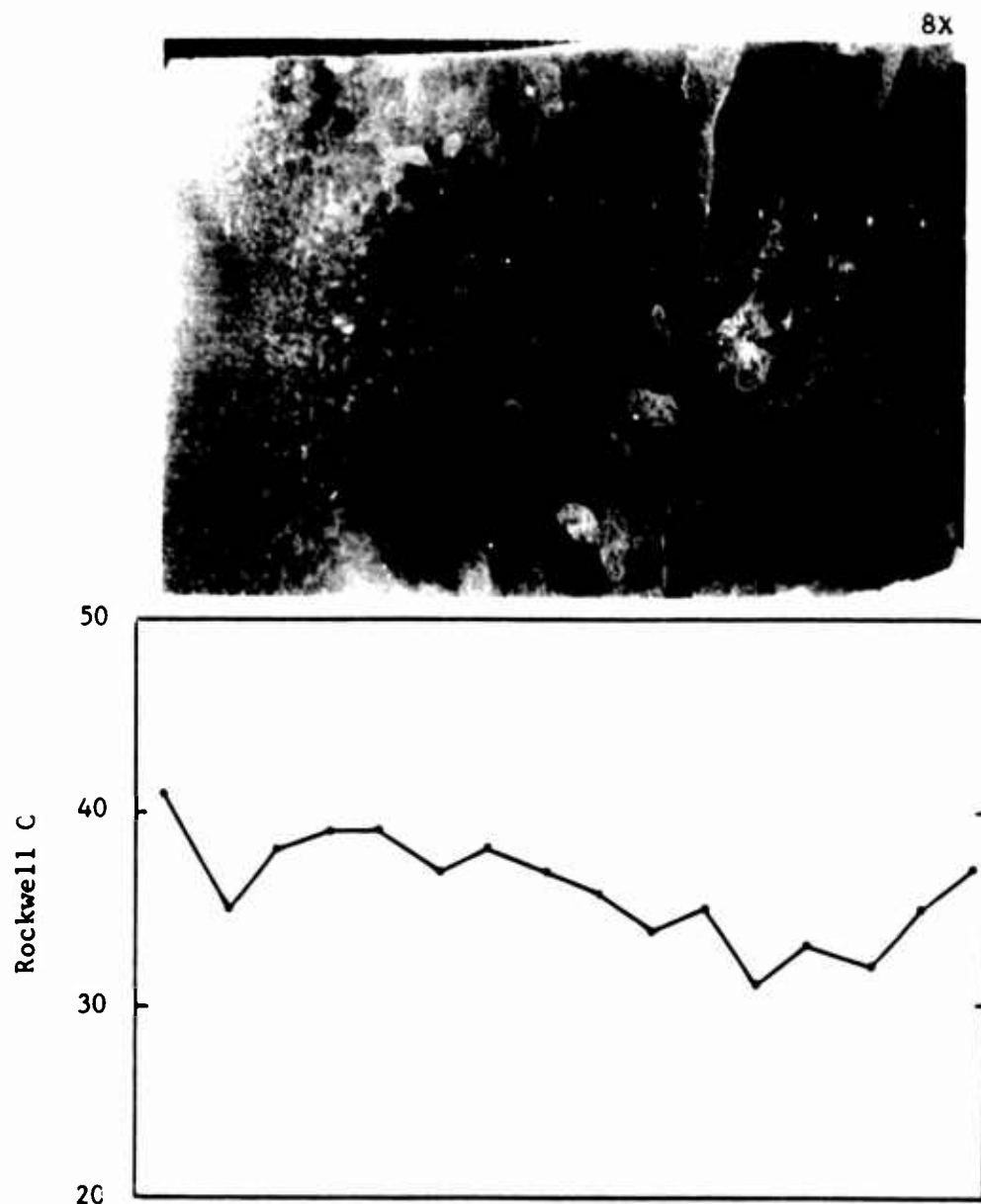


FIGURE 72. MACROSTRUCTURE AND HARDNESS MEASUREMENTS IN AN AUTOMATIC GTA WELD USING 100% Ti-75A FILLER METAL

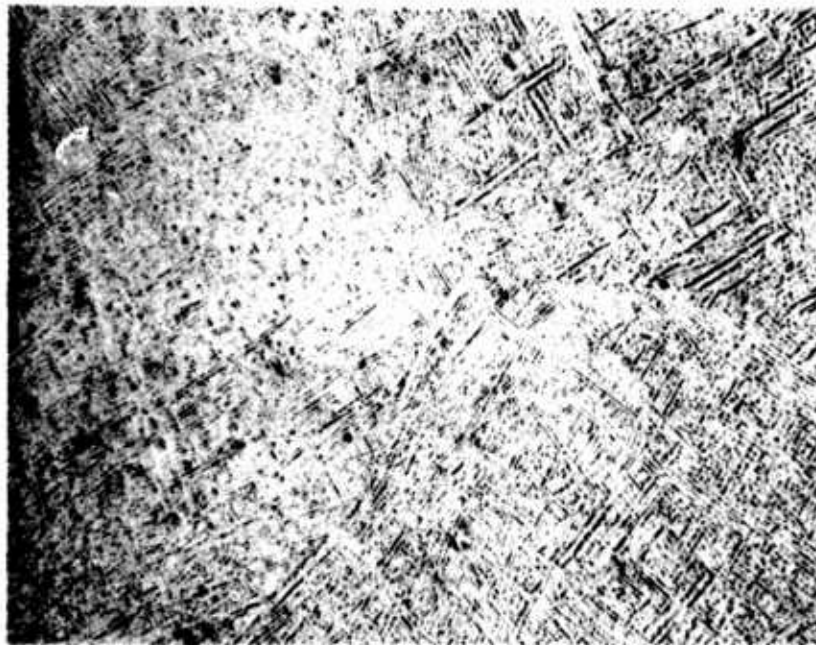


FIGURE 73. FUSION ZONE MICROSTRUCTURE, AUTOMATIC GTAW,  
50% Ti-662 AND 50% Ti-75A FILLER METAL  
500X



FIGURE 74. FUSION ZONE MICROSTRUCTURE, AUTOMATIC GTAW,  
100% Ti-75A FILLER METAL  
500X





— HORIZONTAL  
 --- VERTICAL

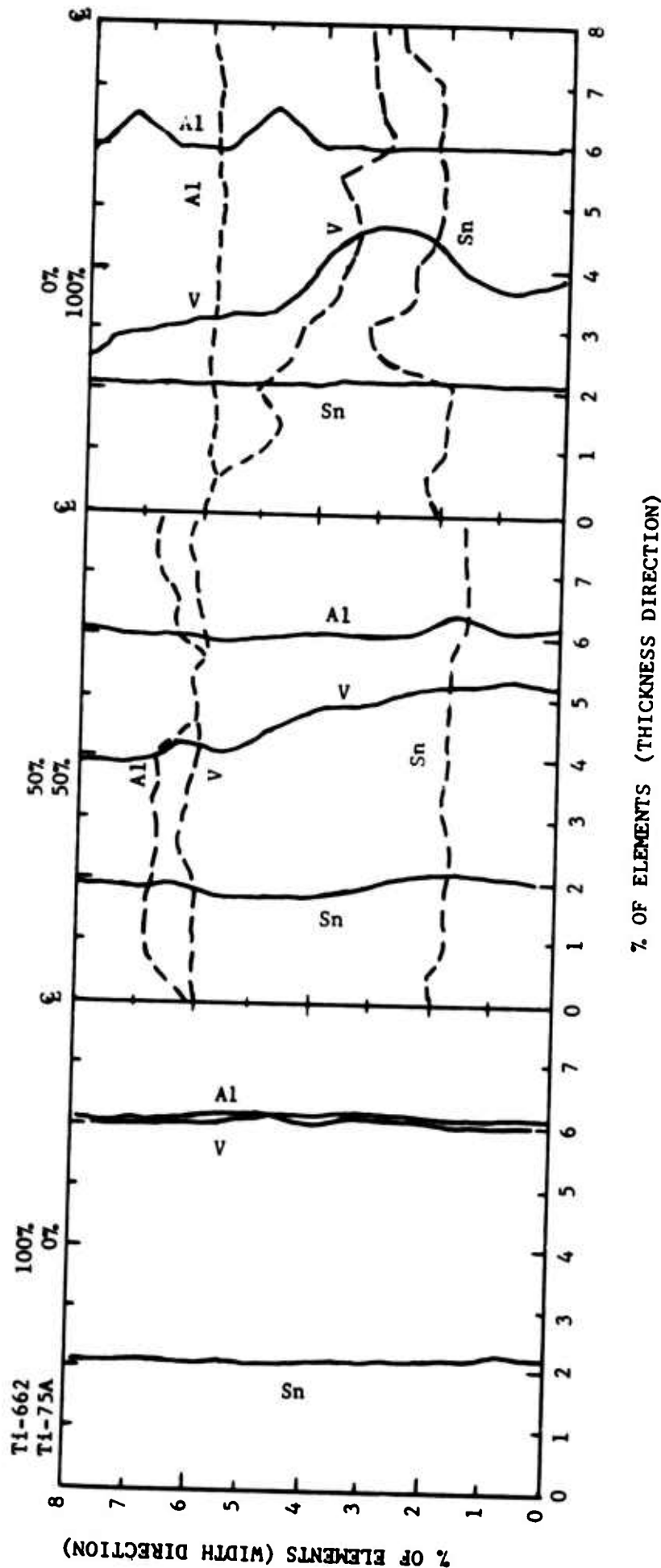


FIGURE 75. ELECTRON MICROPROBE TRACES FOR DUAL FILLER-METAL WELDED FUSION ZONES

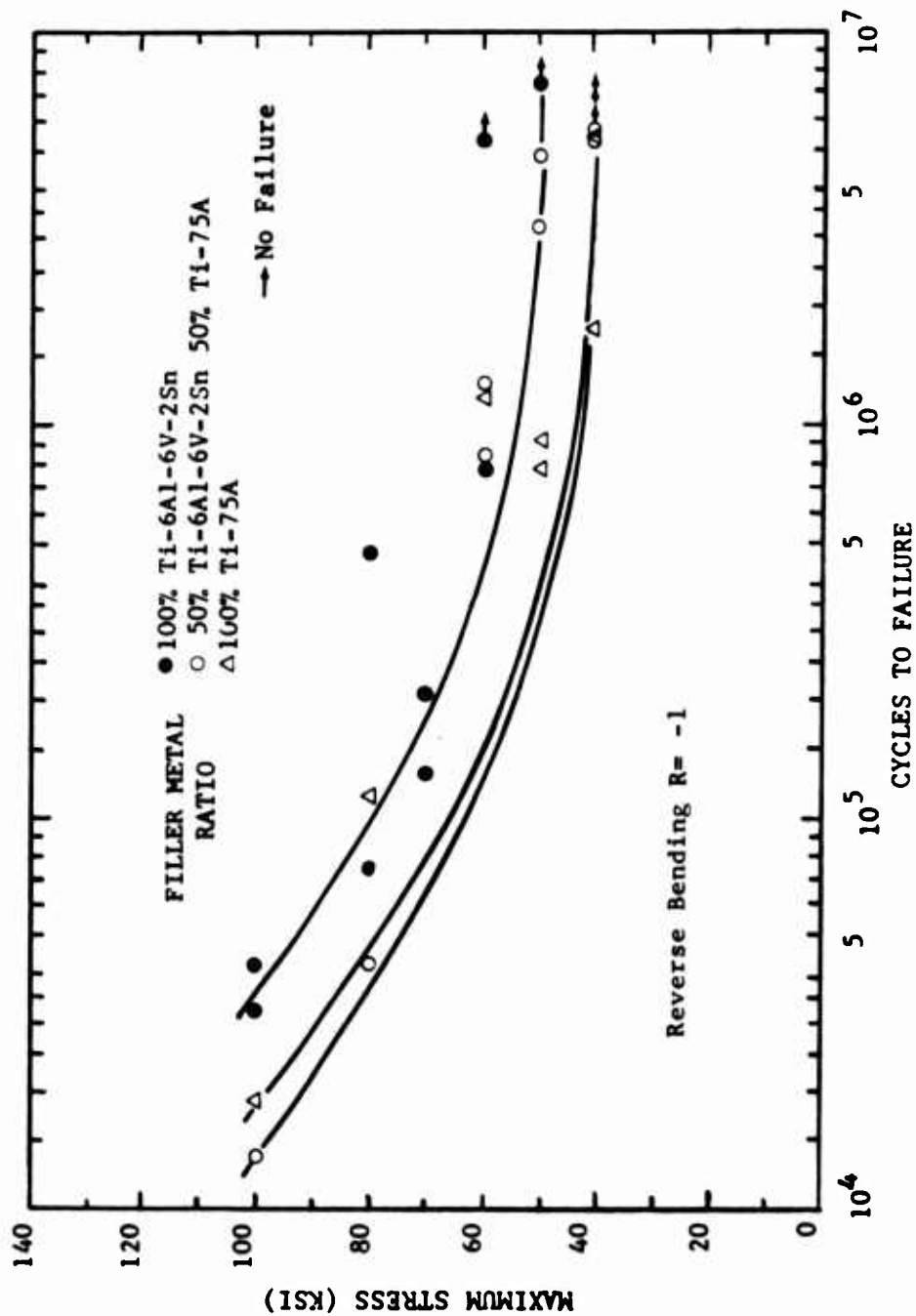


FIGURE 76. S-N DATA FOR Ti-6Al-6V-2Sn WELDS USING DUAL FILLER-METAL

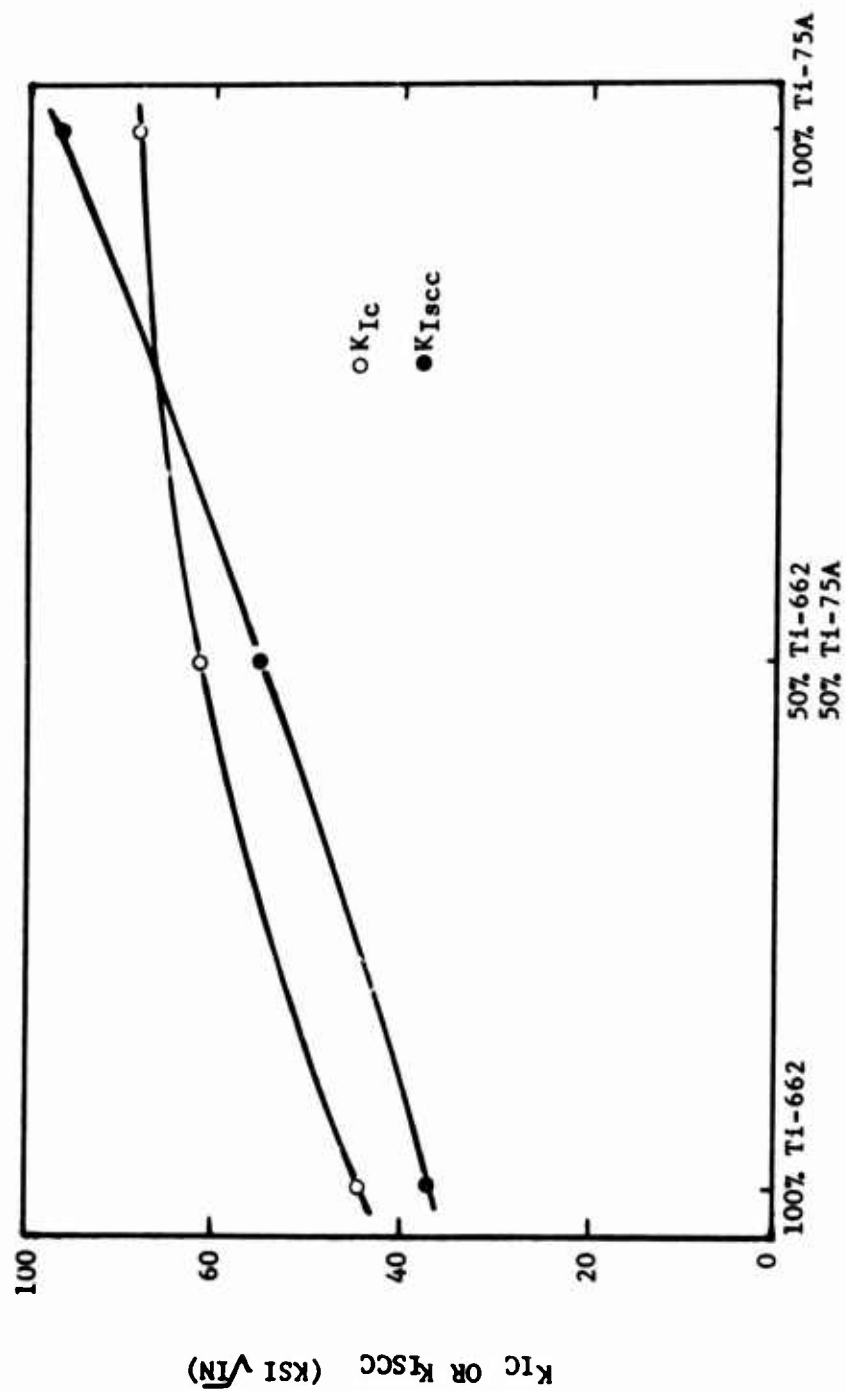


FIGURE 77. EFFECT OF FILLER METAL ON FRACTURE TOUGHNESS AND STRESS-CORROSION RESISTANCE (AUTOMATIC GTAW)

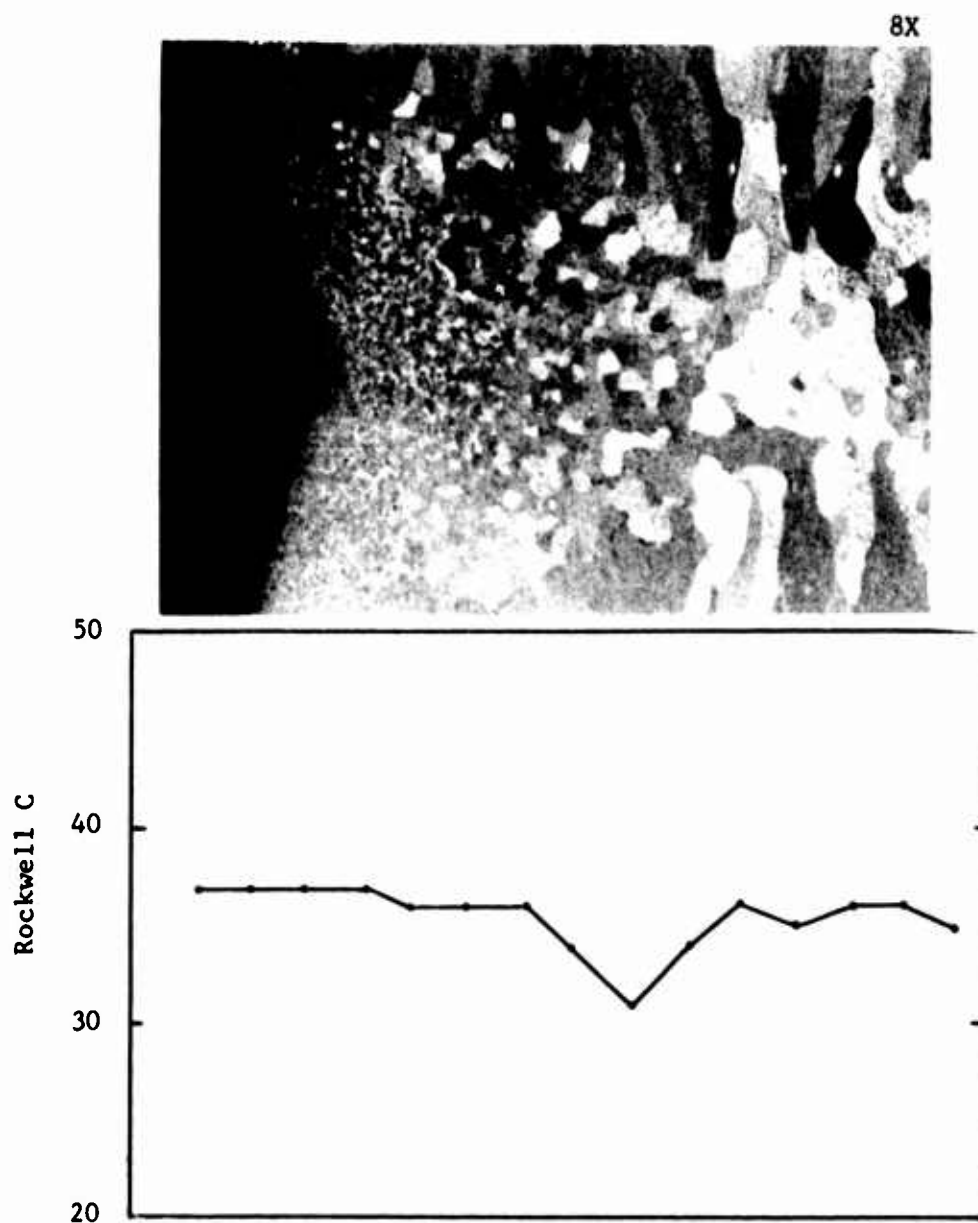


FIGURE 78. MACROSTRUCTURE AND HARDNESS MEASUREMENTS IN AN AUTOMATIC GTA WELD USING T1-662 FILLER METAL, HEAT TREATED AT 1400F - 4 HRS

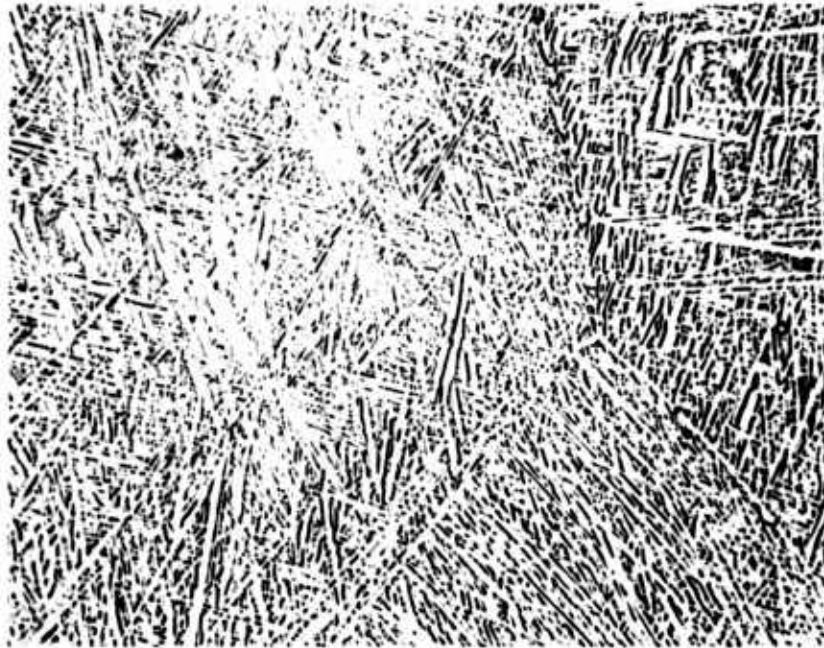


FIGURE 79. FUSION ZONE MICROSTRUCTURE, AUTOMATIC GTAW,  
Ti-662 FILLER METAL, 1400F - 4 HRS 500X

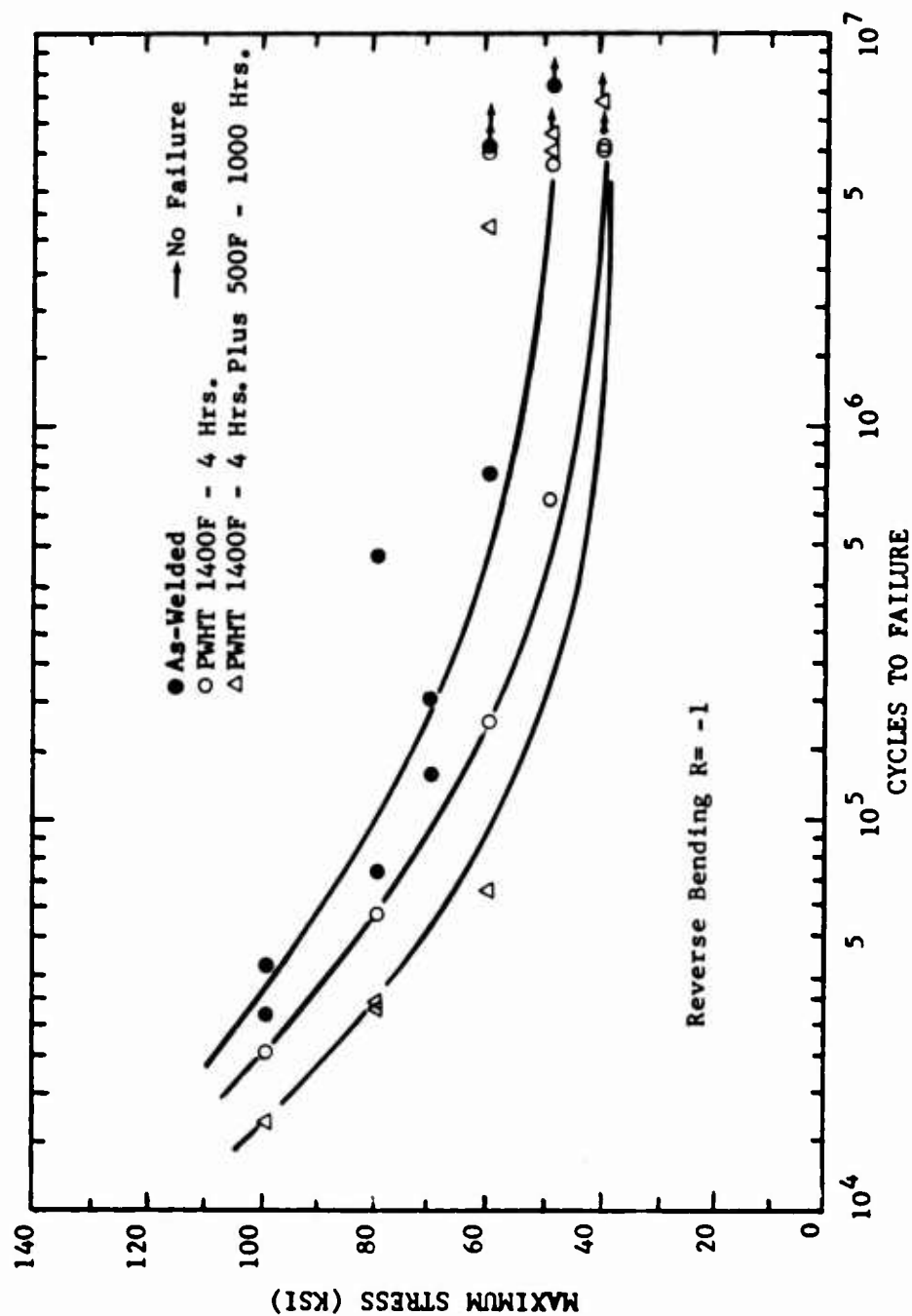


FIGURE 80. S-N DATA FOR T1-6Al-6V-2Sn WELDS, AUTOMATIC GTA WELDED

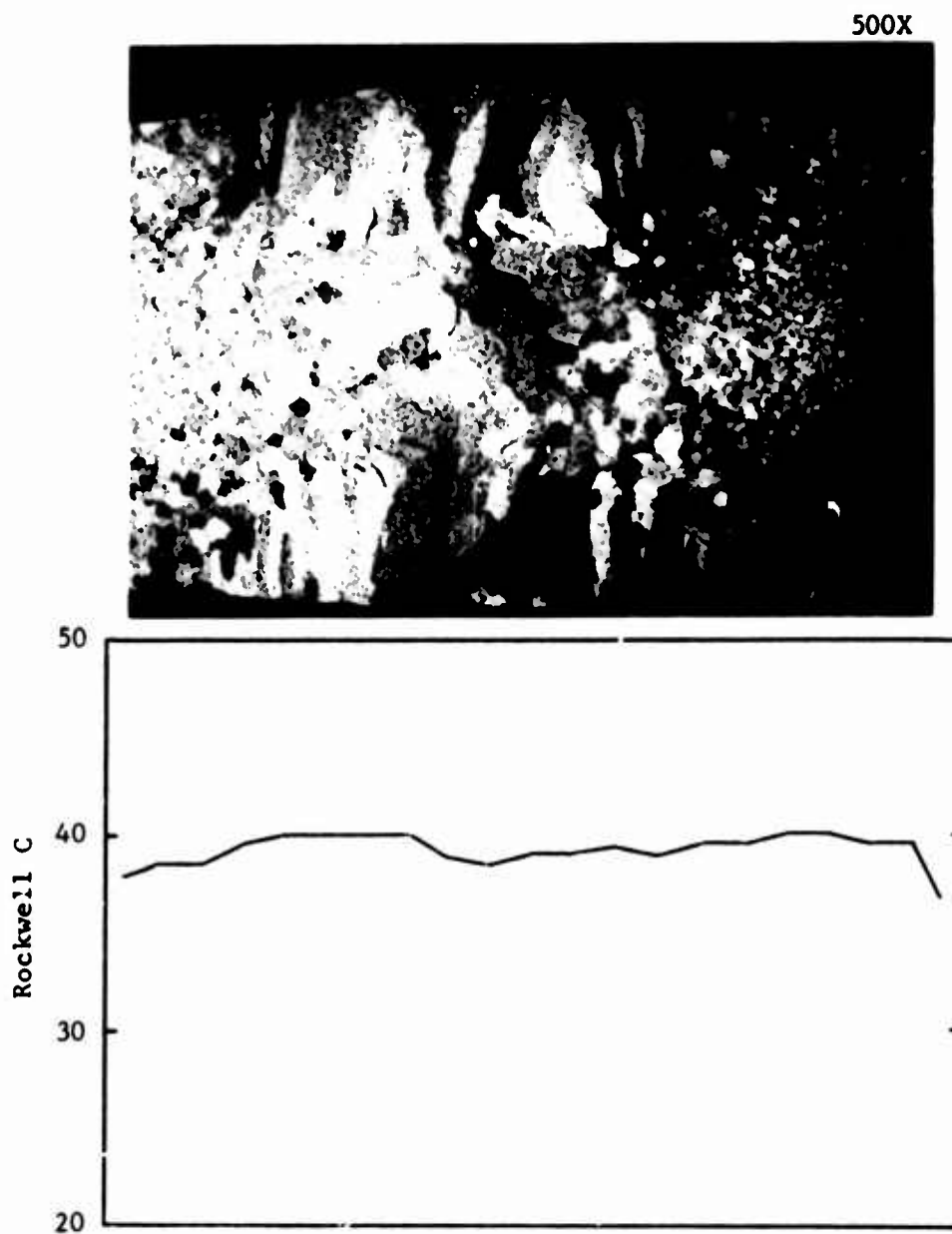


FIGURE 81. MACROSTRUCTURE AND HARDNESS MEASUREMENTS IN AN AUTOMATIC GTA WELD, 1400F - 4 HRS PLUS 500F - 1000 HRS

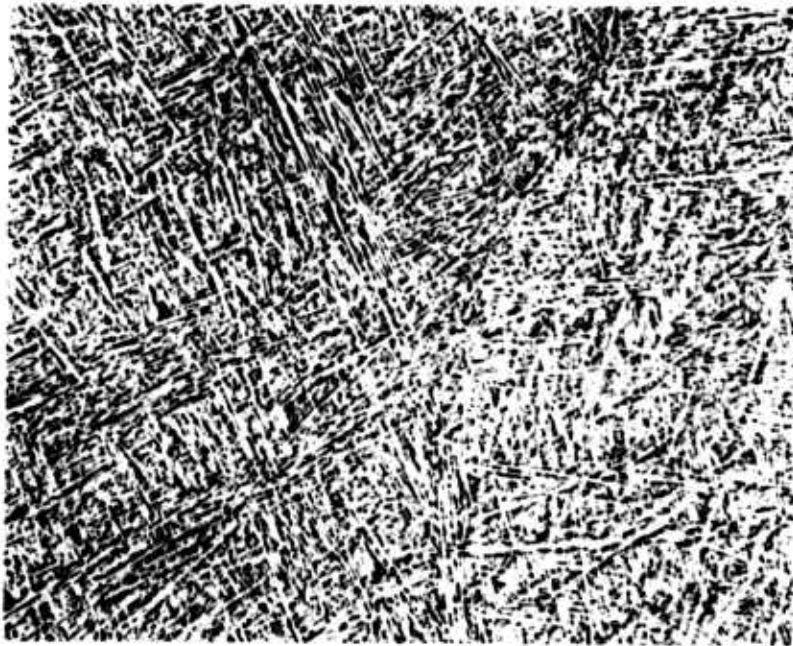


FIGURE 82. FUSION ZONE MICROSTRUCTURE, AUTOMATIC GTAW,  
1400F - 4 HRS PLUS 500F - 1000 HRS 500X